

ABSTRACT

DAVIS, DUNCAN SHERWOOD. Self-Folding of Thermoplastic Polymer Sheets from 2D to 3D. (Under the direction of Dr. Michael Dickey and Dr. Jan Genzer).

This PhD. dissertation focuses on various techniques to convert two-dimensional (2D) sheets into three-dimensional (3D) objects in a hands-free manner. Geometry defines the functions of many objects in society, like chairs, tables, toys, and boxes. Creating 3D structures from 2D sheets is appealing for manufacturing, shipping, and storing objects since flat sheets occupy minimal space. We work with 2D sheets to make processing easier and increase the number of commercially available polymers we can investigate. If a sheet is prestrained, releasing the stored strain can induce self-folding. This thesis explores new methods to program strain into polymer sheets and stimuli – both new (microwaves, hot air) and existing (light, heat) - for actuating self-folding.

We studied the use of microwaves to self-fold thin pre-strained polystyrene (PS) sheets. While the PS sheets are transparent to microwaves, patterns of screen-printed ink containing graphene and iron oxide absorb microwaves and cause the underlying printed sections of the sheet to warm up. When the local temperature in the inked region exceeds the glass transition temperature (T_g) of PS ($\sim 103^\circ\text{C}$), the strain in the inked regions of the film relaxes gradually across the sheet thickness, which causes the PS sheet to fold. The resulting dihedral angle is proportional to the width of the hinge printed by graphene ink. The folding angle is the angle between two panels adjacent to a hinge and the dihedral angle is its supplementary angle (the sum of two supplemental angles is 180°). The geometry and azimuthal orientation of the sample inside the microwave reactor affect the quality of the folding due to the non-uniformity of the microwave energy inside the reactor. This study is the first to use microwaves to induce self-folding.

We also created a simple approach to self-fold commercially available, millimeter-thick thermoplastic polymer sheets. The process begins by first stretching poly(methyl methacrylate) (PMMA), polycarbonate (PC), or PS sheets using an extensometer at elevated temperatures close to the T_g of each sheet. Localizing the strain to a small strip creates a “hinge,” which folds in response to asymmetric heating of the sheet. Although there are many ways to supply heat, here a heat gun delivers heat to one side of the hinge to create the necessary temperature gradient through the polymer sheet. When the local temperature exceeds the T_g of the polymer, the strain in the hinged region relaxes. Because strain relaxation occurs gradually across the sheet thickness, the polymer sheet folds in the direction towards the heating source. A simple geometric model predicts the dihedral angle of the sheet based on the thickness of the sheet and width of the hinge. We report for the first time that this approach to folding works for a variety of thermoplastics using sheets that are significantly thicker (~10 times) than those reported previously.

We also demonstrated a self-folding system that mimics joints in the human body. Stress from pre-strained elastic filaments trigger folding of a plastic sheet when uniform heat softens the sheet. The folded objects revert to 2D sheets at elevated temperatures. These sheets can be folded reliably, reversibly, and repeatedly to create final shapes dictated by the placement of the tensile elements (rubber bands). A model based on the law of cosines predicts the dihedral angle as a function of the strain of the rubber band. A thermo-mechanical model predicts dihedral angle as a function of the pre-strain of the tensile elements. It is also possible to further program the materials to change how the samples unfold; allowing the samples to unfold into a complex shape the sheet previously held. This system can predict and precisely control converting 2D sheets to 3D objects using only commercially available materials.

Lastly, we created a new fabrication system using heated compression of polymer sheets to manufacture strained polymers from planar, unstrained thermoplastic sheets. After straining these materials can self-fold into complex geometries when exposed to external stimuli and can fully recover their initial geometry when heated uniformly. Digital Image Correlation (DIC) is used to measure the strain profile within the strained samples while a Mooney-Rivlin model and geometric model predict the average strain and folding response of our samples, respectively. Complex geometries are attained experimentally with both thick (~12 mm) and thin (~ 1 mm) strained polymers. The techniques presented here should work with many thermoplastic, thus increasing the available pool of polymers for self-actuating devices made from commercially available thermoplastics.

© Copyright 2017 Duncan Sherwood Davis

All Rights Reserved

Self-Folding of Thermoplastic Polymer Sheets from 2D to 3D

by
Duncan Sherwood Davis

A dissertation submitted to the Graduate Faculty of
North Carolina State University
in partial fulfillment of the
requirements for the degree of
Doctor of Philosophy

Chemical Engineering

Raleigh, North Carolina
2017

APPROVED BY:

Jan Genzer
Committee Co-Chair

Michael Dickey
Committee Co-Chair

Kirill Efimenko

Yong Zhu

DEDICATION

This dissertation is dedicated to my parents, my siblings, and my wife. Their support, love, and encouragement inspire me endlessly.

BIOGRAPHY

Duncan Davis grew up in Cranston, Rhode Island. He earned his Bachelor of Science degree in Chemical Engineering at Case Western Reserve University. While there, he fell in love with polymers; he took multiple polymer science courses, conducted independent research in polymer synthesis with Dr. David Schiraldi, and worked at a cooperative education internship synthesizing various copolymers at the Bridgestone Center for Research and Technology. Following his undergraduate studies, he moved to Raleigh, North Carolina to pursue his doctoral degree at North Carolina State University (NCSU). Here, he is co-advised by Dr. Michael Dickey and Dr. Jan Genzer. He studies self-folding techniques using microwaves, infrared light, asymmetric heat, and uniform heat to convert 2D sheets to 3D objects.

ACKNOWLEDGEMENTS

Jan Genzer and Michael Dickey, my advisers, are the best professors a student could have. I am grateful for the attention and guidance they have given me. They challenge me to grow and improve as a researcher more than I knew I could. They patiently helped me develop as a scientific writer, to channel my academic excitement into promising results, to persevere and benchmark my work appropriately, and to see the big picture. They inspire me to maximize my efforts and abilities.

Thank you to Kirill Efimenko and Yong Zhu for serving as my committee members and giving their valuable advice, expertise, time, and critical evaluation of my work.

Thank you to my peers and colleagues who have helped me along the way. Amber, Russ M., and Ying, the folding sub-group, are amazing colleagues and people. They push me to be inventive and helped solve all the problems that came my way. They are a brilliant team!

Thank you to my research groups, both of which provided critical feedback and laughs along the way. Thank you, Gilbert, Matt, Yiliang, Preeta, Julie, Collin L., Dan, Jason, Ko, Chris, Russ S, Steven, Shreya, Kunal, Sean, Casey, Robin, Rohan, Edwin, Phil, Collin E., David, Dishit, Ishan, Minyung, Taylor, Tim, Daniel, Mohammed, and Rashed. I am blessed to have such amazing colleagues.

Thank you to my EFRI collaborators, Susan, Kelly, Sally, Alan, and Jianxun, for their excitement about origami, professional knowledge, and photography expertise. Our monthly Friday afternoon meetings are always the highlight of my month.

I would like to thank Elton, Bin, and Ben, my undergraduate assistants, for working on various projects with me. I am lucky to have clever, hard-working, undergrads helping me with research.

I would also like to thank Dr. Gregory N. Parsons, Dr. Christopher Gorman, Dr. Saad Khan, and Dr. Wesley Henderson for allowing me use instruments in their labs. I also

appreciate the support from the Chemical Engineering staff, especially Joan O'Sullivan for the great conversations and equipment safety help.

Here in Raleigh, my friends have given me so many memories. Thank you for all the great times, Jordan, Talina, Eugene, Laura, Jonathan, Erica, Wes, Preeta, and Vivek. I would also like to thank Triangle Ultimate for keeping me active throughout my tenure.

My family has supported me through thick and thin. My parents always show an interest in whatever inspired me and taught me that I could achieve anything if I put in the time and effort. They encourage me through so many projects, recitals, exams, and even helped me start my own business – Sherwood Games. My siblings help me become the best version of me. They always challenge me to be better than the day before. I am lucky to have such wonderful people in my life. I would also like to thank my grandfather, Vic, for pushing me to pursue a Ph.D. He nurtured my interest in higher education from a young age. As a professor, he sparked my excitement in academia by sharing his experiences with me. I strive to live up to his shining example.

My wife Jackclyn is the best partner a person could have. She inspires me to be better every day. Her compassion, work ethic, and love keep me motivated and inspired. Even in the darkest moment, she is the light that guides my way.

Lastly, I acknowledge the Emerging Frontiers in Research and Innovation program as the National Science Foundation for funding my research. Thank you for supporting innovation, development, and growth in science and learning.

TABLE OF CONTENTS

LIST OF TABLES.....	viii
LIST OF FIGURES.....	ix
CHAPTER 1 Origami in Science: A Review of Hands-On and Hands-Off Techniques	
1.1 Introduction.....	2
1.2 Hands-on Folding.....	5
1.3 Hands-off Folding.....	10
1.3.1 Light and Heat Actuation.....	11
1.3.2 Other Actuation Methods.....	21
1.4 Summary.....	29
References.....	31
CHAPTER 2 Self-folding of Polymer Sheets Using Microwaves and Graphene Ink	
2.1 Introduction.....	41
2.2 Experimental System with Graphene Ink and Geometric Model.....	43
2.3 Azimuthal Orientation Effect of Folding.....	45
2.4 Thermally Modelled Simulation Results.....	50
2.5 Conclusion.....	52
2.6 Acknowledgements.....	53
Supporting Information.....	54
References.....	58
CHAPTER 3 Self-folding of Thick Polymer Sheets Using Gradients of Heat	
3.1 Introduction.....	65
3.2 Geometric Model.....	69
3.3 Self-folding in Asymmetric Heat.....	70
3.4 Thermal Model.....	75
3.5 Conclusion.....	78
3.6 Acknowledgements.....	78
Supporting Information.....	79
References.....	87
CHAPTER 4 Repeatable Reversible 2D to 3D Bilayer Shape Programming	
4.1 Introduction.....	92
4.2 Experimental Results – One Hinge Samples.....	95

4.3 Experimental Results – Complex Samples.....	97
4.4 Experimental and Results – Modular Origami.....	97
4.5 Modeling Results – Balancing Forces.....	99
4.6 Method to Reprogram Unfolding.....	102
4.7 Conclusion.....	103
4.8 Acknowledgements.....	104
Supporting Information.....	105
References.....	110

CHAPTER 5 Compressed Thermoplastic Polymers for Fabricating Tunable Self-Folding Devices

5.1 Introduction.....	114
5.2 Digital Image Correlation – Strain Quantification.....	117
5.3 Experimental Conditions.....	120
5.3.1 Thick Sheets.....	121
5.3.2 Thin Sheets.....	122
5.4 Mooney-Rivlin Model.....	125
5.5 Geometric Model.....	128
5.6 Conclusion.....	131
5.7 Acknowledgements.....	132
References.....	133

CHAPTER 6 Summary and Future Outlook

6.1 Summary.....	136
6.2 Future Outlook.....	138
6.2.1 Chemical Folding.....	138
6.2.2 Melt Press - Future Work.....	139
6.2.3 Children’s Toy / Folding Kit.....	140
6.2.4 Optical Applications for the Folding Driven by Elastic Filaments.....	141
6.3 Final Thoughts.....	142

LIST OF TABLES

Chapter 1

Table 1.1. All self-folding techniques discussed in this review organized by stimulus and compared using various folding properties.....4

Chapter 3

Table 3.1. Folding attributes of tested materials.....77

Table S3.1. Physical characteristics of polymers.....86

Chapter 5

Table 5.1. Constants for the Mooney-Rivlin Model.....126

LIST OF FIGURES

Chapter 1

- Figure 1.1.** Folding patterns to collapse a sheet. (a) This folding pattern does not account for thickness, so hinge location and design do not matter. It can collapse without any changes to the hinge or sheet. (b) This folding pattern uses a shifted rotational axis to ensure the axis of rotation in the hinge is always on the same side as the folding direction. This change allows the sheet to collapse when accounting for sheet thickness. (c) This folding pattern uses gaps in the hinge to make space for the sheet thickness when collapsed. Using gaps allows the sample to fold completely when accounting for sheet thickness¹⁴. This collection of characteristics describes the parameter space for different types of folding in rigid-foldable origami.....**6**
- Figure 1.2.** Engineers designed a 19 mm thick wooden sheet that folds into a table. This table uses a folding pattern from **Figure 1.1** to create stable folded and unfolded shapes¹⁴.....**7**
- Figure 1.3:** A foldable circuit board fabricated from 1.6 mm thick metal panels connected by reversibly folding mechanical hinges¹⁴.....**8**
- Figure 1.4:** A symmetric folding pattern composed of three valley folds and one mountain fold. This sheet uses plates with two different thicknesses to control the maximum folding angle and geometry of the fully folding shape¹⁷. Scale bar is 20 mm.**9**
- Figure 1.5:** A partially folded solar panel array fabricated from concentric rings for space applications. Additional rings greatly increase the unfolded surface area while only slightly increasing the stowed diameter¹³. The scale bar is ~1 m.**9**
- Figure 1.6.** (a) Prestrained polystyrene shapes simultaneously self-fold into a variety of complex shapes using a combination of black ink and IR light⁵². (b) Prestrained polystyrene coated with grey hinges self-fold into a polyhedron in response to IR light. Changing the darkness of the hinges controls the absorption of IR light and the sequence of folds⁵⁵. (c) Prestrained polystyrene self-folds sequentially in response to LED light. By matching the LED light color to the absorption profile of the hinge color, scientists fold exclusively one hinge at a time⁵⁶.**12**
- Figure 1.7:** The fabrication method to make a photo-induced self-folding box. (a) A photomask used to pattern the hinges for a box. (b) Experimentally folded box. (c-e) Simulation results that predict a closed box and an open box⁶⁵.**14**
- Figure 1.8.** (a) Prestrained polystyrene sheet self-folds in response to a laser radiating across its surface, creating a hinge. (b) Once the laser hits the surface, the sample folds to 90° in 4 seconds⁶¹.**15**
- Figure 1.9.** The schematic shows the possible unfolding pathways for a polymer composite filled with Fe₃O₄ and CNT nanoparticles. The polymer is divided into 3 regions; CNT-rich, polymer only, and Fe₃O₄-rich. The polymer is manually deformed into TS1 and unfolded using different frequencies of RF waves. If uniform heat is applied, the sample recovers to form the original flat sheet in the center⁵⁸. There are five recovery routes based on the order in which stimuli are applied.**17**
- Figure 1.10:** Polystyrene coated with graphene ink folds in response to microwaves⁵⁷. The pattern, the experimental sample, and the thermal image taken with an infrared camera are

shown for two different geometries at azimuthal angles of 0°, 45°, and 90°. The azimuthal angle determines the type of folding and the heating profile.18

Figure 1.11: Schematic of fabrication and experimental results for a polymer-metal composite self-folding system. (a,b) Self-folding sheet with multilayer patterned panels shown in pre-and post-folding positions. (c-g) Step-by-step fabrication of polymer-metal composite. (h-l) SEM images of a self-folded cube before and after folding. (m-q) SEM images of the Sn hinges fusing together to reinforce the structure after folding⁸⁰.19

Figure 1.12: (a) The thermoplastic is locally deformed to create a hinge, then self-folded, then recovered in uniform heat. This cycle can be repeated. (b) A heat gun warms the surface of the polymer until the sheet folds. (c) Schematic for programming a thermoplastic polymer to fold in response to a gradient of heat⁸³.20

Figure 1.13. (a) The T_g of the hinges are controlled locally by reacting the PFS/M co-polymer with different concentrations of M_2 reagent. (b) The substrate is thermally programmed at various temperatures to choose which shapes it will take when folded. (c) The sheet is heated from 25 to 65 °C, actuating each hinges individually⁸⁵.22

Figure 1.14: (a) Schematic depicting a method used to fabricate the SU8/elastomer bilayer. (b-d) Finite element analysis predicted folding a pyramid, cylindrical shell, and ‘windmill’ (left). These shapes were fabricated (right)¹¹³.24

Figure 1.15: Pneumatically actuated tentacles⁸⁶ (a-b) and hands¹¹⁵ (c). Both devices flex from inserting pressurized air into the hollow center of the device. The hands can also synchronize with an external glove to precisely control actuation with finger movements.....25

Figure 1.16: PDMS sheets patterned with magnetic dipoles self-folded into 3-D structures when placed into a magnetic field⁹⁰.26

Figure 1.17: A composite of paper, prestrained PO, prestrained PS, and a copper circuit etched into polyimide self-folds into various 3D shapes via joule heating. A pyramid (A-B), a box with a tab lock (C-F) and a crane (G-H) were all fabricated with this method through a combination of sequential and simultaneous folding⁹⁴.27

Figure 1.18. The Venus flytrap uses a snap-through mechanism to fold 180° in less than one second¹⁰⁰. (a) The Venus flytrap before and after actuation. (b) Stereo imaging showing fluorescent dots on the leaf surface. (c) Mesh pattern of the leaf closing using color to show local curvature (blue is more curved than red). The spatially averaged mean curvature (d) and the Gaussian curvature (e) showing the snapping reaction as a function of time.....29

Chapter 2

Figure 2.1. Folding process induced by microwaves (not to scale). A pre-strained polystyrene sheet (a) is screen-printed with graphene ink on the surface of the sheet (b); the printed regions define a ‘hinge’. Microwaves heat the ink (c); the microwave source is physically positioned on the right side of the sample, but is designed to create a standing wave inside the vessel of the microwave reactor. The sample folds to α_D due to the localized heating of the inked region in the sample via absorption of microwaves (d).44

Figure 2.2. The maximum dihedral angle (α_D) increases with increasing hinge width (W). The samples are 6 mm wide in the dimension parallel to the hinge.45

Figure 2.3. Dihedral angle (α_D) as a function of the hinge width (W). The error bars capture the first standard deviation with a minimum of 3 repetitions of each hinge width with all other variables held constant. These samples are all exposed to a microwave power of 250 W, an orientation of 90°, and a square-shaped hinge composed of graphene ink (see text).....**45**

Figure 2.4. Two sample geometries ('diagonal hinge' and 'square hinge' groups) are depicted at 3 different sample orientations (columns) relative to the direction of the microwave source. The top row of each group is a cartoon of the sample, the middle row contains photographs of samples after exposure to 3 s of microwave, and the bottom row is an IR image of the sample slightly before it begins to move in response to microwaves (with the temperature scale on the right side).**46**

Figure 2.5. Time-dependence of temperature in a) 'diagonal hinge' samples with varying orientation and hinge width of 3 mm; b) 'square hinge' samples with hinge width of 3 mm. The microwave power is 250 W in both cases. The IR camera cannot measure accurately temperatures above 150°C and therefore the data truncates at that value.**48**

Figure 2.6. Heating rate of the samples at different orientation relative to the direction of the microwave radiation (azimuthal angle) and hinge widths (W) are shown.**48**

Figure 2.7. Microwave sensitive paper changes color when heated by microwaves to show the non-uniformity of microwaves. Depictions of the polymer samples are superimposed over the paper for the sake of visualization. The microwaves heat non-uniformly, which explains why the hinges at 90° orientation fold and 0 and 45° deform, as shown in the photographs located in the right-most column.**50**

Figure 2.8. Results from Abaqus model that show the temperature profile on the surface (top view) and through the thickness of the samples (side view) oriented at 90°. The images truncate the regions outside the hinge region for better visualization of the thermal profile of the hinge. The side view images are expanded to the distance 'A' and 'B' (which are equal). The black portion of the image is the edge of the unheated polymer.**51**

Figure S2.1. Optical microscopy of the screen printed graphene. There are grid lines from the screen as well as the high level of uniformity in the ink pattern.**55**

Figure S2.2. Profilometry of screen printed Vor-ink™ (3 mm hinge width). The hinge size varies from 50 to 100 μm for most peaks in the sample with the maximum being over 130 μm**55**

Figure S2.3. Heating profile for a 'rectangular hinge' (6 mm, 250 W, 45° orientation). The pictures are taken with an IR camera and show how the hinge heated non-uniformly. This lack of uniformity in the profile leads to imperfect folding. The camera view is flipped, so the directional heating is left to right instead of right to left. This sample folds in ~6 second. The microwave is then turned off. (*Note that the first 2 images do not use the same temperature scale in order to increase visibility of the sample and hinge*). The temperature range (in °C) is show in the legend on the right.**56**

Figure S2.4. Thermal Images of square hinge samples. Even though the heating rate is similar, the orientation controls whether the sample craters or folds. This is likely because the hot region spans the width of the hinge in the 90° sample (without bound) but is bound by stiff polymer in the 0° case. The temperature range (in °C) is show in the legend on the right.**56**

Figure S2.5. Heating profile of a 3 mm 250 W sample (experimental) and the *tanh* fit. Using this fit we found the maximum heating rate via the inflection point of the derivative.....**57**

Figure S2.6. Heating rate of the samples ($W = 6$ mm) at different microwave powers and orientation relative to the direction of the microwave radiation (azimuthal angle).....**57**

Chapter 3

Figure 3.1. Process for self-folding. a) Locally prestraining a polymer sheet creates a hinge. Selective heating of one side of the ‘hinge’ causes asymmetric strain relaxation that induces folding. When applied uniformly, heat causes unfolding and the sample reverts to the original shape. The full cycle causes some permanent deformation, but the focus here is on the folding step. b) Schematic of the preparation steps using an extensometer. A picture of the setup is in **Figure S3.1** the SI. c) A heat gun asymmetrically heats one side of the prestrained polymer sheet to induce self-folding.**68**

Figure 3.2. A geometric model predicts the folding angle α_F of commercial prestrained sheets⁴⁹. Grips from an extensometer start at a distance W_i apart and strain the sample a distance W_s . The straining causes the sample to shrink in the hinged region. Heat delivered to the top of the sample causes the top of the sample to shrink and therefore the sample folds. In our system, $W = (W_i + W_s)$**69**

Figure 3.3. Photographs of self-folding samples. a) PMMA samples with thickness ranging from 1.5 to 12 mm. b) PS samples with λ from 1.33 to 2.67. c) PC samples exposed to the heat gun for 30 to 45 s. d) A PMMA sample folded to $\alpha_D \sim 180^\circ$ that is supporting a 9 kg weight demonstrates the strength of the folded samples.**71**

Figure 3.4. a) Experimental data (symbols) and geometric model predictions (lines) of α_D vs λ for varying thicknesses of PMMA. b) Experimental data (symbols) and geometric model predictions (line) of α_D vs λ for 2.0 mm thick PMMA, PS, and PC. c) Data from **Figures 3.4a** and **3.4b** plotted as a function of the arctan function from the geometric model. The black line denotes prediction from Equation 3.3.**73**

Figure 3.5. Temperature (red-solid line, left ordinate) and dihedral angle (blue-dashed line, right ordinate) as a function of heating time overlaid with the surface temperature profile of the same sample. The PMMA starts folding after the surface exceeds T_g ($\sim 105^\circ\text{C}$) for 1.5 mm (b), 2.0 mm (c) and 3.0 mm (d) thick samples. Samples of PMMA that are 3.0 mm thick start folding after the surface reaches T_g**74**

Figure 3.6. The top of each pair show the model’s prediction of temperature profiles inside the sheets: PMMA 1.5 mm (left), PMMA 2.0 mm (middle), and PMMA 3.0 mm (right). The bottom of each pair denotes the temporal evolution of the temperature on the front side (red line) and the backside (blue line) of the sample.**76**

Figure S3.1. Experimental setup for programming strain in polymer sheets in an extensometer. There are two metal grips in the center of the oven that pull the sample vertically while the four infrared lamps control the temperature with an error of $\pm 1^\circ\text{C}$. The metal grips each have two screws that secure the sample.**79**

Figure S3.2. Temperature profiles of the hinge region of PS, PC, and PMMA (all thicknesses) as a function of time. We use an infrared camera to measure the temperature of the hinge while the material folds. The heat gun starts heating the sample at time = ~ 2 seconds....**80**

Figure S3.3. Dihedral angles calculated using the Almansi (blue lines) and Swainger (green lines) strains as a function of extension ratio (λ) using the model given by Equation 3.1 in the main text. The symbols represent the experimental data collected from PMMA sheets with thicknesses 1.5 mm (a), 2.0 mm (b) and 3.0 mm (c).82

Figure S3.4. Temperature (red-solid line, left ordinate) and the dihedral angle (blue-dashed line, right ordinate) as a function of time of PS (upper - thickness 2.0 mm) and PC (bottom - thickness 2.0 mm). The material starts folding at around the time the surface of the sheet reaches T_g (~103 °C for PS and ~147 °C for PC).83

Figure S3.5. The top of each pair show the model's prediction of temperature profiles inside the sheets: PS 2.0 mm (left), and PC 2.0 mm (right). The bottom of each pair denotes the temporal evolution of the temperature on the front side (solid red line) and the backside (dashed blue line) of the sample.85

Chapter 4

Figure 4.1. Schematic of the self-folding method using rubber bands. (A) A rubber band of initial length L_0 is stretched across the hinge region to length L , extended through the PMMA sheet, and secured with metal clips. The sample is placed in an oven at 130 °C until the increased temperature makes the thermoplastic hinge soft enough to allow the rubber band to relax back to L_0 , folding the sample to a dihedral angle (α_D). If the rubber bands are removed and the sample is reheated at 130 °C, the sample unfolds back to its original shape, or 'base shape,' regardless of which new shape it occupies. (B) Starting with a flat shape with multiple hinges, the sample sequentially folds into two different shapes. When the rubber bands are removed and the sample is heated again, it will unfold into the original shape. (C) The sample can be strained and heated to 170 °C to change which shape it will return to when it is unfolded. With the additional heating step, the sample behaves the same as the sample in B except it unfolds to the intermediate shape instead of the original flat sheet. Compare the last to steps of (B) and (C) for a side by side comparison.94

Figure 4.2. (A) Folded 2 mm thick PMMA sheets showing the effect of strain on dihedral angle. (B) This plot uses the extension ratio of the rubber band to accurately predict the dependence of dihedral angle based on Equation 4.2.96

Figure 4.3. Complex shapes (A) and a series of modular shapes (B). The pyramids, cubes, planes, birds, and cranes were folded by designing a series of flat samples with hinges across the regions that need to fold. The modular patterns contained two different base shapes, a hex pattern and a cross patterned box which each fold into a variety of different shapes shown below the base images. The hex pattern can fold into a cylinder, a flat line, and a fully collapsed cell. The cross patterned box can fold into an offset cylinder, a flat square, and a fan. By connecting the rubber bands to different areas, even more shapes can be discovered from the same base patterns. Both sets of shapes were cut and ablated with a laser writer and folded in an oven at 130 °C.98

Figure 4.4. (A) The model predicts the α_D at the point when $F_S=F_R$ as a function of t_h (solid, rainbow) and T . Above a critical onset temperature, the sheet will fold. (B) $\frac{d\alpha_D}{dT}$ plotted as a function of temperature. This figure shows the T when α_D drastically increases. There is a major and minor relaxation in the sheet. The major relaxation predicts the onset folding. (C) Using this model, we predict the temperature at the onset of folding and compare the model to experimental data. The experimental data was taken by heating a sample to a temperature, holding it at that temperature for a given duration and then slowly ramping the temperature up

until the samples folded. In these experiments, we noticed that once a sample folded a certain amount, it would continue folding to the maximum angle predicted in **Figure 4.2**.....101

Figure 4.5. Using the programming methods shows in **Figure 4.1**, here are the experimental results for the folding method (A), the reprogramming method (B), and the side by side comparison in the oven (C). The reprogramming method contains an extra heating step that anneals PMMA in a high heat while preventing the shape from changing with a metal weight. This extra step allows the sample to relax and resets the base shape. Instead of reforming the initial shape (hex pattern) upon additional heating without rubber bands, it relaxes back to the intermediate shape (flat pattern).103

Figure S4.1. The contraction force in the rubber band calculated with an extensometer co-plotted with F_c from the balance of forces model. F_c does not predict the rubber band behavior perfectly, so it will cause some errors in ability of the model to predict the temperature at the onset of folding. The force balance model was calculated with an extension ratio of 3 to minimize these errors.106

Chapter 5

Figure 5.1. Schematic to produce strained sheets compressed with a melt press. If these sheets are put under a heat gun (red) or an IR light (orange), they will self-fold. All samples of varying thicknesses and polymer compositions were initially cut into a 75 mm diameter disk using a laser cutter and melt pressed at an elevated temperature (below the glass transition temperature of each sheet). The strained samples then were either modified using hinge ablation (via laser cutting for sample thickness >1 mm) or ink addition (via China Marker for sample thickness <1 mm). An asymmetric temperature profile induces self-folding in the thick and thin samples via a heat gun or local light absorption, respectively.116

Figure 5.2. Example images depicting pre- and post-strained PMMA sheets (A). DIC derived strain profiles of PMMA and PS samples in the X and Y directions (E_{xx} and E_{yy} , respectively) as a function of applied force in the melt press (B). The colored scale bar represents a breadth of strain (mm/mm) imparted to the sample. The scale bars are 20 mm.119

Figure 5.3. Images on the left show the 2D patterns that self-fold into the 3D structures created from thick PMMA (~12 mm, middle) and thin PS (~1 mm, right) sheets. We created a range of complex geometries including pyramids (top), open boxes (middle), and closed boxes (bottom) using both thick and thin self-folding. Note that both the thick and thin folding can be produced with a polymeric material other than the ones demonstrated here (i.e., the thick and thin folding materials can be reversed).122

Figure 5.4. UV-Vis shows that China Marker absorbs ~98% of IR light compared with printed black ink and manually applied black ink which absorb ~73% and ~82%, respectively.....124

Figure 5.5. The Mooney-Rivlin model correlates the force applied in the melt press to the radial extension ratio (λ_R) post-melt pressing. Using this model, an end user can predict the strain in their sample using only the applied force and the surface area of the disk. The PMMA has a starting thickness of 12 mm. The PS was modeled at two different thicknesses: 6 mm and 1 mm. All samples have a diameter of 75 mm.127

Figure 5.6. λ_R of a sheet strained in the melt press plotted as a function of starting sheet thickness for PMMA and PS. The applied force was 6 metric tons in all cases. λ_R does not depend on thickness for PMMA but does effect PS.128

Figure 5.7. A geometric model is used to predict the folding angle as a function of hinge width for PS (left) and PMMA (right). (A-B) We use the geometric model to predict the folding angle based on the applied force in the melt press. This model only accounts for geometry, so any nonuniform strain profiles produced in the melt press will result in deviation. (C-D) Since force does not perfectly correlate to the amount of strain in a particular region of the sheet, the data from A-B is replotted as a function of strain. This plot shows that despite the high variance in the system, the geometric model predicts the dihedral angle relatively well. (E-F) The predicted dihedral angle vs. the experimentally measured dihedral angle demonstrates a reasonable fit with a near-linear trend line.130

CHAPTER 1

Origami in Science: A Review of Hands-On and Hands-Off Techniques

1.1 Introduction

This chapter reviews origami-inspired folding techniques that convert two-dimensional (2D) sheets into three-dimensional (3D) objects. These folding methods are organized into two categories: hands-on and hands-off. Hands-on techniques use manual manipulation of materials to induce folding, such as folding and unfolding a collapsible table. These techniques require manual manipulation and are independent of the material used; examples involving wood, metal, and plastic sheets will be discussed. Hands-off or hands-free folding techniques use an external stimulus to actuate motion, such as using a magnet to move a paper clip. Techniques using external stimuli to actuate motion are material dependent. This Ph.D. dissertation focuses on self-folding polymer sheets, thus only self-folding thermoplastic or elastomeric polymers will be discussed.

This review has three goals: (1) Survey the state of the art and future opportunities for hands-on and hands-off folding techniques. (2) Discuss stimuli that can induce self-folding, and (3) Compare hands-on and hands-off folding to identify relative strengths and weaknesses between the methods.

Converting 2D sheets into 3D objects is appealing for manufacturing, shipping, and storing objects since flat sheets occupy minimal space. There are many methods to manufacture 2D sheets cost-effectively. Examples include, casting, machining, melt pressing, molding, coating, or extruding.

Origami, the Japanese art of paper folding, is often a source of inspiration for converting 2D sheets into 3D shapes. In the field of origami, there are two types of folds: mountain or valley. Mountain folds elevate the hinge above the sides of the paper and valley folds elevate the sides of the paper above the hinge. For systems with an external stimulus, we define valley folds as folds that face toward the external stimulus and mountain folds as folds that face away from the external stimulus. External stimuli include heat, lights, lasers, and microwaves.

This Ph.D. dissertation focuses on thermoplastic polymers. Therefore, this introductory chapter excludes the research areas involving hydrogels, shape memory alloys, and other adaptive materials. The topics not included here are reviewed elsewhere¹⁻¹².

Table 1.1 compares all folding techniques presented here using metrics that define the capabilities and limitations of each technique. We will evaluate each technique based on their maximum dihedral angle (see below), if they can form both mountain and valley folds in the same sample, if they can fold sequentially and/or reversibly, and whether they can control curvature in the hinges when actuated.

Maximum dihedral angle is important because it limits what shapes are possible. The folding angle is the angle between two panels adjacent to a hinge and the dihedral angle is its supplementary angle (the sum of two supplemental angles is 180°). Many techniques can fold to the maximum dihedral angle of ~180°.

Some complex shapes require both mountain and valley folds to fabricate. Techniques that can only fold mountain or valley folds are restricted to making shapes with all interior hinges like cubes and pyramids.

Sequential folding is important to forming 3D shapes where hinges are folded in a pre-programmed order or sequence. In origami, all folds are sequential, so mastering this attribute allows the technique to mimic origami folding patterns more closely.

Reversible folding allows the same 3D form to fold and unfold multiple times. This property improves the functionality of the device and enables fabrication of products like folding chairs and tables. For hands-off techniques, reversibility enables the creation of reconfigurable self-folding devices.

Some shapes require curved hinges or panels. If a technique can control the curvature in a sheet, then devices inspired by nature and shapes without sharp edges become possible to fabricate.

Table 1.1. All self-folding techniques discussed in this review organized by stimulus and compared using various folding properties.

Stimulus type	Material	Figure Number in this chapter	Sheet Thickness scale	Sheet Length scale	Maximum dihedral angle (deg)	Valley & mountain folds	Sequential folding	Reversible folding/unfolding	Can generate curves
Manual actuation	Plastic, metal, wood, or composite	1.2, 1.3, 1.4, 1.5	mm	m	180	✓	✓	✓	
IR/LED light	Prestrained PS coated in ink	1.6	μm	mm	180	✓	✓		✓
Photo-Reaction	PETMP-MDTVE-EGDMP copolymer	1.7	μm	mm	120				✓
Laser	Prestrained PS coated in black ink	1.8	μm	mm	90	✓	✓		✓
RF waves	Polymer-metal composite	1.9	μm	mm	180	✓	✓		
Microwaves	Prestrained PS	1.10	μm	mm	180				
Heat	PMMA with metal hinges	1.11	nm	μm	90		✓		
Heat	PMMA, PS, and PC	1.12	mm	mm	180		✓		✓
Thermal-chemical	PFS/M copolymer	1.13	μm	mm	180	✓	✓	✓	✓
Chemical removal of sacrificial layer	SU8-elastomer bilayer	1.14	μm	mm	180	✓		✓	✓
Pneumatic	Ecoflex-PDMS bilayer	1.15	μm	mm	180	✓	✓	✓	✓
Magnetism	Magnetic dipole patterned PDMS	1.16	μm	mm	<90			✓	✓
Resistive heating	Prestrain polymer-paper composite	1.17	μm	mm	180	✓	✓		
Biological Response	Venus FlyTrap	1.18	μm	mm	180			✓	✓

1.2 Hands-On Folding

Hands-on folding uses origami principles to create various 3D objects. Origami can create many different shapes by manually folding a sheet of paper. Origami-based principles inspired numerous researchers to use folding to create a new generation of shape changing materials. For example, satellites use hands-on folding techniques to prepare the device for launch by folding it into the smallest possible volume. Once the satellite reaches space, hands-off self-folding techniques aid in the deployment by unfolding the satellite into a device with the largest possible surface area¹³.

In rigid-foldable origami materials have rigid panels connected to flexible hinges. The mathematics behind rigid-foldable origami folding are not material specific and extend to metal, paper, polymers, and wood.

The hands-on techniques presented in this chapter were combined into a single entry in **Table 1.1** since they have the same advantages and disadvantages. For example, they can all fold to a dihedral angle of $\sim 180^\circ$ and make both mountain and valley folds in the same structure. They can all fold sequentially and reversibly. Their hinges are mechanical joints, so they cannot change the curvature in the sheet once the device is manufactured.

Several researchers have explored the effects of sheet thickness on folding^{14–18}. **Figure 1.1** shows the geometric relationship of folding a sheet into a flat object. If the thickness of a sheet does not affect its folding, the sheet folds ideally as shown in **Figure 1.1a**. When sheet thickness affects folding, the sheet cannot fold to 180° unless the hinge is modified or the sheet bends. Researchers suggest two ways to modify the hinges to allow 180° folding: changing the axis of rotation or adding gaps in the hinge region. The axis of rotation is where the sheet rotates when folding. If the axis of rotation is shifted to the surface of the hinge on the interior of the fold, the sheet can collapse into a flat object as shown on **Figure 1.1b**. If gaps are added into the hinge region, the sheet thickness will not affect the fold and the sheet can collapse into a flat object as shown in **Figure 1.1c**. The techniques shown in **Figure 1.1**

are used in the applications discussed in **Figure 1.2**, **Figure 1.3**, and **Figure 1.4** to create such macroscopic objects as foldable circuits and tables.

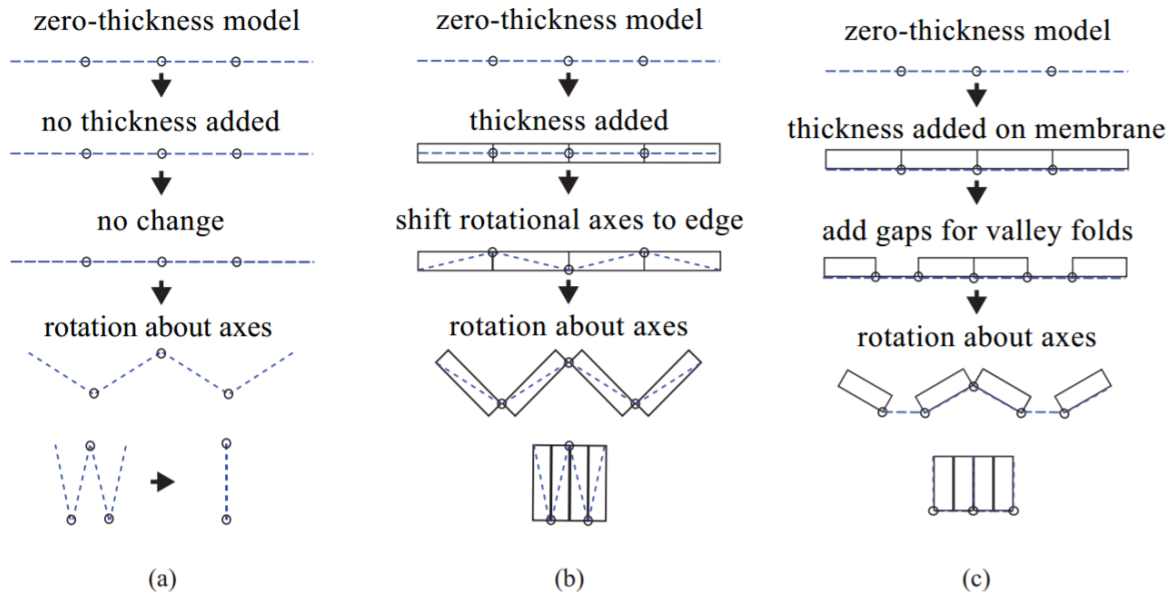


Figure 1.1. Folding patterns to collapse a sheet. (a) This folding pattern does not account for thickness, so hinge location and design do not matter. It can collapse without any changes to the hinge or sheet. (b) This folding pattern uses a shifted rotational axis to ensure the axis of rotation in the hinge is always on the same side as the folding direction. This change allows the sheet to collapse when accounting for sheet thickness. (c) This folding pattern uses gaps in the hinge to make space for the sheet thickness when collapsed. Using gaps allows the sample to fold completely when accounting for sheet thickness¹⁴. This collection of characteristics describes the parameter space for different types of folding in rigid-foldable origami.

There are currently several practical applications of hands-on folding. **Figure 1.2** shows a table that is delivered as a flat square and unfolds to become a table that seats eight people. Creating compact foldable tables demonstrates the power of applications inspired by origami.

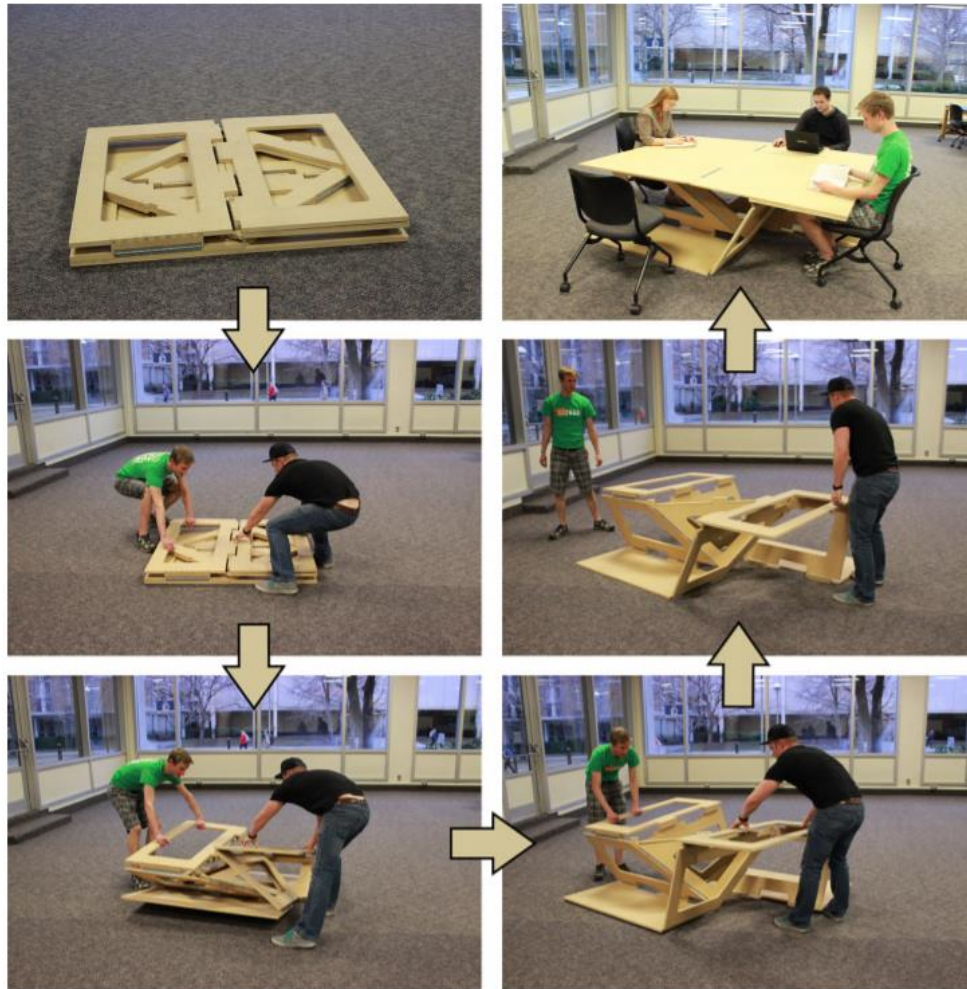


Figure 1.2. Engineers designed a 19 mm thick wooden sheet that folds into a table. This table uses a folding pattern from **Figure 1.1** to create stable folded and unfolded shapes¹⁴.

Figure 1.3 shows a foldable circuit board using mechanical hinges attached to the panels to allow collapsing into a Muira-ori fold. The Muira-ori fold is a pattern that allows a flat sheet to fully collapse into a smaller flat object, such as a folded map. Rigid-foldable origami was applied to the system using flexible metal hinges to pattern a fully collapsible circuit board. The Muira-ori folding pattern is one of the most difficult shapes to create because it requires mountain folds, valley folds, and reversible actuation. We speculate that any technique that can implement a Muira-ori folding pattern effectively can make many other 3D objects using the same properties.

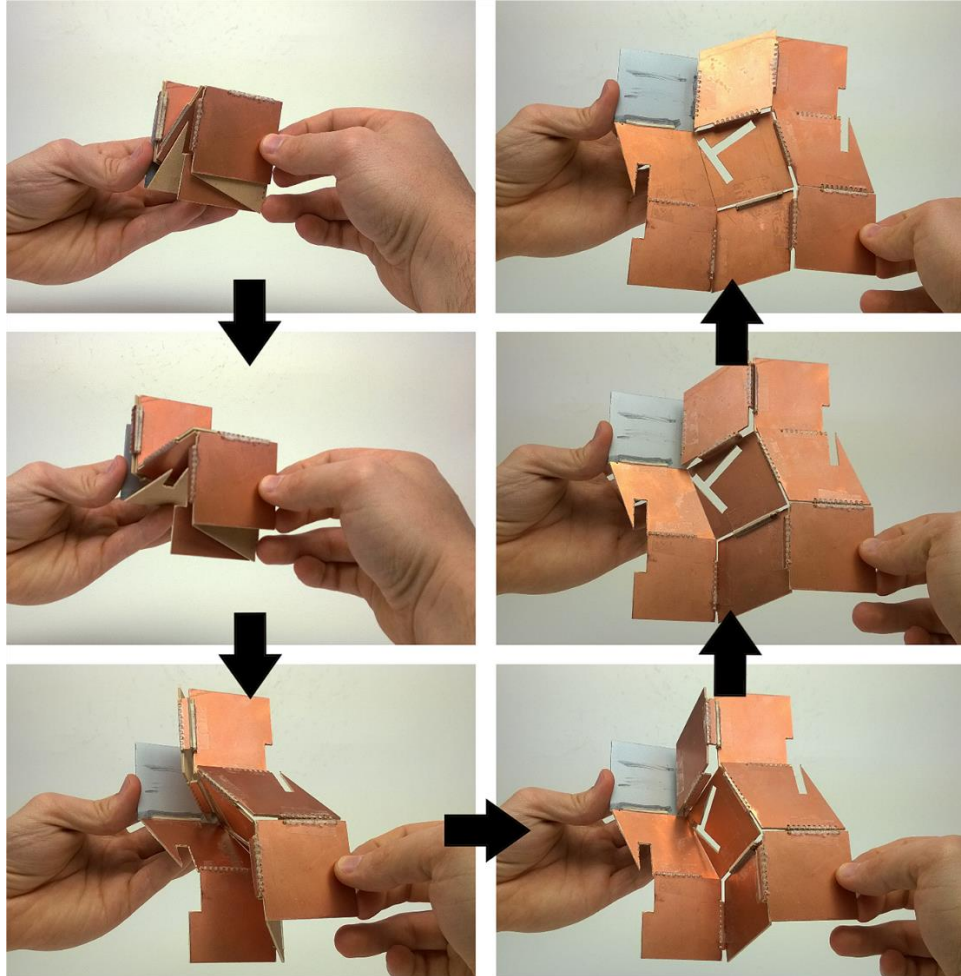


Figure 1.3. A foldable circuit board fabricated from 1.6 mm thick metal panels connected by reversibly folding mechanical hinges¹⁴.

Figure 1.4 shows a symmetric folding pattern with a central vertex connected to three valley folds and one mountain fold. This geometry has one degree of freedom (DOF); i.e., it converts from its flat state to its fully folded state with no structurally stable intermediate states. Structures made from repeating pieces of the same single DOF allow complex folding with easily actuated hinges. As hands-off techniques become more refined, these types of repeated geometries will become critical to fabricating complex structures without complicated hinges or folding patterns.

Figure 1.5 shows a foldable solar array of panels designed to be used in space. One of the most scientifically interesting applications of macroscopic origami is the conversion of

a small stowed structure into a large unfolded structure for space structure fabrication. Currently, the unfolding of this design is demonstrated in a hands-on manner, though it is meant to become a hands-off technology when implemented in space.

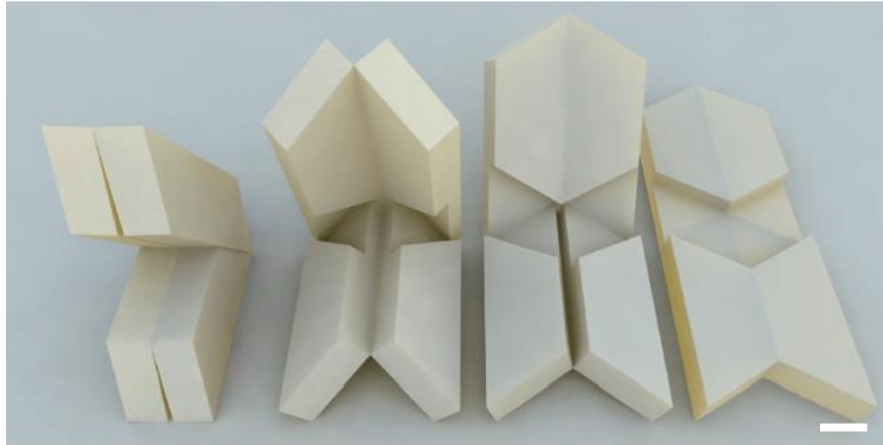


Figure 1.4. A symmetric folding pattern composed of three valley folds and one mountain fold. This sheet uses plates with two different thicknesses to control the maximum folding angle and geometry of the fully folding shape¹⁷. Scale bar is 20 mm.

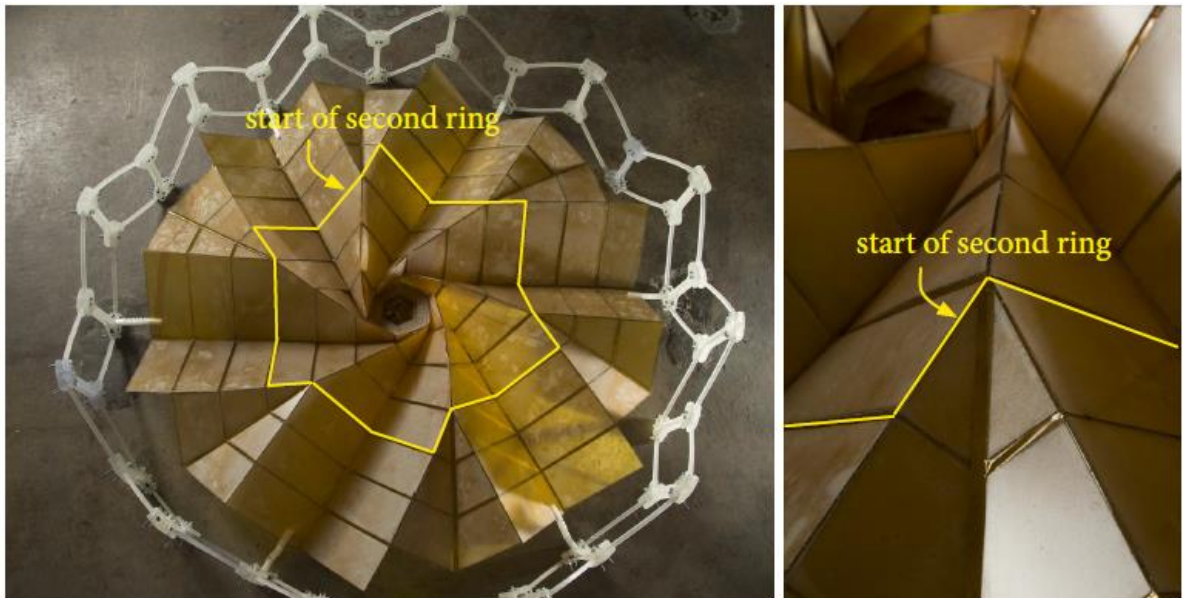


Figure 1.5. A partially folded solar panel array fabricated from concentric rings for space applications. Additional rings greatly increase the unfolded surface area while only slightly increasing the stowed diameter¹³. The scale bar is ~1 m.

Hands-on folding is useful for folding macroscopic objects, such as, chairs, tables, paper cranes, and cardboard boxes. Hands-on folding is material agnostic, mechanically simple, and used widely in industry and households. We want to improve hands-off folding until it reaches the same wide spread use as hands-on folding. Next, we will survey hands-off techniques that were used in origami inspired, self-folding applications.

1.3 Hands-off Folding

Hands-off folding uses an external stimulus to induce shape change in a material. This chapter focuses on hands-off folding of on thermoplastic and elastomeric polymers. We will review sheet thickness size scales ranging from macro (>mm) to micro (<mm). On the macroscopic scale, hands-off folding focuses on mimicking origami or implementing self-folding into specialized applications including flexible displays¹⁹, self-folding antennas²⁰, robotics hands or grippers²¹⁻²³, soft robotics²⁴⁻²⁹, photovoltaics and batteries³⁰⁻³², self-deployment³³⁻³⁵, space applications^{13,33}, and packaging^{36,37}. On the microscopic scale, researchers focus on precise control and geometries tuned to self-folding for biomedical devices^{35,38,39}, drug delivery^{40,41}, dentistry⁴², optics⁴³⁻⁴⁵, sensors⁴⁶⁻⁴⁹, and microfluidic devices⁵⁰. Self-folding can be actuated by light (including infrared radiation (IR)⁵¹⁻⁵⁵, light emitting diodes (LED)⁵⁶, microwaves⁵⁷, radio frequencies (RF)⁵⁸, and lasers⁵⁹⁻⁶²), photochemical reactions⁶³⁻⁶⁵, heat^{47,66-83}, thermal-chemical reactions^{23,66,84,85}, pneumatics^{28,86-88}, magnetism⁸⁹⁻⁹², joule heating^{34,93-98}, and biological reactions⁹⁹⁻¹⁰⁴.

Unlike hands-on techniques, hands-off methods are material-dependent. They manipulate stress/strain, chemistry, swelling, or biological responses to actuate self-folding. Despite the different stimuli, many researchers use the same geometries and folding patterns inspired by origami to self-fold complex shapes. Within hands-off folding, we will compare many different stimuli using **Table 1.1** to evaluate each technique.

Throughout this Ph.D. dissertation, we will induce self-folding using IR light, microwaves, asymmetric heat, and uniform heat. We will discuss existing self-folding techniques that use electromagnetic radiation and heat. Electromagnetic radiation is divided into IR/LED light, photo-reactive materials, lasers, RF waves, and microwaves. In studies of IR and LED light to actuate self-folding polymer sheets, researchers have patterned the surface of a polymer with a light absorbing coating, filled a polymer with particles that absorb light, and used photo-reactions to trigger self-folding^{51–53,55,105,106}.

Although radio waves⁵⁸ and microwaves⁵⁷ are studied less frequently than other parts of the electromagnetic spectrum, scientists have used them to induced self-folding. These frequencies require specific composite materials, including a filler or coating that absorbs radio waves or microwaves and converts them into heat to actuate shape change.

Heat is a common stimulus that can be employed to actuate self-folding^{47,66–83}. For example, prestrained polymers self-fold when heated asymmetrically. When heating a material, the temperature change can alter the absorption of a dye to create a macroscopic color shift for sensor applications⁴⁷, change the crystallinity in a polymer⁶⁷, or cause stitches to sew themselves up by programming a polymer to shrink under mild heat⁶⁸.

1.3.1 Light and Heat Actuation

IR/LED light can induce self-folding of prestrained PS sheets coated with inkjet printed black^{52,106,107}, grey⁵⁵, or colored⁵⁶ ink. Shining IR (for black or grey ink) or LED (for colored ink) light onto the surface of the sheet allows the ink to absorb the light and heat up. This creates an asymmetric temperature gradient through the thickness of the sheet. The surface of the sheet heats up faster and begins shrinking before the underside of the sheet, allowing the sheet to self-fold. The black, grey, and colored inks allow the system to fold simultaneously, sequentially, and individually as shown in **Figure 1.6**. With black ink, the complex shapes form through folding all the hinges simultaneously as shown in **Figure 1.6a**. By patterning various

shades of grey ink, the darkest shades will fold before the lighter shades, enabling the researchers to control the order of folding as shown in **Figure 1.6b**. Colored ink enables hinges to be folded individually (one hinge can be folded without folding any other hinges). They control heating by matching the light absorption of colored inks to the corresponding color of LED light as shown on **Figure 1.6c**.

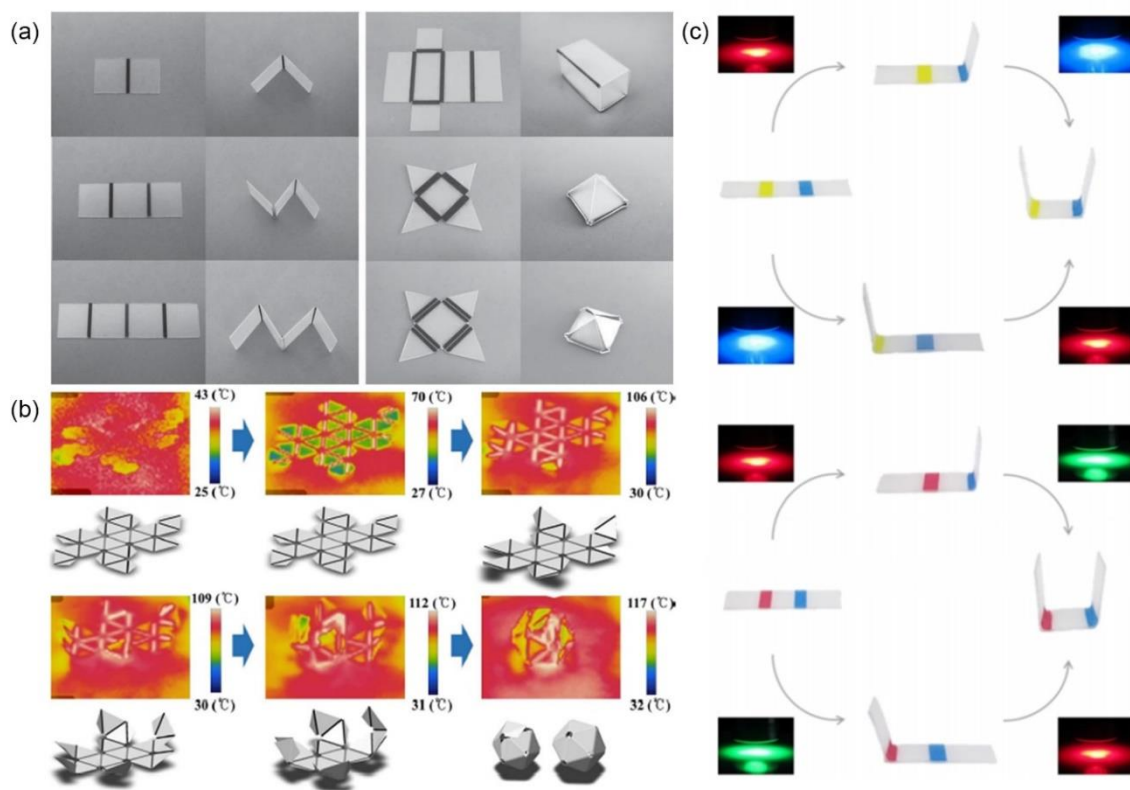


Figure 1.6. (a) Prestrained polystyrene shapes simultaneously self-fold into a variety of complex shapes using a combination of black ink and IR light⁵². (b) Prestrained polystyrene coated with grey hinges self-fold into a polyhedron in response to IR light. Changing the darkness of the hinges controls the absorption of IR light and the sequence of folds⁵⁵. (c) Prestrained polystyrene self-folds sequentially in response to LED light. By matching the LED light color to the absorption profile of the hinge color, scientists fold exclusively one hinge at a time⁵⁶.

We analyzed light actuated self-folding of prestrained PS outlined in **Table 1.1**. This technique can create both mountain and valley folds. It can fold polymer sheets sequentially by changing the hinge shading and color. It folds to a maximum dihedral angle of $\sim 180^\circ$. This process is not reversible. Researchers combined the IR-black ink and IR-grey ink systems to generate gradients of black and grey in the hinges to generate curves⁵⁴.

In addition to absorbing light to generate heat, some polymers undergo photo-induced stress relaxation or photo-induced cross-linking which causes self-folding^{51,63–65,105,108–111}. Researchers combine 22–25 pentaerythritol tetra(3-mercaptopropionate) (PETMP), 2-methylene-propane-1,3-di(thioethylvinylether) (MDTVE), and ethylene glycol di(3-mercaptopropionate) (EGDMP) mixed in a 1:4:5 wt.% ratio with two photoinitiators (1 wt.% each of Iragacure 819 and 184) to make a copolymer⁶⁵. This mixture polymerizes in response to irradiation with light at 400–500 nm, 40 mW cm². Researchers programmed the copolymer by irradiating light at 365 nm to cleave the MDTVE functionalities in the polymer backbone. When the bonds break, a small number of free radicals form and react with each other. Reconnecting the polymer in this way creates irreversible changes to the polymer network. If a strained sample is irradiated with a photomask, only the 'hinge' region rearranges and locally increases the modulus. When the strain is released, the sample folds as the stress in the non-irradiated regions recover as shown in **Figure 1.7**. This technique can make 3D objects by using a complex photomask and biaxially straining the copolymer.

We compared photo-induce strain relaxation self-folding of a strained copolymer to other techniques in **Table 1.1**. This technique can generate only valley folds as implemented in the paper⁶⁵. It cannot fold sequentially or reversibly. It has a maximum dihedral angle of $\sim 120^\circ$. Researchers can control the curvature in the hinge through controlling the concentration of the photo-reactive species in the copolymer.

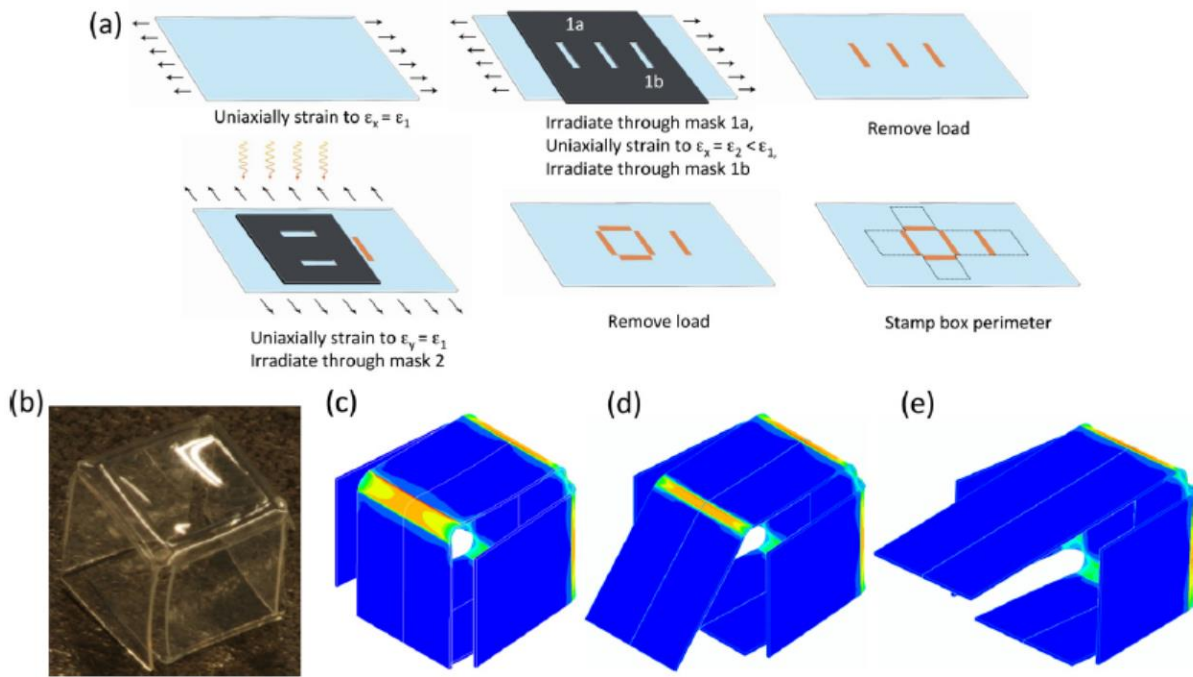


Figure 1.7. The fabrication method to make a photo-induced self-folding box. (a) A photomask used to pattern the hinges for a box. (b) Experimentally folded box. (c-e) Simulation results that predict a closed box and an open box⁶⁵.

Compared to their IR and LED counterparts, lasers provide a unique and efficient way to heat samples to trigger self-folding^{59–62,112}. Researchers completely coat a prestrained PS sheet with black ink and shine a continuous-wave 1064 nm Nd:YAG laser at the inked surface. Wherever the laser hits the surface, the ink absorbs the laser light and heats up. If the laser shines in a raster pattern across the surface of the sheet, it generates a self-folding response. **Figure 1.8** shows laser light actuating self-folding in a prestrained PS sheet⁶¹. In the IR and LED light actuation system, light shines across the entire sheet but only the inked hinge absorbs the energy. In the laser actuation system, the ink covers the entire sheet but only the region hit by the laser heats up. Therefore, the hinges rely on the location and shape of the laser, not the pattern of the ink.

We studied laser light induced self-folding of a prestrained PS sheet in **Table 1.1**. This technique can make only valley folds as implemented in the paper. It can fold sequentially by

moving the laser to a new location after folding the sheet. It has a maximum dihedral angle of $\sim 90^\circ$. After $\sim 90^\circ$, the sheet blocks the incoming laser light, preventing further folding. This technique is not reversible (it cannot fold and unfold multiple times). We speculate that changing the raster pattern of the laser could enable future researchers to control the curvature in the sheet.

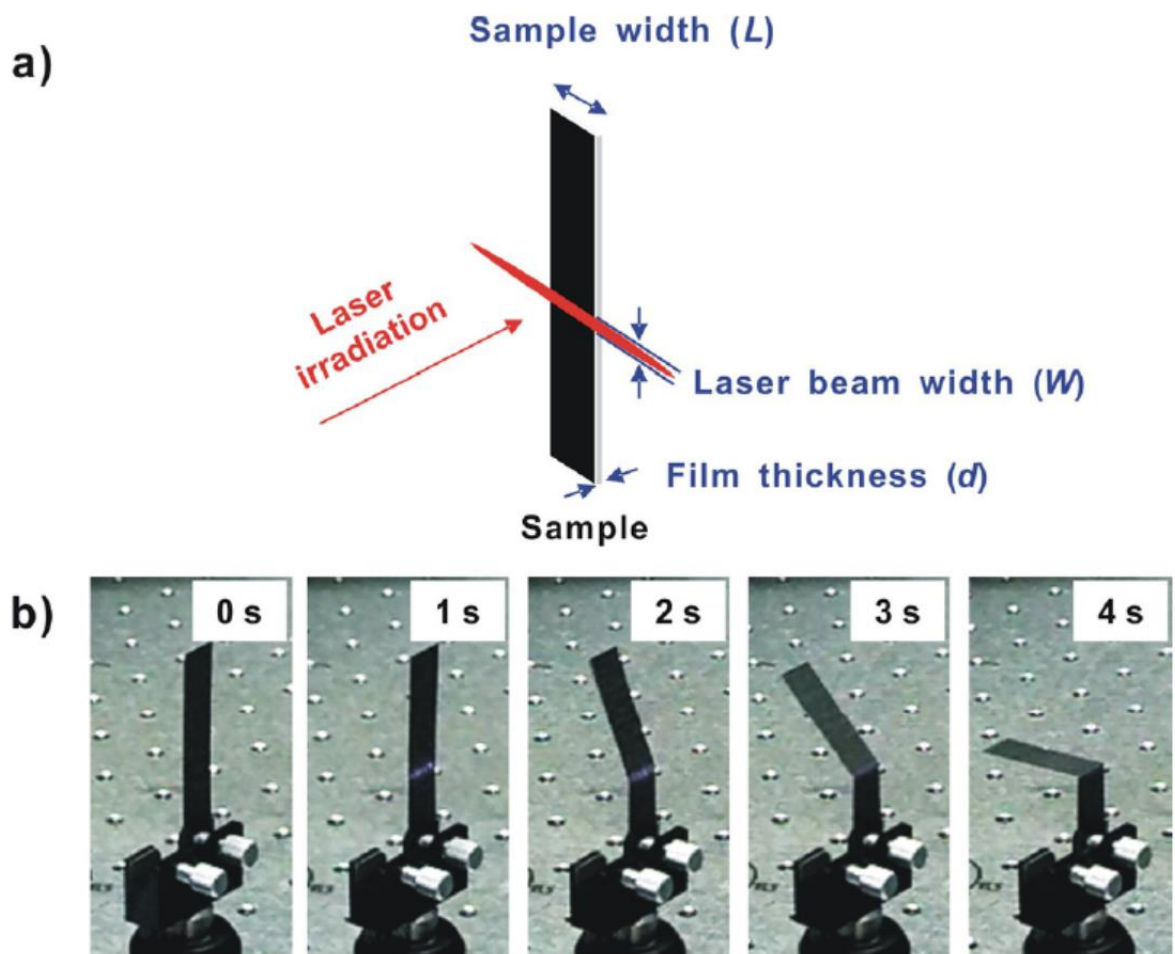


Figure 1.8. (a) Prestrained polystyrene sheet self-folds in response to a laser radiating across its surface, creating a hinge. (b) Once the laser hits the surface, the sample folds to 90° in 4 seconds⁶¹.

Shape change using radiofrequencies (RF) is possible using a polymer composite filled with Fe_3O_4 nanoparticles and carbon nanotubes (CNTs) – which absorb two different RF ranges, 296 kHz and 13.56 MHz, respectively⁵⁸. This technique is different from the other method presented in this review because it is an unfolding technique instead of a self-folding technique. The composite is synthesized with an epoxy-based polymer matrix filled with both nanofillers. By controlling the location of each nanofiller within the polymer host, one can designate specific sections of the film that heat when exposed different frequencies of RF waves. In **Figure 1.9**, researchers make a polymer film with a Fe_3O_4 rich region, a nanoparticle-free region, and a CNT rich region. Then, they deform the polymer to manually make Temporary Shape 1 (TS1). From TS1, researchers can actuate the Fe_3O_4 rich or CNT rich region with the matching RF wave to change shape into TS2 or TS3. If both are activated (regardless of order), the polymer folds into TS4. If the whole composite is activated, the sheet will return to the original flat sheet shown in the center of **Figure 1.9**.

We investigated RF wave induced unfolding of a polymer composite sheet in **Table 1.1**. This technique can unfold mountain and valley folds. It can unfold sequentially by changing the RF frequency. It can unfold a sheet from any angle back to 0° . The sheet can recover multiple times, but the sheet is not folding, thus the technique is repeatable but not reversible. This technique cannot induce curvature into the sheet.

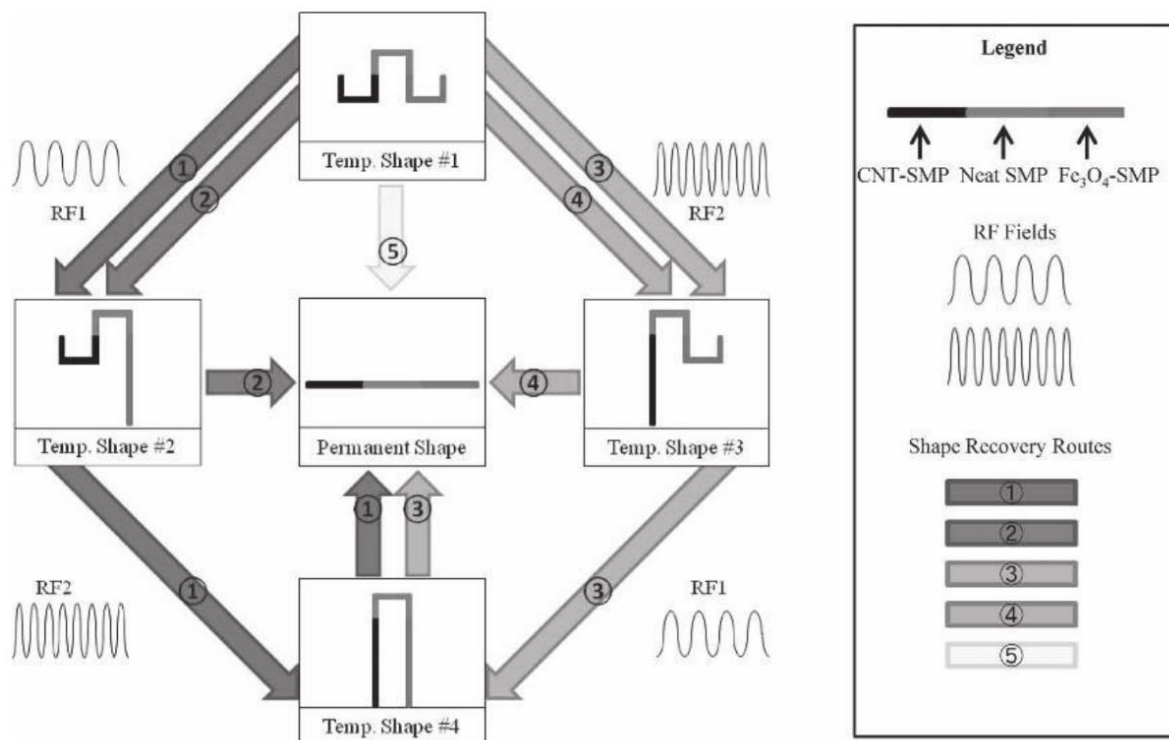


Figure 1.9. The schematic shows the possible unfolding pathways for a polymer composite filled with Fe₃O₄ and CNT nanoparticles. The polymer is divided into 3 regions; CNT-rich, polymer only, and Fe₃O₄-rich. The polymer is manually deformed into TS1 and unfolded using different frequencies of RF waves. If uniform heat is applied, the sample recovers to form the original flat sheet in the center⁵⁸. There are five recovery routes based on the order in which stimuli are applied.

Prestrained PS can be folded using microwaves. Researchers coat the surface of the sheet with an ink containing graphene and iron oxide. When placed in a microwave, the ink absorbs the microwaves and converts them into heat. The heat creates an asymmetric temperature gradient through the thickness of the film, shrinking the surface faster than the backside, thus inducing self-folding. The process discussed here is sensitive to the orientation of the sample with respect to the source of the microwaves. When the azimuthal angle changes, the absorption process changes, causing samples to crater or fold in a different direction compared to when the hinge is perpendicular to the microwave source as shown in **Figure 1.10**⁵⁷.

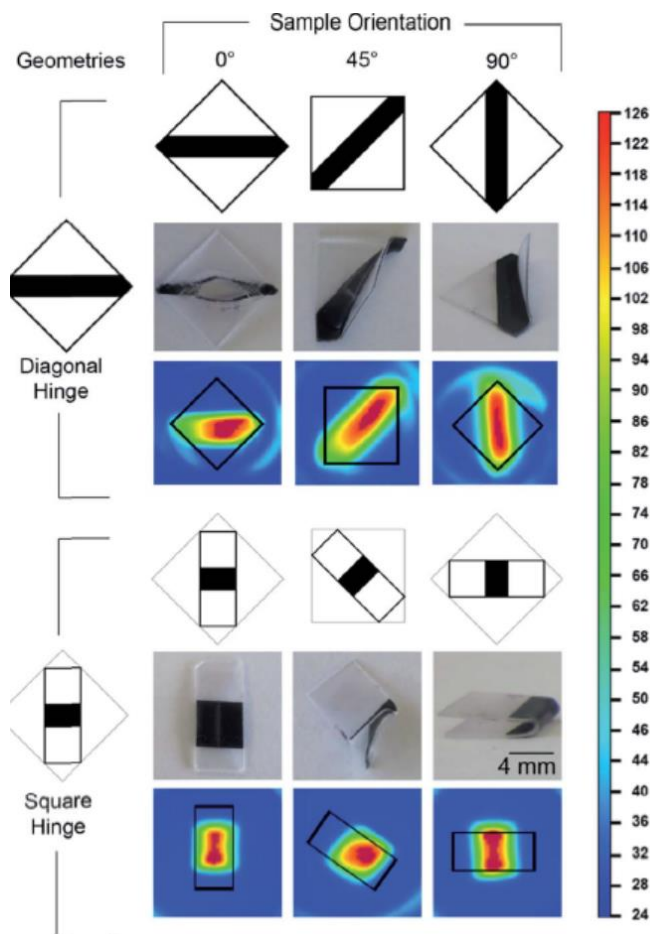


Figure 1.10. Polystyrene coated with graphene ink folds in response to microwaves⁵⁷. The pattern, the experimental sample, and the thermal image taken with an infrared camera are shown for two different geometries at azimuthal angles of 0°, 45°, and 90°. The azimuthal angle determines the type of folding and the heating profile.

We analyzed this microwave induced self-folding technique using the properties outlined in **Table 1.1**. Microwave induced shrink film folding can only make valley folds. If the technique were improved, we speculate that both mountain and valley folds would be possible. This technique cannot fold reversibly or sequentially. The maximum possible dihedral angle is $\sim 180^\circ$. The researchers did not explore if they can control curvature in the hinges or panels.

Figure 1.11 shows the fabrication of a foldable cube on the scale of hundreds of nanometers. Researchers used an electron beam (e-beam) process to create an origami inspired pattern from a poly(methyl methacrylate) (PMMA) thin film coated on a silicon

substrate. E-beam lithography shoots a beam of electrons onto a substrate to ablate away the surface and create grooves. These grooves are filled with a mixture of Au and Al_2O_3 to keep the panels stiff and improve electrical properties. Many panels are adhered together using Sn hinges as shown on **Figure 1.11e**. The researchers use plasma etching to remove the composite from the underlying silicon. Plasma etching creates enough heat to melt the Sn hinges. The Sn hinges reflow and pull any attached panels, inducing a self-folding response (cf. **Figure 1.11f-g**). When panels touch, the hinges seal together and the new shape becomes rigid. The folding angle depends on the amount of Sn in the hinge and the parameters of the plasma etching. The embedded metals enhance the conductivity and electric properties of the folding structure which can be programmed based on the composition of the metals used.

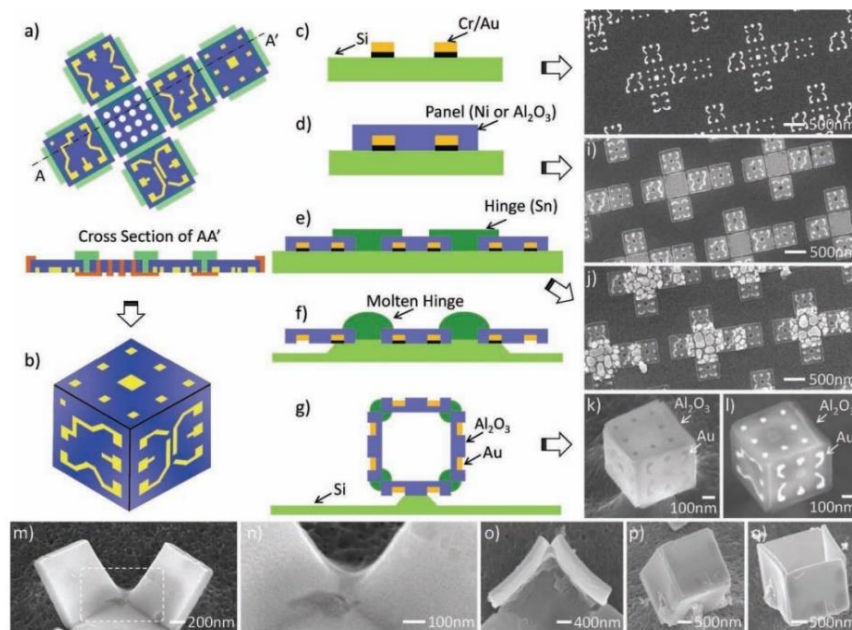


Figure 1.11. Schematic of fabrication and experimental results for a polymer-metal composite self-folding system. (a,b) Self-folding sheet with multilayer patterned panels shown in pre-and post-folding positions. (c-g) Step-by-step fabrication of polymer-metal composite. (h-l) SEM images of a self-folded cube before and after folding. (m-q) SEM images of the Sn hinges fusing together to reinforce the structure after folding⁸⁰.

We studied this metal-hinge melting self-folding technique using the properties outlined in **Table 1.1**. This technique can make valley folds, but not mountain folds. It can fold sequentially by controlling which hinges are heated first. The researchers did not explore if the process is reversible, what is the maximum possible folding angle, or if they can control curvature in the hinges or panels.

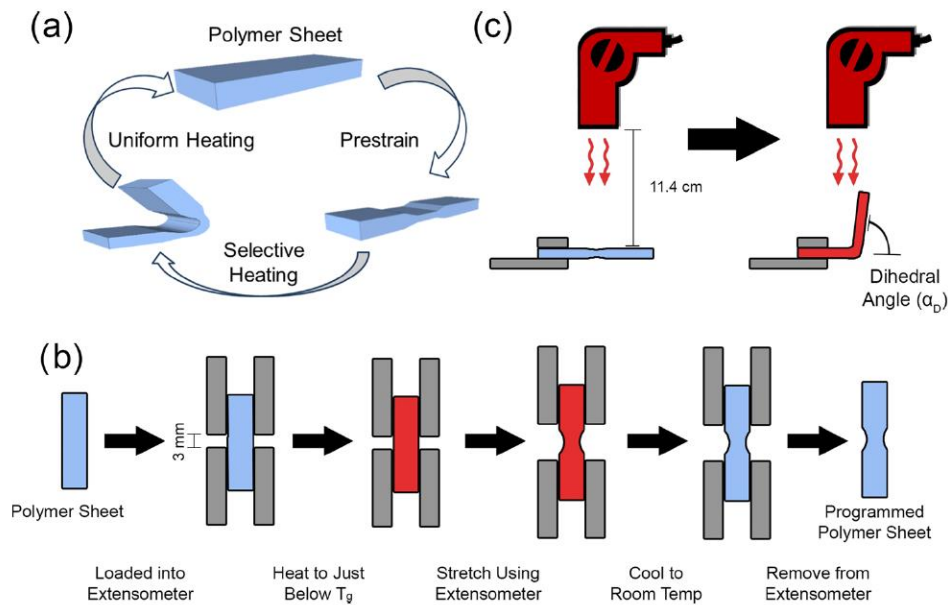


Figure 1.12. (a) The thermoplastic is locally deformed to create a hinge, then self-folded, then recovered in uniform heat. This cycle can be repeated. (b) A heat gun warms the surface of the polymer until the sheet folds. (c) Schematic for programming a thermoplastic polymer to fold in response to a gradient of heat⁸³.

Figure 1.12 shows another method to induce self-folding in thermoplastic polymers using heat. Researchers locally deform a homogenous polymer sheet to create a hinge that self-folds in response to asymmetric heat. A heat gun is used to heat the exposed top surface of the hinge faster than the backside, allowing the surface to shrink faster than the backside of the hinge, thus inducing self-folding. Thermoplastic sheets up to 12 mm thick are self-folded using this technique.

We compared this thick sheet self-folding method to other techniques using the properties outlined in **Table 1.1**. This technique can generate valley folds, but not mountain folds. It can fold sequentially by controlling which hinges are heated first. This technique is not reversible although the material can be recovered and strained again as shown in **Figure 1.12a**. After folding, the original shape can be recovered in uniform heat and the process can begin again. The maximum possible dihedral angle is $\sim 180^\circ$ if the heat gun is moved as the sample folds. If the heat gun is held stationary, the maximum dihedral angle is $\sim 90^\circ$. The researchers did not explore if they can control curvature in the hinges or panels.

1.3.2 Other Actuation methods

This PhD. dissertation studies self-folding actuated by light and heat, but many other techniques exist, including thermal-chemical, pneumatics, magnetism, electricity, and biological responses. We will briefly explore each of these topics as a survey of other stimuli. Including these techniques in the review will give a more complete analysis of the tools available to researchers for to creating new self-folding systems. We will evaluate them using **Table 1.1**.

The chemistry of polymers can be manipulated to allow materials to have multiple transition states and fold reversibly^{23,66,84,85}. Isothermal crystallization can be employed to create multiple stable states in a semi-crystalline polymer⁷⁰. Specific temperature transitions trigger the change between these states. The crystallinity controls the transition temperatures, and chemical adjustments of crystallinity allow for transition temperature programming.

Chemistry can also control the T_g . Researchers prepared a copolymer composed of poly(2,5-furandimethylene succinate) (PFS) and bismaleimide.^{25,26} (M). The local T_g in the film can be controlled by submerging a section of the film into 1,8-bis-maleimidotriethyleneglycol (M_2) solution with different concentrations as shown in **Figure 1.13a**. At 40 °C, they program the folded shape to be a pyramid and at 60 °C they program

the shape to be an open star. By changing the temperature from room temperature to 65 °C, they actuate each hinge as the temperature of that hinge exceeds its local T_g as shown in **Figure 1.13b-c**.

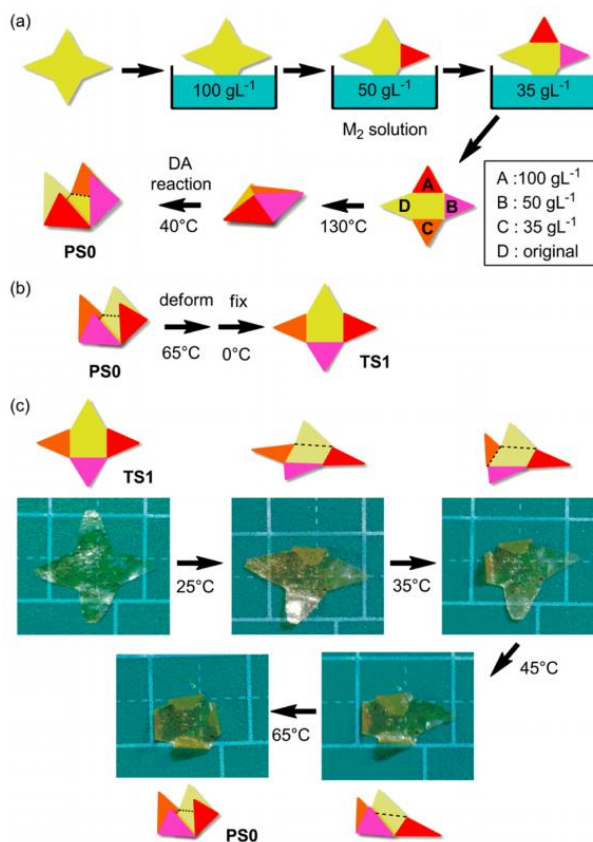


Figure 1.13. (a) The T_g of the hinges are controlled locally by reacting the PFS/M co-polymer with different concentrations of M_2 reagent. (b) The substrate is thermally programmed at various temperatures to choose which shapes it will take when folded. (c) The sheet is heated from 25 to 65 °C, actuating each hinges individually⁸⁵.

We analyzed this local T_g based self-folding technique using the properties outlined in **Table 1.1**. This technique can generate both mountain and valley folds. It can fold sequentially by controlling the T_g in each hinge. This technique is reversible by increasing and decreasing the temperature. The maximum possible dihedral angle is $\sim 180^\circ$. Although not explored in the

paper, we speculate that curvature is possible with this system because they can control the T_g locally.

Researchers created a bilayer laminate composed of a patterned polymer (SU8) substrate bound to a prestrained elastomer with an adhesive (AZ 5214) shown systematically in **Figure 1.14a**. The edges of the SU8 sheet are bound directly to the elastomer substrate. When acetone dissolves the AZ 5214, the prestrained elastomer relaxes and causes the SU8 layer to fold. The folding is controlled by thinning the SU8 sheet wherever a hinge is desired. By manipulating geometry and hinge locations, complex shapes were created as shown in **Figure 1.14b-d**.

We studied this chemically induced self-folding technique using the properties outlined in **Table 1.1**. This technique can generate both mountain and valley folds. If the elastomer is stretched, the SU8 layer will unfold. The maximum possible dihedral angle is $\sim 180^\circ$. This system cannot fold sequentially. By controlling the geometry and hinge thickness, researchers made curves as shown in **Figure 1.14d**.

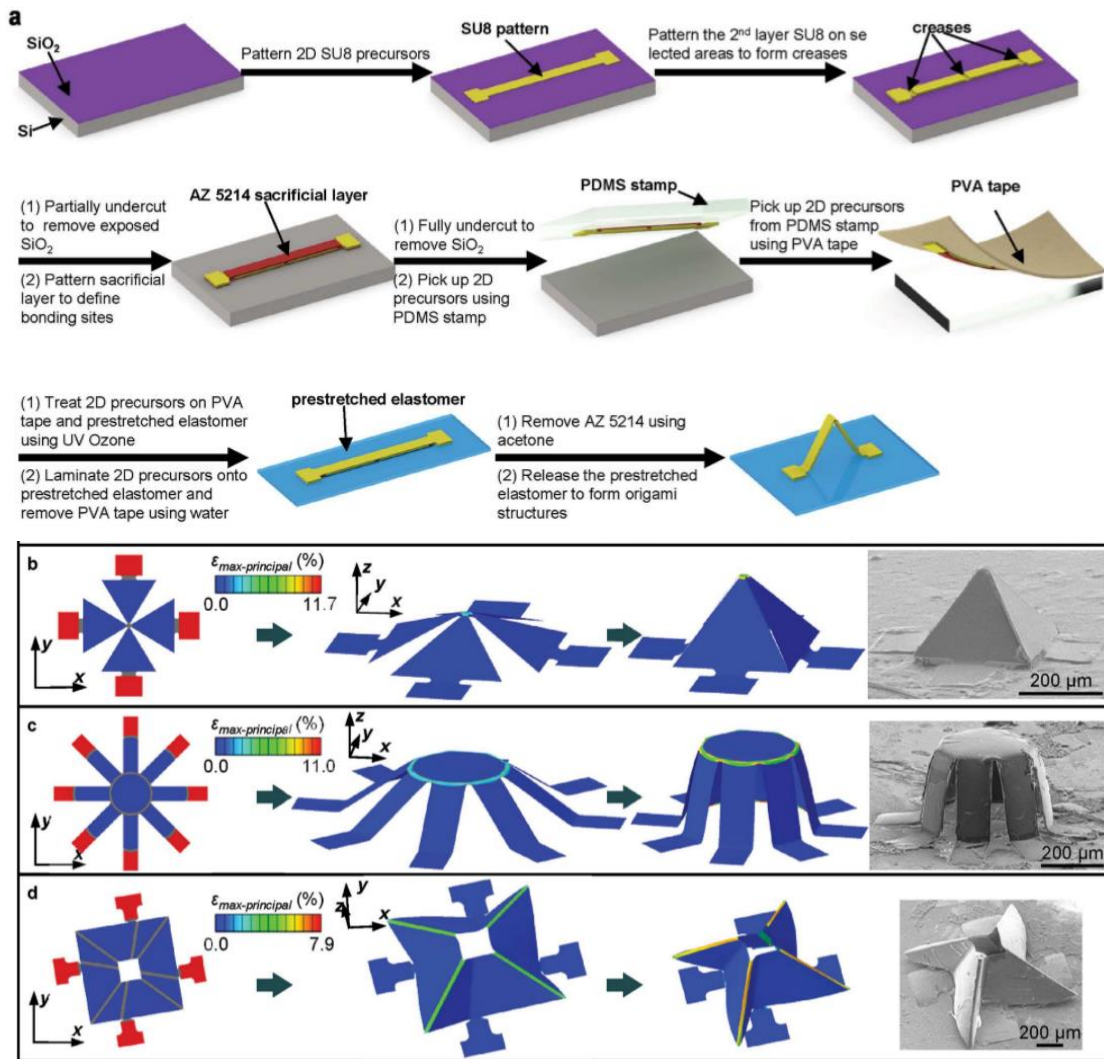


Figure 1.14. (a) Schematic depicting a method used to fabricate the SU8/elastomer bilayer. (b-d) Finite element analysis predicted folding a pyramid, cylindrical shell, and ‘windmill’ (left). These shapes were fabricated (right)¹¹³.

Origami inspired pneumatic controlled actuation is largely used in soft robotics^{28,86–88} and sensors^{114,115}. Pneumatics are primarily used with elastomers due to the need for flexibility and elasticity to actuate folding. Researchers fabricated the gripper legs shown in **Figure 1.15a-b** from a polymer composite of poly(dimethylsiloxane) (PDMS) and Ecoflex 00-30. Pressurized air inflates the Ecoflex layer and induces self-folding. This type of motion control is well suited to soft grippers. Researchers created a pneumatically triggered hand for remote

actuation as shown in **Figure 1.15c**. The hand is made from PDMS balloons that inflate and deflate to control the fingers. The researchers created an external glove that controls the hand precisely. Whenever the glove moves, the balloons adjust in size to move the hand the same amount. Remote medical surgery is a possible future application for this technology¹¹⁵.

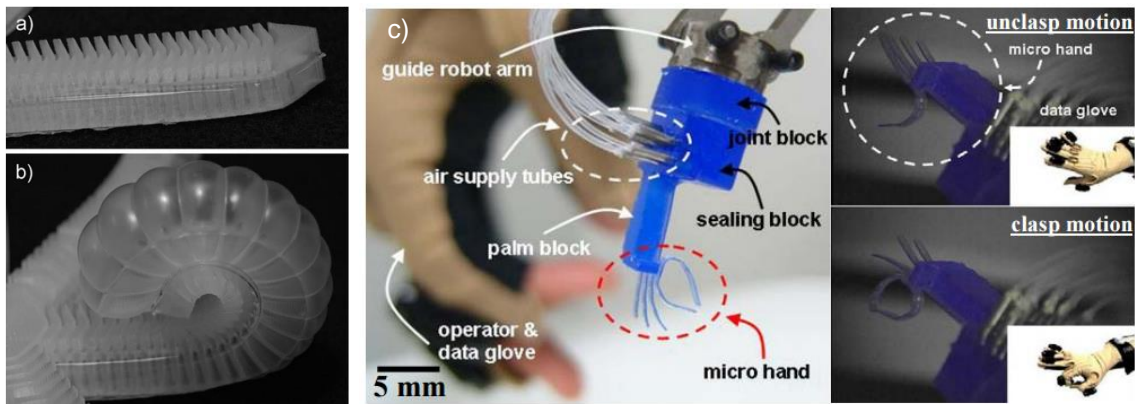


Figure 1.15. Pneumatically actuated tentacles⁸⁶ (a-b) and hands¹¹⁵ (c). Both devices flex from inserting pressurized air into the hollow center of the device. The hands can also synchronize with an external glove to precisely control actuation with finger movements.

Due to their similarities, these two self-folding techniques were combined when analyzed in **Table 1.1**. Both pneumatic systems can make mountain and valley folds. They are fully reversible and can fold sequentially. Through controlling patterns in the sheets, researchers control the curvature in the hinge. The only thing these systems do not show is the ability to generate folds with a small radius of curvature (sharp folds).

Magnetically actuated polymer are usually composites of a soft polymer and a magnetically active metal component⁸⁹⁻⁹². Researchers patterned magnetic dipoles onto PDMS sheets to enable magnetically actuated folding as shown in **Figure 1.16**. They cut a 3D object into flat connected pieces like unpeeling an orange or a map projection of planet

Earth. By patterning the edges and applying a magnetic field, researchers make the ‘nearly’ flat sheet fold into a sphere as shown in **Figure 1.16a-b**. Applying this same technique to other patterns, they made a variety of other shapes as shown in **Figure 1.16c-h**.

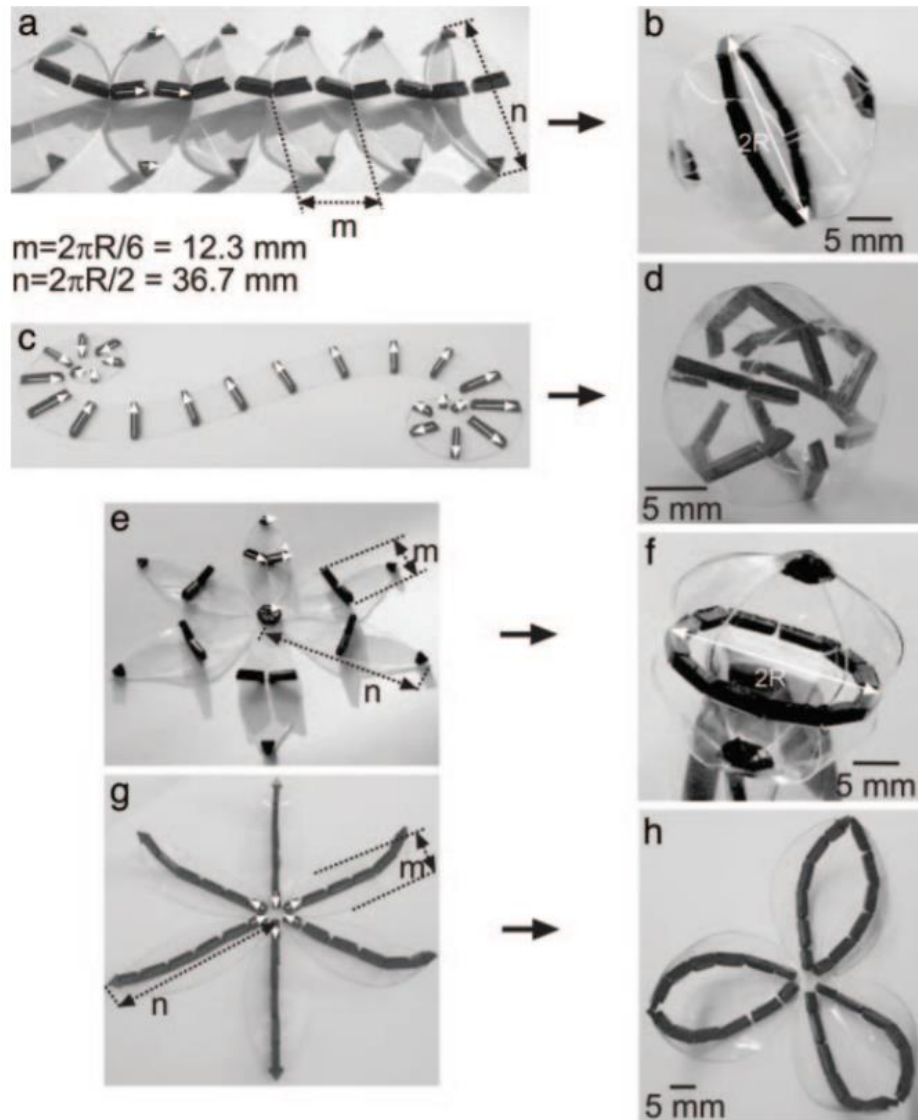


Figure 1.16. PDMS sheets patterned with magnetic dipoles self-folded into 3-D structures when placed into a magnetic field⁹⁰.

We analyzed this magnetically actuated self-folding technique using the properties outlined in **Table 1.1**. This technique can only generate valley folds due to the limitations of the magnetic field. The interactions between magnetic dipoles stabilize the 3D structures. If the interactions are disrupted, the sample will unfold, therefore the process is reversible. Due to the complexity of the hinges, we could not determine a maximum dihedral angle, but we speculate based on the images that the dihedral angles are $<90^\circ$. This system cannot fold sequentially because the magnetic field interacts with all hinges simultaneously. This system can control curvature accurately.

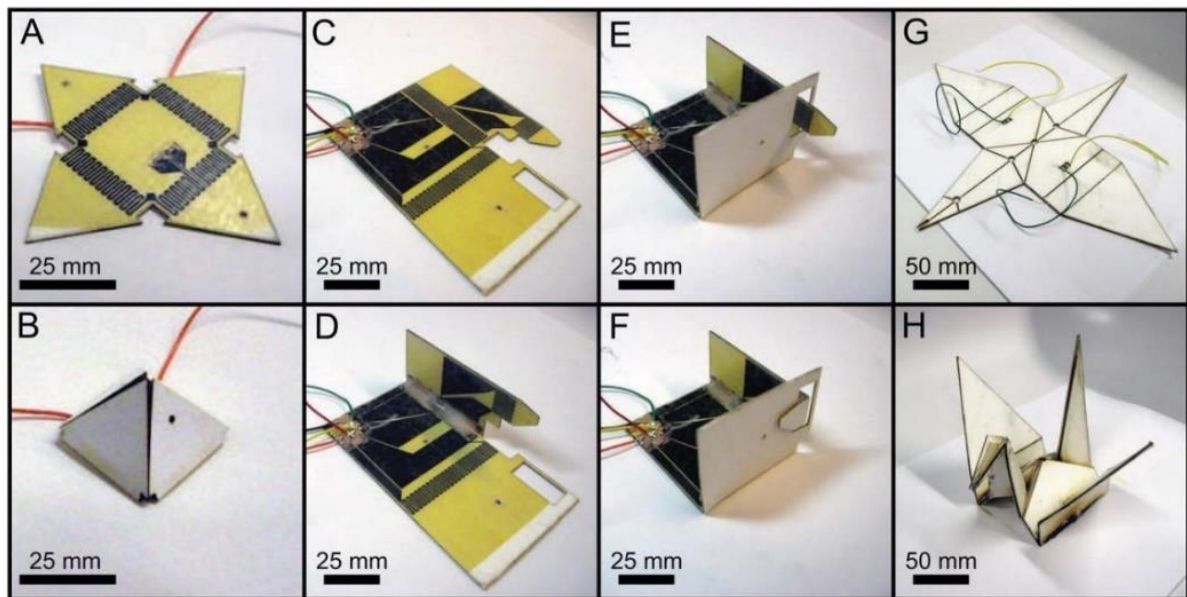


Figure 1.17. A composite of paper, prestrained PO, prestrained PS, and a copper circuit etched into polyimide self-folds into various 3D shapes via joule heating. A pyramid (A-B), a box with a tab lock (C-F) and a crane (G-H) were all fabricated with this method through a combination of sequential and simultaneous folding⁹⁴.

Researchers have studied using electricity to actuate self-folding through dielectric/piezoelectric properties^{116–119} or joule/resistive heating^{34,93–98}. In **Figure 1.17**, researchers used a composite of uniaxially prestrained polyolefin (PO), biaxially prestrained

PS, paper, and a copper circuit etched into polyimide to self-fold 3D shapes via joule heating. The copper circuit etched into polyimide provides heat when electricity flows through the layer. When exposed to heat, the PO and PS layers shrink asymmetrically in the hinge region, causing the hinge to self-fold.

We compared this joule heating self-folding method to other techniques using the properties outlined in **Table 1.1**. This technique can generate both mountain and valley folds by changing the order of layers in the composite. The hinges can be actuated individually, so sequential folding is possible. The maximum possible dihedral angle is $\sim 180^\circ$. The samples cannot fold reversibly because the prestrained layers cannot become prestrained again without additional processing steps. In its current form, this technique cannot make curves, although we speculate that curvature would be possible if researchers improved this technique.

Self-folding mechanisms exist in nature. Scientists studied shape changing via molecular switches⁹⁹, Venus flytraps^{100,101}, and other bioinspired actuation methods^{102–104}. The Venus flytrap closing mechanism is one of the fastest actuations in nature because it self-folds completely in ~ 0.04 seconds. Scientists do not fully understand the mechanism, but some researchers have modeled this system and argue that leaf geometry determines the macroscopic closing mechanism as shown in **Figure 1.18**. Because Venus flytrap leaves curve in two orthogonal directions, if a leaf bends in one area, it will stretch in another. The coupling between bending and stretching is strong that if the center bends slightly, the leaf snaps shut to avoid deforming further. The snapping action is captured on **Figure 1.18e-d**.

Self-folding observed in the Venus flytrap was compared to other self-folding methods in **Table 1.1**. This plant can only make valley folds because it only actuates between open and closed states. This folding is reversible and folds to a maximum dihedral angle of $\sim 180^\circ$. The leaves always fold together, so sequential folding is impossible. This technique can make curved hinges, but the method to control the curvature is not currently understood.

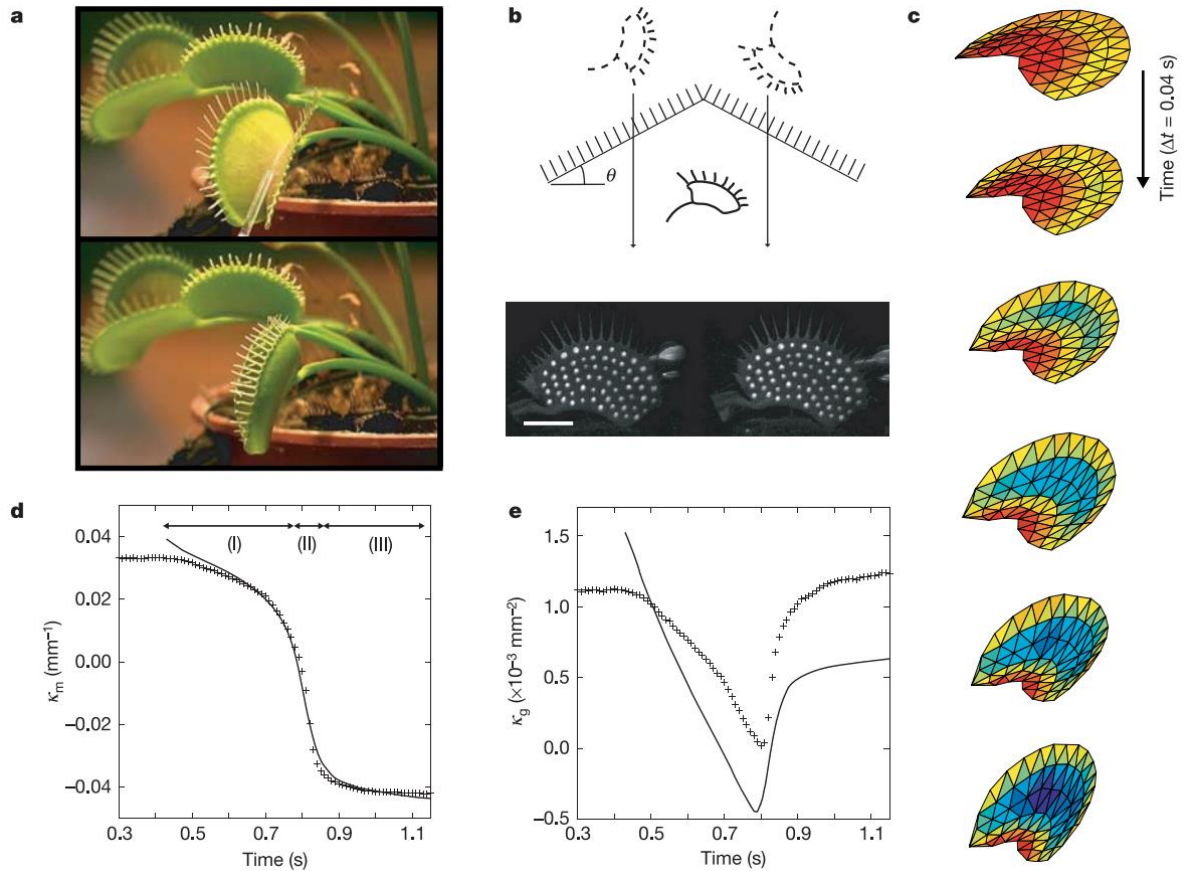


Figure 1.18. The Venus flytrap uses a snap-through mechanism to fold 180° in less than one second¹⁰⁰. (a) The Venus flytrap before and after actuation. (b) Stereo imaging showing fluorescent dots on the leaf surface. (c) Mesh pattern of the leaf closing using color to show local curvature (blue is more curved than red). The spatially averaged mean curvature (d) and the Gaussian curvature (e) showing the snapping reaction as a function of time.

1.4 Summary

Origami has inspired numerous advances in science. It provides the patterns and mathematics that enable the creation of 3D objects from 2D sheets. Hands-on and hands-off techniques both continue to improve and innovate technology. Currently, the ability to control hinges, fold order, object size, and materials allows hands-on folding to create more complex objects. Despite limited material choices and fabrication thicknesses, hands-off folding is more useful in remote deployment and on the microscopic scale. For the hands-off techniques we outlined, some methods are better at creating complex shapes, some mechanisms fold faster

or in a more controlled manner, some approaches create curves instead of folds, and some designs fold sequentially or reversibly. Because no hands-off techniques are particularly effective on the macroscopic scale, this PhD. dissertation focuses on using hands-off techniques to self-fold polymer sheets to create complex macroscopic objects.

From surveying hands-off techniques, we decided to focus on various types of light and heat. We believe these stimuli allow for greater control and more robust systems. We use hands-on techniques for inspiration for how to fold useful macroscopic origami-inspired objects and chose to focus on PS and PMMA.

Polymers can be actuated in a variety of ways. We can use hand-on or hands-off techniques depending on the application. We can implement these techniques and macro and micro scales and with many different polymers. As researchers continue to innovate techniques and polymers, our toolbox will grow.

Future developments of hands-off techniques could transform the way society uses origami in everyday life. We might have self-folding tables in our houses and circuits that can reconfigure themselves to suit the needs of the end-user. We could make entire space stations change shape to alter its exposure to the sun. If we continue to invest in this technology, the potential is unlimited!

References

1. Liu, Y., Genzer, J. & Dickey, M. D. '2D or not 2D': Shape-programming polymer sheets. *Prog. Polym. Sci.* **52**, 79–106 (2016).
2. Choi, J., Kwon, O.-C., Jo, W., Lee, H. J. & Moon, M.-W. 4D Printing Technology: A Review. *3D Print. Addit. Manuf.* **2**, 159–167 (2015).
3. Bae, W.-G., Kim, H. N., Kim, D., Park, S.-H., Jeong, H. E. and Suh, K.-Y. 25th Anniversary Article: Scalable Multiscale Patterned Structures Inspired by Nature: the Role of Hierarchy. *Adv. Mater.* **26**, 675–700 (2014).
4. Fan, X., Chung, J. Y., Lim, Y. X., Li, Z. & Loh, X. J. A Review of Adaptive Programmable Materials and Their Bio-applications. *ACS Appl. Mater. Interfaces* **8**, 33351–33370 (2016).
5. Meng, H. & Li, G. A review of stimuli-responsive shape memory polymer composites. *Polymer* **54**, 2199–2221 (2013).
6. O'Halloran, A., O'Malley, F. & McHugh, P. A review on dielectric elastomer actuators, technology, applications, and challenges. *J. Appl. Phys.* **104**, 071101-071101-10 (2008).
7. Bindu Sri. M, A. V. As A Review on Hydrogels as Drug Delivery in the Pharmaceutical Field. *Int. J. Pharm. Chem. Sci.* **1**, 642–661 (2012).
8. Deligkaris, K., Tadele, T. S., Olthuis, W. & van den Berg, A. Hydrogel-based devices for biomedical applications. *Sens. Actuators B Chem.* **147**, 765–774 (2010).
9. Laftah, W. A., Hashim, S. & Ibrahim, A. N. Polymer Hydrogels: A Review. *Polym.-Plast. Technol. Eng.* **50**, 1475–1486 (2011).
10. Peraza-Hernandez, E. A., Hartl, D. J., Jr, R. J. M. & Lagoudas, D. C. Origami-inspired active structures: a synthesis and review. *Smart Mater. Struct.* **23**, 094001 (2014).
11. Rousseau, I. A. Challenges of shape memory polymers: A review of the progress toward overcoming SMP's limitations. *Polym. Eng. Sci.* **48**, 2075–2089 (2008).
12. Fu, Y. Q., Du, H. J., Huang, W. M., Zhang, S. & Hu, M. TiNi-based thin films in MEMS applications: a review. *Sens. Actuators -Phys.* **112**, 395–408 (2004).
13. Zirbel, Shannon A., Brian P. Trease, Mark W. Thomson, Robert J. Lang, Spencer P. Magleby, and Larry H. Howell. "HanaFlex: A Large Solar Array for Space Applications." *Micro- and Nanotechnology Sensors, Systems, and Applications VII* 94671 (2015).

14. Morgan, M. R., Lang, R. J., Magleby, S. P. & Howell, L. L. Towards developing product applications of thick origami using the offset panel technique. *Mech. Sci.* **7**, 69–77 (2016).
15. Zachary A., Cantarella J., Demaine E., Eppstein D., Hull T., Ku J., Lang R., Tachi T. Rigid Origami Vertices: Conditions and Forcing Sets. *JoCG.* **7** 171-184 (2016).
16. Zirbel, S. A. *et al.* Accommodating Thickness in Origami-Based Deployable Arrays. *J. Mech. Des.* **135**, 111005 (2013).
17. Tomohiro Tachi. in *Origami* **5** 253–263 (A K Peters/CRC Press, 2011).
18. Chen, Y., Peng, R. & You, Z. Origami of thick panels. *Science* **349**, 396–400 (2015).
19. Morphees: Shape-shifting mobile devices (w/ Video). at <<http://phys.org/news/2013-04-morphees-shape-shifting-mobile-devices-video.html>>
20. Hayes, G. J., Liu, Y., Genzer, J., Lazzi, G. & Dickey, M. D. Self-Folding Origami Microstrip Antennas. *IEEE Trans. Antennas Propag.* **62**, 5416–5419 (2014).
21. Hubschman, J.-P. *et al.* ‘The Microhand’: a new concept of micro-forceps for ocular robotic surgery. *Eye* **24**, 364–367 (2010).
22. Lu, Y.-W. & Kim, C.-J. Microhand for biological applications. *Appl. Phys. Lett.* **89**, 164101/1-3 (2006).
23. Malachowski, K. *et al.* Stimuli-Responsive Theragrippers for Chemomechanical Controlled Release. *Angew. Chem. Int. Ed.* **53**, 1–6 (2014).
24. Wood, R. J., Avadhanula, S., Sahai, R., Steltz, E. & Fearing, R. S. Microrobot Design Using Fiber Reinforced Composites. *J. Mech. Des.* **130**, 052304–052304 (2008).
25. An, B. *et al.* An end-to-end approach to making self-folded 3D surface shapes by uniform heating. in 1466–1473 (IEEE Conf. Robotics & Automation, 2014).
26. Felton, S. M., Tolley, M. T. & Wood, R. J. Mechanically programmed self-folding at the millimeter scale. in 1232–1237 (IEEE, 2014).
27. Felton, S., Tolley, M., Demaine, E., Rus, D. & Wood, R. A method for building self-folding machines. *Science* **345**, 644–646 (2014).
28. Sun, X., Felton, S. M., Niiyama, R., Wood, R. J. & Kim, S. Self-folding and self-actuating robots: A pneumatic approach. in 3160–3165 (IEEE, 2015).

29. Wehner, M, Tolley M., Mengüç Y., Park Y., Mozeika A., Ding Y., Onal C., Shepherd R., Whitesides G, and Wood R. Pneumatic Energy Sources for Autonomous and Wearable Soft Robotics. *Soft Robotics* **1** 263-74 (2014).
30. Chien, C.-W. *et al.* Flat-Plate Photovoltaics with Solar-Tracking Origami Micro-Concentrator Arrays. in JW2A.103 (Optical Society of America, 2015).
31. Guo, X. *et al.* Two- and three-dimensional folding of thin film single-crystalline silicon for photovoltaic power applications. *Proc. Natl. Acad. Sci.* **106**, 20149–20154 (2009).
32. Song, Z. *et al.* Origami lithium-ion batteries. *Nat. Commun.* **5**, 3140/1-6 (2014).
33. Pentlicki, C. J. Self-deployable solar cell panel. US4133501 A (1979).
34. Tu, H., Jiang, H., Yu, H. & Xu, Y. Hybrid silicon-polymer platform for self-locking and self-deploying origami. *Appl. Phys. Lett.* **103**, 241902/1-4 (2013).
35. Kuribayashi, K. *et al.* Self-deployable origami stent grafts as a biomedical application of Ni-rich TiNi shape memory alloy foil. *Mater Sci Eng -Struct Mater Prop Microstruct Process* **419**, 131–137 (2006).
36. Lee, N. & Pellegrino, S. Packaging and deployment strategies for synthetic aperture radar membrane antenna arrays. in 1–4 (IEEE, 2014).
37. Kimionis, J. & Tentzeris, M. Origami antennas and packaging using 3D printing technologies. *SPIE Newsroom* (2015).
38. Maitland, D. J., Metzger, M. F., Schumann, D., Lee, A. & Wilson, T. S. Photothermal properties of shape memory polymer micro-actuators for treating stroke. *Lasers Surg Med* **30**, 1–11 (2002).
39. Meier, T. *et al.* Programmable and self-demolding microstructured molds fabricated from shape-memory polymers. *J. Micromechanics Microengineering* **25**, 065017 (2015).
40. Fernandes, R. & Gracias, D. H. Self-folding polymeric containers for encapsulation and delivery of drugs. *Adv. Drug Deliv. Rev.* **64**, 1579–1589 (2012).
41. Fusco, S. *et al.* An Integrated Microrobotic Platform for On-Demand, Targeted Therapeutic Interventions. *Adv. Mater.* **26**, 952–957 (2013).
42. Y, Seo. Shape memory dental retention systems. US 8651864 B2 (2014).
43. Chandra, D., Yang, S. & Lin, P.-C. Strain responsive concave and convex microlens arrays. *Appl. Phys. Lett.* **91**, 251912 (2007).

44. Kolaric, B., Vandeparre, H., Desprez, S., Vallée, R. A. L. & Damman, P. In situ tuning the optical properties of a cavity by wrinkling. *Appl. Phys. Lett.* **96**, 043119 (2010).
45. Tippets, C. A. *et al.* Dynamic Optical Gratings Accessed by Reversible Shape Memory. *ACS Appl. Mater. Interfaces* **7**, 14288–14293 (2015).
46. Lipomi, D. J. *et al.* Skin-like pressure and strain sensors based on transparent elastic films of carbon nanotubes. *Nat Nano* **6**, 788–792 (2011).
47. Kunzelman, J., Chung, T., Mather, P. T. & Weder, C. Shape memory polymers with built-in threshold temperature sensors. *J. Mater. Chem.* **18**, 1082–1086 (2008).
48. Shirinov, A. V. & Schomburg, W. K. Pressure sensor from a PVDF film. *Sens. Actuators Phys.* **142**, 48–55 (2008).
49. Bar-Cohen, Y. & Zhang, Q. Electroactive polymer actuators and sensors. *Mrs Bull.* **33**, 173–181 (2008).
50. Chen, C.-S. *et al.* Shrinky-Dink microfluidics: 3D polystyrene chips. *Lab. Chip* **8**, 622–624 (2008).
51. Lendlein, A., Jiang, H., Juenger, O. & Langer, R. Light-induced shape-memory polymers. *Nature* **434**, 879–882 (2005).
52. Liu, Y., Boyles, J. K., Genzer, J. & Dickey, M. D. Self-folding of polymer sheets using local light absorption. *Soft Matter* **8**, 1764–1769 (2012).
53. Habault, D., Zhang, H. & Zhao, Y. Light-triggered self-healing and shape-memory polymers. *Chem. Soc. Rev.* **42**, 7244–7256 (2013).
54. Hubbard, A. M., Mailen, R., Zikry, M., Dickey, M. & Genzer, J. Controllable Curvature from Planar Polymer Sheets in Response to Light. *Soft Matter* (2017).
55. Lee, Y., Lee, H., Hwang, T., Lee, J.-G. & Cho, M. Sequential Folding using Light-activated Polystyrene Sheet. *Sci. Rep.* **5**, 16544 (2015).
56. Liu, Y., Shaw, B., Dickey, M. D. & Genzer, J. Sequential folding of polymer sheets. (2017).
57. Davis, D., Mailen, R., Genzer, J. & Dickey, M. D. Self-folding of polymer sheets using microwaves and graphene ink. *RSC Adv.* **5**, 89254–89261 (2015).

58. He, Z., Satarkar, N., Xie, T., Cheng, Y.-T. & Hilt, J. Z. Remote Controlled Multishape Polymer Nanocomposites with Selective Radiofrequency Actuations. *Adv. Mater.* **23**, 3192–3196 (2011).
59. Small, W., Wilson, T. S., Benett, W. J., Loge, J. M. & Maitland, D. J. Laser-activated shape memory polymer intravascular thrombectomy device. *Opt Express* **13**, 8204–8213 (2005).
60. Laflin, K. E., Morris, C. J., Muqeem, T. & Gracias, D. H. Laser triggered sequential folding of microstructures. *Appl. Phys. Lett.* **101**, 131901/1-4 (2012).
61. Liu, Y., Miskiewicz, M., Escuti, M. J., Genzer, J. & Dickey, M. D. Three-dimensional folding of pre-strained polymer sheets via absorption of laser light. *J. Appl. Phys.* **115**, (2014).
62. Piqué, A., Mathews, S., Birnbaum, A. & Charipar, N. Microfabricating 3D structures by laser origami. *SPIE Newsroom* (2011).
63. Long, K. N., Scott, T. F., Jerry Qi, H., Bowman, C. N. & Dunn, M. L. Photomechanics of light-activated polymers. *J. Mech. Phys. Solids* **57**, 1103–1121 (2009).
64. Mu, X. *et al.* Photo-induced bending in a light-activated polymer laminated composite. *Soft Matter* **11**, 2673–2682 (2015).
65. Ryu, J. *et al.* Photo-origami—Bending and folding polymers with light. *Appl. Phys. Lett.* **100**, 161908/1-5 (2012).
66. Leong, T. G. *et al.* Tetherless thermobiochemically actuated microgrippers. *Proc. Natl. Acad. Sci.* **106**, 703–708 (2009).
67. Meng, Y., Jiang, J. & Anthamatten, M. Body temperature triggered shape-memory polymers with high elastic energy storage capacity. *J. Polym. Sci. Part B Polym. Phys.* **54**, 1397–1404 (2016).
68. Lendlein, A. Biodegradable, Elastic Shape-Memory Polymers for Potential Biomedical Applications. *Science* **296**, 1673–1676 (2002).
69. Bothe, M. & Pretsch, T. Bidirectional actuation of a thermoplastic polyurethane elastomer. *J. Mater. Chem. A* **1**, 14491–14497 (2013).
70. Zhou, J., Li, Q., Turner, S. A., Ashby, V. S. & Sheiko, S. S. Isothermal programming of triple shape memory. *Polymer* **72**, 464–470 (2015).
71. Ebara, M., Uto, K., Idota, N., Hoffman, J. M. & Aoyagi, T. Rewritable and shape-memory soft matter with dynamically tunable microchannel geometry in a biological temperature range. *Soft Matter* **9**, 3074–3080 (2013).

72. Wu, X., Yang, X., Zhang, Y. & Huang, W. A new shape memory epoxy resin with excellent comprehensive properties. *J. Mater. Sci.* **51**, 3231–3240 (2016).
73. Zhao, Q., Zou, W., Luo, Y. & Xie, T. Shape memory polymer network with thermally distinct elasticity and plasticity. *Sci. Adv.* **2**, e1501297 (2016).
74. Shree, S. *et al.* in *3rd International Conference on Nanotechnologies and Biomedical Engineering* (eds. Sontea, V. & Tiginyanu, I.) **55**, 146–148 (Springer, 2016).
75. Cantrell, J. T., Van Hall, J. R., Young, A. J. & Ifju, P. G. in *Experimental and Applied Mechanics, Vol 4* (eds. Sciammarella, C., Considine, J. & Gloeckner, P.) 1–10 (Springer, 2016).
76. J. Hu, Y. Zhu, H. Huang, J. Lv. Two-way shape memory composite material capable of achieving electroresponse stretching deformation under prestress and preparing method thereof. CN 105670272 A (2016).
77. Browne A. & Johnson N. Shape memory polymer temperature sensing devices and methods of use US 7628116 B2 (2009).
78. Dolynchuk, O., Kolesov, I. & Radusch, H.-J. in *Proceedings of Pps-30: The 30th International Conference of the Polymer Processing Society* (ed. Jana, S. C.) **1664**, 030002 (Amer Inst Physics, 2015).
79. Samuel, C., Raquez, J.-M. & Dubois, P. in *Proceedings of Pps-30: The 30th International Conference of the Polymer Processing Society* (ed. Jana, S. C.) **1664**, 030005 (Amer Inst Physics, 2015).
80. Cho, J. H. *et al.* Nanoscale Origami for 3D Optics. *Small* **7**, 1943–1948 (2011).
81. Azam, A., Laflin, K. E., Jamal, M., Fernandes, R. & Gracias, D. H. Self-folding micropatterned polymeric containers. *Biomed. Microdevices* **13**, 51–58 (2011).
82. Deng, D. & Chen, Y. Origami-Based Self-Folding Structure Design and Fabrication Using Projection Based Stereolithography. *J. Mech. Des.* **137**, 021701 (2015).
83. Davis, D., Chen, B., Dickey, M. D. & Genzer, J. Self-folding of Thick Polymer Sheets Using Gradients of Heat. *J. Mech. Robot.* **8**(3), 031014 (2015).
84. Deng, T. *et al.* Self-folding graphene-polymer bilayers. *Appl. Phys. Lett.* **106**, 203108/1-4 (2015).

85. Zeng, C., Seino, H., Ren, J. & Yoshie, N. Polymers with Multishape Memory Controlled by Local Glass Transition Temperature. *ACS Appl. Mater. Interfaces* **6**, 2753–2758 (2014).
86. Ilievski, F., Mazzeo, A. D., Shepherd, R. F., Chen, X. & Whitesides, G. M. Soft Robotics for Chemists. *Angew. Chem. Int. Ed.* **50**, 1890–1895 (2011).
87. Kim, S., Laschi, C. & Trimmer, B. Soft robotics: a bioinspired evolution in robotics. *Trends Biotechnol.* **31**, 287–294 (2013).
88. Wehner, M. *et al.* Pneumatic Energy Sources for Autonomous and Wearable Soft Robotics. *Soft Robot.* **1**, 263–274 (2014).
89. Zakharchenko, S., Puretskiy, N., Stoychev, G., Stamm, M. & Ionov, L. Temperature controlled encapsulation and release using partially biodegradable thermo-magneto-sensitive self-rolling tubes. *Soft Matter* **6**, 2633–2636 (2010).
90. Boncheva, M. *et al.* Magnetic self-assembly of three-dimensional surfaces from planar sheets. *Proc. Natl. Acad. Sci. U. S. A.* **102**, 3924–3929 (2005).
91. In, H. J., Lee, H., Nichol, A. J., Kim, S. G. & Barbastathis, G. Carbon nanotube-based magnetic actuation of origami membranes. *J. Vac. Sci. Technol. B* **26**, 2509–2512 (2008).
92. Judy, J. W. & Muller, R. S. Magnetically actuated, addressable microstructures. *J. Microelectromechanical Syst.* **6**, 249–256 (1997).
93. Ebefors, T., Kälvesten, E. & Stemme, G. Dynamic actuation of polyimide V-groove joints by electrical heating. *Sens. Actuators Phys.* **67**, 199–204 (1998).
94. Felton, S. M. *et al.* Self-folding with shape memory composites. *Soft Matter* **9**, 7688–7694 (2013).
95. Felton, S. M., Tolley, M. T., Onal, C. D., Rus, D. & Wood, R. J. Robot self-assembly by folding: A printed inchworm robot. in 277–282 (IEEE International Conference on Robotics and Automation, 2013).
96. Sellinger, A. T., Wang, D. H., Tan, L.-S. & Vaia, R. A. Electrothermal Polymer Nanocomposite Actuators. *Adv. Mater.* **22**, 3430–3435 (2010).
97. Serman, Y., Demaine, E. D. & Oxman, N. PCB Origami: A Material-Based Design Approach to Computer-Aided Foldable Electronic Devices. *J. Mech. Des.* **135**, 114502/1-4 (2013).

98. Khan, F. & Singh, K. An experimental investigation of the effect of strain on the electrical conductivity of a shape memory polymer. *Polym. Test.* **49**, 82–87 (2016).
99. Pan, M., Yuan, Q.-J., Gong, X.-L., Zhang, S. & Li, B.-J. A Tri-Stimuli-Responsive Shape-Memory Material Using Host–Guest Interactions as Molecular Switches. *Macromol. Rapid Commun.* **37**, 433–438 (2016).
100. Forterre, Y., Skotheim, J. M., Dumais, J. & Mahadevan, L. How the Venus flytrap snaps. *Nature* **433**, 421–425 (2005).
101. Williams, S. E. & Bennett, A. B. Leaf Closure in the Venus Flytrap: An Acid Growth Response. *Science* **218**, 1120–1122 (1982).
102. Ionov, L. Bioinspired Microorigami by Self-Folding Polymer Films. *Macromol. Chem. Phys.* **214**, 1178–1183 (2013).
103. Studart, A. R. & Erb, R. M. Bioinspired materials that self-shape through programmed microstructures. *Soft Matter* **10**, 1284–1294 (2014).
104. Leite, Á. J., Caridade, S. G. & Mano, J. F. Synthesis and characterization of bioactive biodegradable chitosan composite spheres with shape memory capability. *J. Non-Cryst. Solids* **432**, 158–166 (2016).
105. Jiang, H. Y., Kelch, S. & Lendlein, A. Polymers Move in Response to Light. *Adv. Mater.* **18**, 1471–1475 (2006).
106. Liu, Y., Mailen, R., Zhu, Y., Dickey, M. D. & Genzer, J. Simple geometric model to describe self-folding of polymer sheets. *Phys. Rev. E* **89**, 042601 (2014).
107. Mailen, R., Liu, Y., Dickey, M. D., Zikry, M. & Genzer, J. Modeling of shape memory polymer sheets that self-fold in response to localized heating. *Soft Matter* **11**, 7827–7834 (2015).
108. Das, S., Varghese, S. & Kumar, N. S. S. Butadiene-Based Photoresponsive Soft Materials. *Langmuir* **26**, 1598–1609 (2010).
109. Ma, J. *et al.* A photoviscoplastic model for photoactivated covalent adaptive networks. *J. Mech. Phys. Solids* **70**, 84–103 (2014).
110. Barrett, C. J., Mamiya, J., Yager, K. G. & Ikeda, T. Photo-mechanical effects in azobenzene-containing soft materials. *Soft Matter* **3**, 1249–1261 (2007).
111. Biggs, J. *et al.* Electroactive Polymers: Developments of and Perspectives for Dielectric Elastomers. *Angew. Chem. Int. Ed.* **52**, 9409–9421 (2013).

112. Zeng, H. *et al.* Light-Fueled Microscopic Walkers. *Adv. Mater.* **27**, 3883–3887 (2015).
113. Yan, Z. *et al.* Controlled Mechanical Buckling for Origami-Inspired Construction of 3D Microstructures in Advanced Materials. *Adv. Funct. Mater.* **26**, 2629–2639 (2016).
114. Martinez, R. V., Fish, C. R., Chen, X. & Whitesides, G. M. Elastomeric Origami: Programmable Paper-Elastomer Composites as Pneumatic Actuators. *Adv. Funct. Mater.* **22** 1376–1384 (2012).
115. Kusuda, S., Sawano, S. & Konishi, S. Fluid-resistive bending sensor having perfect compatibility with flexible pneumatic balloon actuator. in *IEEE 20th International Conference on Micro Electro Mechanical Systems, 2007. MEMS* 615–618 (2007).
116. Ahmed, S., McGough, K., Ounaies, Z. & Frecker, M. Origami-Inspired Folding and Unfolding of Structures: Fundamental Investigations of Dielectric Elastomer-Based Active Materials. in *ASME Proceedings V001T01A029/1-6* (2013).
117. Anderson, I. A., Gisby, T. A., McKay, T. G., O'Brien, B. M. & Calius, E. P. Multi-functional dielectric elastomer artificial muscles for soft and smart machines. *J. Appl. Phys.* **112**, 041101/1-20 (2012).
118. Hsu, Y.-J., Jia, Z. & Kymissis, I. A Locally Amplified Strain Sensor Based on a Piezoelectric Polymer and Organic Field-Effect Transistors. *IEEE Trans. Electron Devices* **58**, 910–917 (2011).
119. Kroemer, N., Manthey, W., Kuenstler, W., Danz, R. & Geiss, D. Ultrasonic transducers using piezoelectric PVDF films. in *Electrets, 1988. (ISE 6) Proceedings., 6th International Symposium on (IEEE Cat. No.88CH2593-2)* 379–383 (1988).

CHAPTER 2

Self-folding of Polymer Sheets Using Microwaves and Graphene Ink

* This chapter is based on Davis, D., Mailen, R., Genzer, J. & Dickey, M. D. Self-folding of polymer sheets using microwaves and graphene ink. *RSC Adv.* **5**, 89254–89261 (2015)

Overview

Self-folding represents an attractive way to convert two-dimensional (2D) material sheets into three-dimensional (3D) objects in a hands-free manner. This chapter demonstrates a simple approach to self-fold thin pre-strained polystyrene (PS) sheets using microwaves. While the PS sheets are transparent to microwaves, patterns of screen-printed ink containing graphene absorb microwaves and cause the underlying printed sections of the sheet to warm up. When the local temperature in the inked region exceeds the glass transition temperature of PS ($\sim 103^{\circ}\text{C}$), the strain in the inked regions of the film relaxes gradually across the sheet thickness, which causes the PS sheet to fold. The resulting dihedral angle is proportional to the width of the hinge printed by graphene ink. The geometry and azimuthal orientation of the sample inside the microwave reactor affect the quality of the folding due to the non-uniformity of the microwave energy inside the reactor. While self-folding has previously utilized heat, light, photo-chemistry, and solvent swelling, this chapter reports the use of microwaves, which can deliver large amounts of energy remotely.

2.1 Introduction

This chapter describes the self-folding of polymer sheets using microwaves (frequency ~ 2.45 GHz) as a heating source to achieve a wide range of dihedral angles that fold within seconds. Self-folding strategies convert planar surfaces into three-dimensional (3D) objects in a hands-free manner. Self-folding is attractive for a number of applications, including remote deployment of compact structures¹⁻³, assembly⁴, packaging⁵, robotics^{6,7}, mechanical metamaterials⁸, and mechanical actuation⁹. In general, sheets that self-fold have two common features: (1) a 'hinged' region that differs chemically, physically, or mechanically from the rest of the sheet, and (2) a force that arises in response to an external stimulus and causes the hinged region to fold. Previously, researchers induced self-folding using light¹⁰⁻²⁹, heat^{9,28,30-}

³⁷, lasers^{38–43}, pH⁴⁴, swelling^{45–50}, electricity^{4,51–57}, magnets^{58–61}, and pneumatics^{62–64}. This work demonstrates it is also possible to use microwaves to induce self-folding. Although there are a number of approaches to self-folding⁶⁵, the method described here is most closely related to those that utilize localized heating of shrink films (i.e., shape memory polymers) to induce folding²⁴. In this context, microwaves are appealing because they can be generated easily to deliver large amounts of energy from large distances. Microwave ovens are also common household items and, in principle, could be utilized to convert flat objects shipped to the home into 3D objects.

Microwaves are electromagnetic waves with a frequency between 300 MHz and 300 GHz. Most commercial microwave ovens use a frequency of 2.45 GHz, including the one utilized in our studies. Microwaves deliver heat via dielectric heating (also known as electronic heating), which results from molecular dipoles in a material absorbing the microwaves and orienting themselves with or against the oscillating electric field^{66–72}. When the dipoles cannot re-orient as fast as the frequency of the electric field, they remain out of phase with the electric field created from the microwave^{66–72}. This lag (i.e., dielectric loss) causes energy to be dissipated in the form of heat. Thus, the dielectric loss of a material determines how much microwave energy a given material can absorb. While polymers generally do not absorb microwaves effectively, a number of materials absorb microwaves, including graphene and graphite^{68,71}.

In this work, we utilize Vor-inktm as a microwave absorbing ink. This ink comprises a heterogeneous mixture that includes graphene, iron oxide, solvent, and polymer stabilizers. We chose this ink because it absorbs microwaves effectively, it is easy to pattern, and it is commercially available. We screen printed the ink on the surface of sheets of prestrained PS to create 'hinges' with well-defined geometry (i.e., size and position). Whereas many self-folding approaches utilize multi-step fabrication strategies to define hinges, the simple screen printing approach utilized here creates hinges in a single step on a commercially available,

homogeneous plastic sheet. Previously, patterns of ink have been utilized to locally heat the underlying polymer by light absorption²⁴ and Joule heating⁵⁷. Here, the absorbance of microwaves by the ink causes the polymer underneath the ink to heat. When the local temperature in the sheet exceeds the glass transition temperature of PS ($\sim 103\text{ }^{\circ}\text{C}$)²⁴, the strain in that region of the film relaxes in a gradual fashion across the sheet thickness, causing the PS sheet to fold in the direction towards the inked side of the sheet. Thus, the ink defines a hinge in the sheet and for the microwave power utilized here, the polymer folds over the course of 1-3 seconds starting from room temperature. This chapter demonstrates self-folding of polymer sheets using microwaves and shows that the hinge geometry, the sample orientation in the microwave reactor, and the power of the microwave control the angle, times scales, and quality of the self-folding.

2.2 Experimental System with Graphene Ink and Geometric Model

We first sought to demonstrate that it is possible to use microwaves to induce self-folding of polymer sheets. **Figure 2.1** shows schematically the process of creating and folding the samples. The substrates consist of prestrained polystyrene films (Shrinky-DinkTM, 300 μm thick) screen-printed with lines of graphene ink that also contains $\sim 10\text{ wt}\%$ iron oxide. A micrograph of a screen-printed line is shown in **Figure S2.1** in the Supplementary Information. **Figure S2.2** in the Supplementary Information section depicts a typical height profile ($\sim 50 - 100\text{ }\mu\text{m}$ thick) of the ink that defines the hinge. Graphene and iron oxide both absorb microwaves strongly^{68,71}.

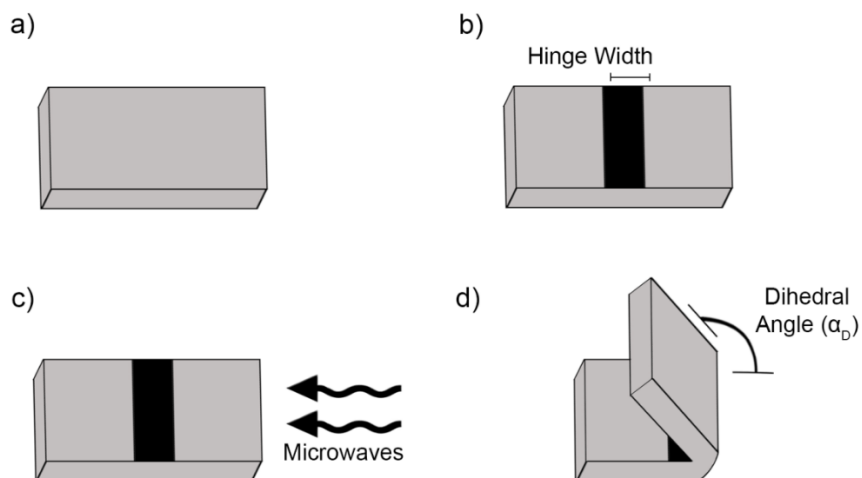


Figure 2.1. Folding process induced by microwaves (not to scale). A pre-strained polystyrene sheet (a) is screen-printed with graphene ink on the surface of the sheet (b); the printed regions define a ‘hinge’. Microwaves heat the ink (c); the microwave source is physically positioned on the right side of the sample, but is designed to create a standing wave inside the vessel of the microwave reactor. The sample folds to α_D due to the localized heating of the inked region in the sample via absorption of microwaves (d).

A microwave reactor heats the samples, which rest against the bottom of a cylindrical glass chamber inside the reactor (85 mm deep and 20 mm diameter). Microwave ovens designed for food operate at a power of 900 W, but the reactor here was operated at 250 W. We expose the samples to 250 W of power for up to 3 s, resulting in dihedral angles (α_D) ranging from 0° to 180° by varying only the hinge width, as shown in **Figure 2.2**. Shorter exposure times result in less folding. Times longer than 3 s often result in distorted samples and in some cases, ignition, which shows how effectively the ink absorbs the microwaves. The polymer portion of the sample is transparent to microwaves and consequently does not heat up.

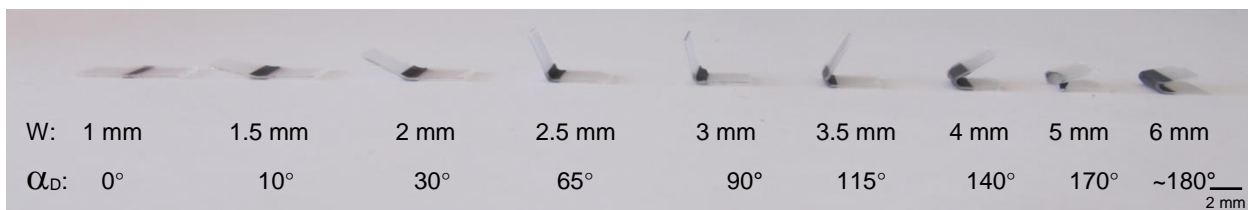


Figure 2.2. The maximum α_D increases with increasing hinge width (W). The samples are 6 mm wide in the dimension parallel to the hinge.

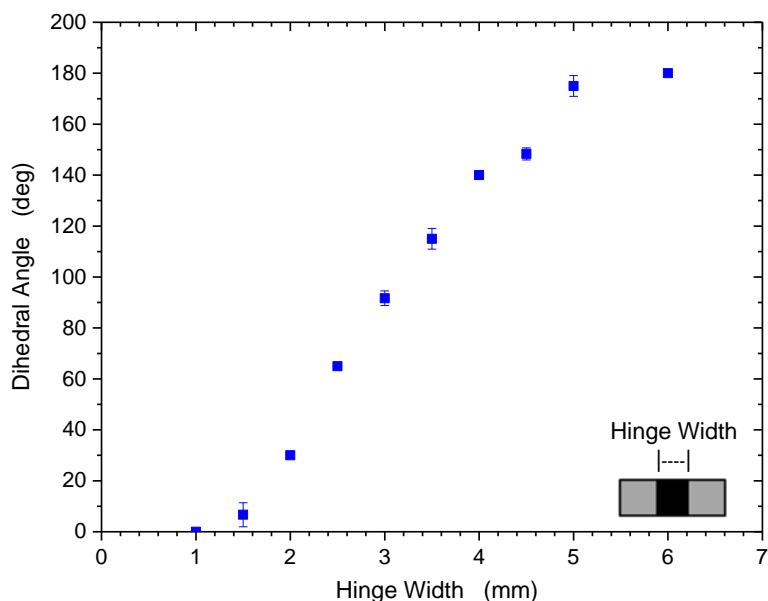


Figure 2.3. Dihedral angle as a function of the hinge width. The error bars capture the first standard deviation with a minimum of 3 repetitions of each hinge width with all other variables held constant. These samples are all exposed to a microwave power of 250 W, an orientation of 90°, and a square-shaped hinge composed of graphene ink (see text).

2.3 Azimuthal Orientation Effect of Folding

During these measurements, we observed that the folding behavior of the samples depends strongly on both the sample geometry and the in-plane (*i.e.*, azimuthal) orientation of the hinge inside the microwave reactor. Samples folded most reliably when oriented at 90°; *i.e.*, with the long axis of the hinge aligned perpendicular to both the front panel of the instrument and therefore, perpendicular to the source of microwaves. **Figures 2.2** and **2.3** report the folding

behavior of samples oriented azimuthally at 90° . We sought to understand why the other sample orientations folded poorly (azimuthal angle $\sim 45^\circ$) or not at all (azimuthal angle $\sim 0^\circ$) by varying systematically the orientation, geometry, and microwave power. We hypothesize that folding depends on sample orientation due to the non-uniformity of microwaves inside the reactor, which cause non-uniform heating of the hinge.

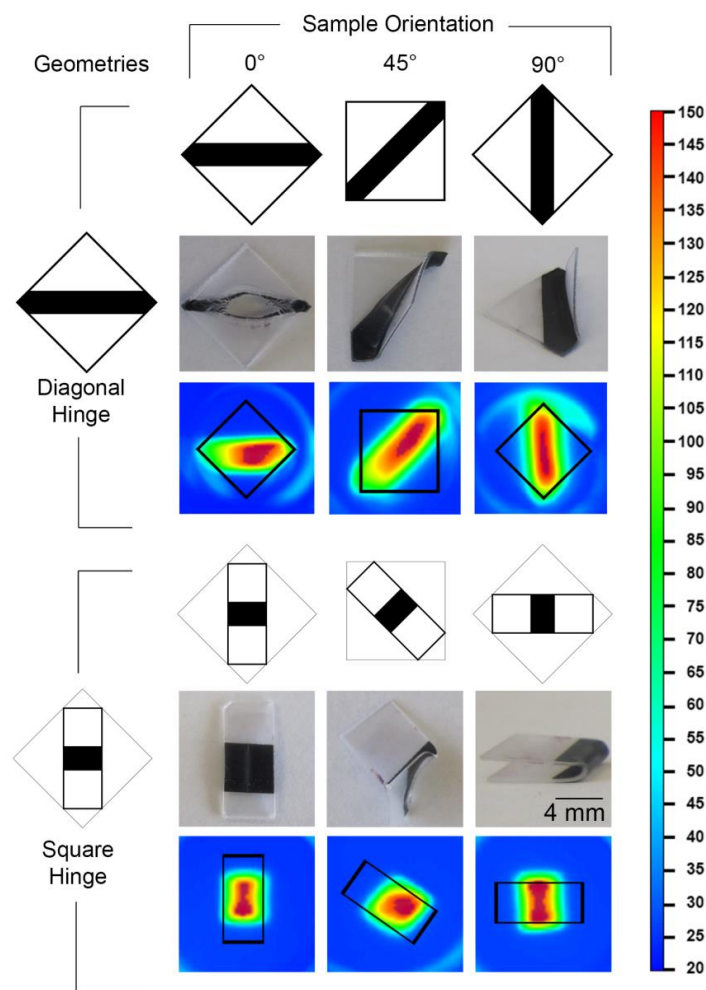


Figure 2.4. Two sample geometries ('diagonal hinge' and 'square hinge' groups) are depicted at 3 different sample orientations (columns) relative to the direction of the microwave source. The top row of each group is a cartoon of the sample, the middle row contains photographs of samples after exposure to 3 s of microwave, and the bottom row is an IR image of the sample slightly before it begins to move in response to microwaves (with the temperature scale on the right side).

We chose two different geometries in our study, as depicted in **Figure 2.4**. The diagonal hinge geometry spanned the diameter of the microwave vessel to explore the uniformity of the heating of the hinges. The diagonal hinge geometry consists of a 13 mm x 13 mm polystyrene square with a hinge spanning opposite corners. This sample had the maximum possible hinge length (17 mm) that can fit in the microwave without touching the vessel walls. The square hinge geometry consists of 13 mm x 6 mm PS rectangle with a centered, square-shaped hinge. The use of a square-shape minimizes the effect of orientation on the average temperature of the hinge but not its effect on folding.

The self-folding studied here is a thermally-driven process. To test if uneven heating causes variation in folding behavior with respect to sample orientation, we utilized an IR camera to measure the surface temperature of the hinge during exposure to the microwaves. Changing the orientation of the samples changed the temperature profile of the hinge during the microwave heating. **Figure 2.5** plots the average temperature of the hottest region of the hinge versus time for each of the six possible combinations of sample geometry and orientation using samples with a 3 mm hinge width exposed to 250 W of microwave power. The 'square hinges' have temperature profiles that are nearly independent of orientation, whereas the profiles for 'diagonal hinges' vary with alignment. To quantify the heating rate of the surface, we fit the experimental data (cf. **Figure 2.5**) to a *tanh* function and define the maximum heating rate as a tangent at the inflection point of the *tanh* function (see **Figure S2.5** in Supporting Information). **Figure 2.6** plots the maximum heating rates for each sample configuration.

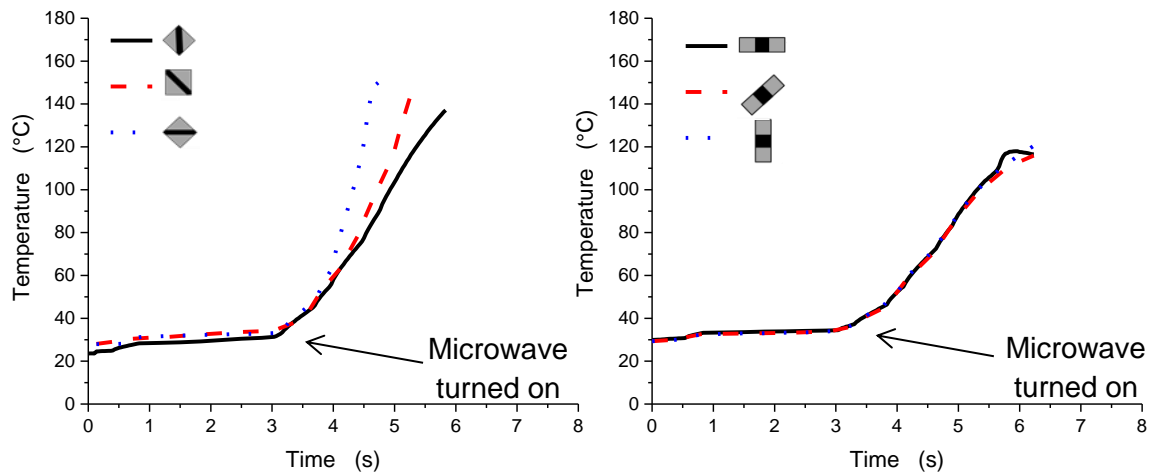


Figure 2.5. Time-dependence of temperature in a) ‘diagonal hinge’ samples with varying orientation and hinge width of 3 mm; b) ‘square hinge’ samples with hinge width of 3 mm. The microwave power is 250 W in both cases. The IR camera cannot measure accurately temperatures above 150°C and therefore the data truncates at that value.

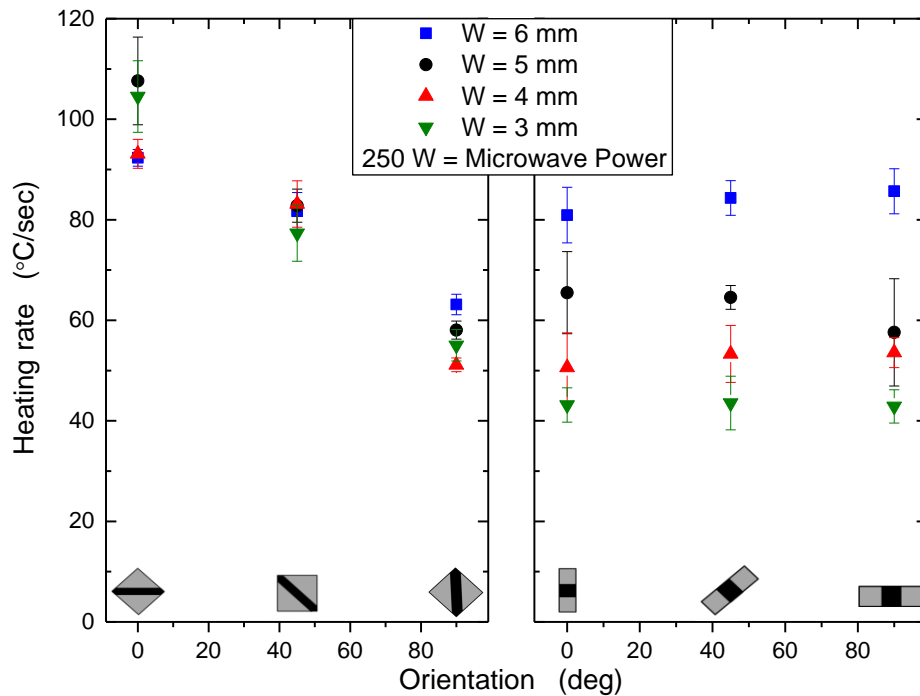


Figure 2.6. Heating rate of the samples at different orientation relative to the direction of the microwave radiation (azimuthal angle) and hinge widths (W) are shown.

The results in **Figure 2.6** confirm that the orientation affects the maximum heating rate of the samples with a 'diagonal hinge' more than the hinge width. Because the diagonal hinges span the walls of the reactor, this result suggests that there is a strong variation in microwave power around the perimeter of the reactor. Samples oriented at 0° and 45° did not heat uniformly along the long axis of the hinge (see **Figure S2.3** and **S2.4** in Supporting information and the images in **Figure 2.4**). This non-uniformity causes distortion (0° orientation) and off-center folding (45° orientation). We observed a few sparks during the folding of all three orientations but they were most pronounced during samples orientated at 0° . The sparks appear to partially ablate the ink for the 0° samples, but do not seem to affect the folding of 45° or 90° samples; eliminating sparks may be possible by optimizing the resistivity of the ink. In the square hinge samples, the orientation does not affect the maximum heating rate since the areal coverage of the graphene ink remains centered in the reactor regardless of orientation. For these samples, the hinge width affects the maximum heating rate much more than the sample orientation. The trends in the data shown in **Figure 2.6** also occur at 30 W microwave power (see Supporting Information).

The data in **Figure 2.6** motivated us to study the uniformity of the microwaves in the vessel. We mapped the heating profile inside the microwave using a paper (MWAC, Atlanta Chemical) that absorbs microwaves and changes color permanently due to thermal excursions above a temperature of 65°C . **Figure 2.7** shows pictures of the paper after exposure to different durations of microwave heating. The color 'front' propagates across the paper with time, illustrating the non-uniformity in the aerial microwave intensity.

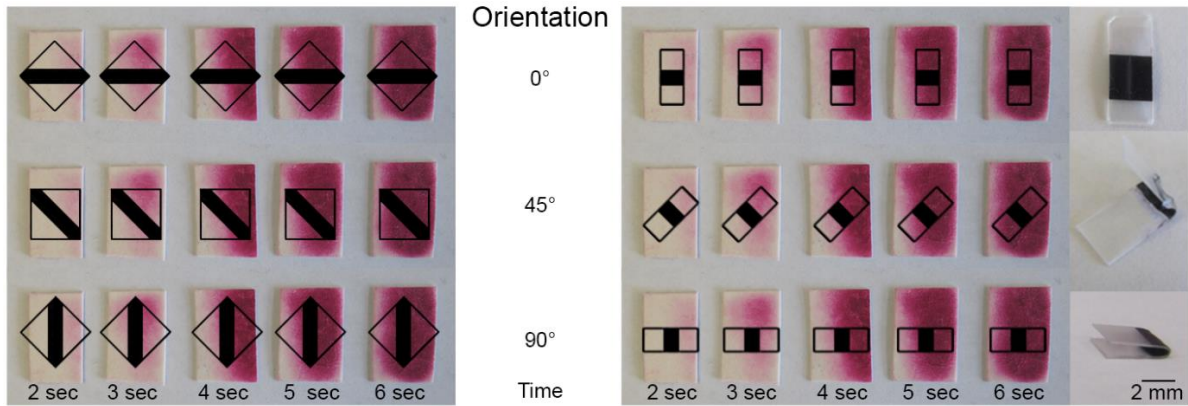


Figure 2.7. Microwave sensitive paper changes color when heated by microwaves to show the non-uniformity of microwaves. Depictions of the polymer samples are superimposed over the paper for the sake of visualization. The microwaves heat non-uniformly, which explains why the hinges at 90° orientation fold and 0 and 45° deform, as shown in the photographs located in the right-most column.

For the sake of visualization, **Figure 2.7** superimposes the geometry and orientation of the hinges (which were not present while heating the paper). It also displays the three types of folding behaviors observed as a result of orientation in otherwise identical samples. The 0° sample shows the beginnings of ‘cratering’; portions of the polymer in the hinge region flow away from the hinge, but the sample does not fold due to the physical restraint offered by the portions of the hinge that remain below the T_g of the sheet. The 45° sample folds unevenly. The 90° samples fold very well (cf. **Figure 2.2**). These results highlight the effects of non-uniform heating on the folding process.

2.4 Thermally Modelled Simulation Results

To gain a better understanding of the response of the samples to microwave induced heating we modeled the folding process using Abaqus finite element analysis software. The model is based primarily on a model developed for the self-folding of pre-strained polystyrene sheets that fold due to IR induced heating⁷³. Briefly, the model starts by pre-straining the polymer sheet at an elevated temperature prior to cooling the sheet to preserve the pre-strained state.

From the pre-strained state, we impose representative thermal and mechanical boundary conditions. The temperature distribution measured experimentally across the surface of the samples serves as a thermal boundary condition. The model predicts the resulting deformation based on the strain relaxation of the polymer in response to this thermal profile. Square and diagonal hinge geometries are modeled each with 6 mm wide hinges oriented at a 90° azimuthal angle. **Figure 2.8** shows representative results from these simulations.

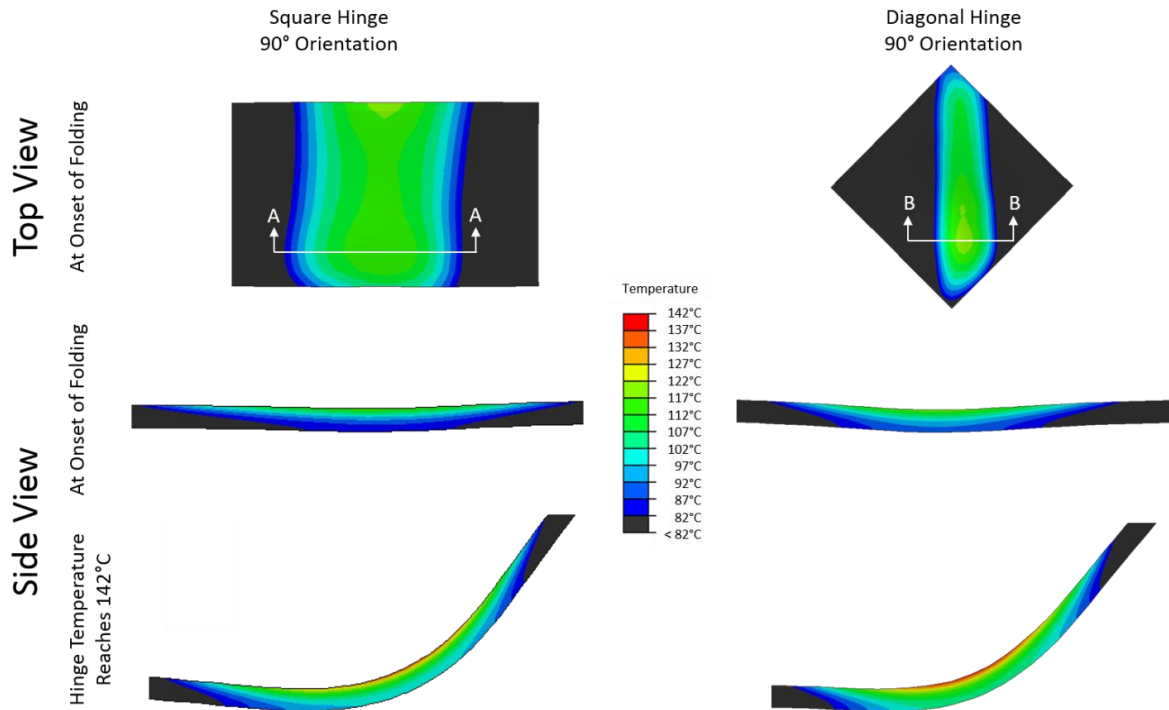


Figure 2.8. Results from Abaqus model that show the temperature profile on the surface (top view) and through the thickness of the samples (side view) oriented at 90°. The images truncate the regions outside the hinge region for better visualization of the thermal profile of the hinge. The side view images are expanded to the distance ‘A’ and ‘B’ (which are equal). The black portion of the image is the edge of the unheated polymer.

At the onset of folding (middle row in **Figure 2.8**) the maximum patterned surface temperature for both hinge geometries is ~117°C while the bottom surface is ~82°C, a

difference of 35°C. Later in the folding process, when the patterned surface temperature reaches ~142°C (bottom row in **Figure 2.8**), the temperature on the bottom surface is ~102°C, a difference of 40°C. This temperature gradient is double the temperature gradient seen in IR induced folding samples²⁴. The folding happens within seconds because the microwaves efficiently deliver large amounts of heat locally to a patterned hinge. Although the bottom of the sample approaches T_g during folding, the onset of folding occurs when the bottom of the microwave sample is significantly below T_g . Folding of the sample prior to the bottom surface reaching T_g is due to the large temperature gradient in the microwave samples, which is remarkably large considering the sheets are only ~300 μm thick.

2.5 Conclusions

This chapter demonstrates self-folding of pre-strained polymer films using microwaves as a heating source. A pattern of graphene ink on the surface of pre-strained polymer films absorbs the microwaves and causes the polymer to shrink directly below the hinge, which induces the polymer sheet to fold. The dihedral angle is directly proportional to the hinge width printed on the polymer sheet and it is possible to self-fold all the way to 180°. The quality of the folding depends on the geometry and orientation of the sample due to uneven distribution of microwaves energy in the microwave reactor (commercial microwaves also have non-uniform heating). The best folding occurs when the hinge receives as uniform heating as possible across its length, which occurs at an azimuthal sample orientation of 90° within the reactor. A finite element model suggests that the absorption of microwave energy by the hinge results in a temperature difference of ~40 °C from top to bottom of the polymer samples. This large temperature difference explains why the samples are able to fold within seconds despite starting at room temperature.

Polymer sheets that fold in response to microwaves could have several applications, particularly since microwaves are common household items. Here, we utilize graphene inks, but it is possible to use other microwave absorbers including materials that might be optically transparent. This technique folds polymers quickly and accurately which lends itself to time sensitive applications. This technique could be used for triggering remote folding or for activating folding within enclosures or through materials transparent to microwaves.

2.6 Acknowledgements

The authors thank the National Science Foundation for supporting this work under the NSF EFRI program (Grant No. 1240438). We also thank Professor Chris Gorman for access to his CEM LabMate microwave, Progressive Graphics (<http://www.progressivegraphics.net>) for their screen printing expertise, and our EFRI Collaborators for their constructive feedback.

Experimental Section

Onto Shrinky-Dink™ sheets (prestrained polystyrene), we screen printed Vor-ink™ (graphene ink) as straight lines using a 180 mesh screen. The lines define the 'hinges' and have widths from 1–6 mm. Next, we laser cut two different sized samples from the inked sheets: 13 mm x 13 mm and 13 mm x 6 mm rectangles. We placed the samples onto a CEM Discover microwave oven and heated the samples at 250 W. We tested three different physical orientations (0°, 45°, and 90°) up to 60 seconds (although most trials ended much earlier). We used an IR camera to record the surface temperature profiles.

Supplementary Information

Approximating the temporal evolution of temperature

The temperature in the heating profiles can be approximated by the *tanh* function:

$$T(t) = \frac{c}{2} [\tanh(a(t-t_0)) + 1] + T_0 \quad (\text{S2.1})$$

where a , t_0 , c , and T_0 are adjustable parameters. The parameters a and c help define the heating rate (*i.e.*, dT/dt) and t_0 represents the time corresponding to the inflection point in the $T=T(t)$ curve. Using the expression in Equation (S2.1), one can calculate the heating rate as:

$$\begin{aligned} \frac{\partial T(t)}{\partial t} &= \frac{c}{2} \frac{\partial T(t)}{\partial t} [\tanh(a(t-t_0)) + 1] = \\ &= \frac{c}{2} \frac{4a}{[e^{a(t-t_0)} + e^{a(b-t_0)}]^2} = \frac{2ac}{[e^{a(t_0-b)} + e^{a(b-t_0)}]^2} = \\ &= \frac{c}{2} \frac{4a \cdot \cosh^2(a(t-t_0))}{[\cosh(2(a(t-t_0))) + 1]^2} \end{aligned} \quad (\text{S2.2})$$

The maximum heating rate occurs at the inflection point, *i.e.*, $t=t_0$:

$$\frac{\partial T(t)}{\partial t} = \frac{c}{2} \frac{4a}{[e^{a(0)} + e^{a(0)}]^2} = \frac{ac}{2} \quad (\text{S2.3})$$

This inflection point is our representative heating rate for a given sample as shown in **Figure S2.5**. From **Figure S2.5**, the model fits the experimental data until the sample starts to fold. Using this model to find the heating rate, we compare the heating rate of samples with different hinge widths, geometry, orientations, and microwave power as shown in **Figure 2.6**.

Screen Printing

Screen printing is a fabrication method used to apply patterned ink to the surface of a flat object. Openings in the screen are patterned with intense light and then the ink is rolled across the surface using a squeegee. The ink can only pass through the patterned parts of the screen and the squeegee keeps the height of the ink uniform. Screen printing allows for precise patterning of the ink onto the surface of the polystyrene samples.

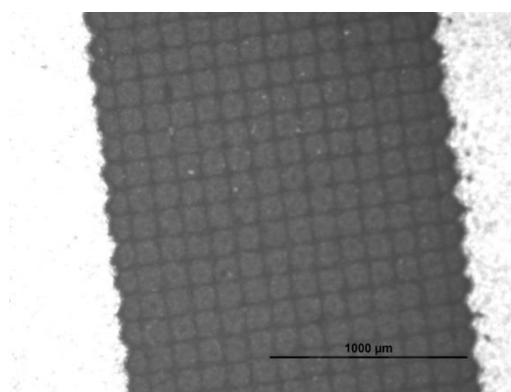


Figure S2.1. Optical microscopy of the screen printed graphene. There are grid lines from the screen as well as the high level of uniformity in the ink pattern.

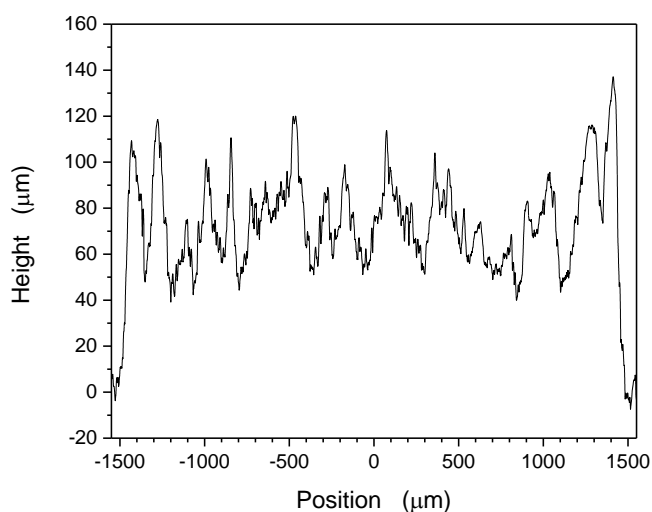


Figure S2.2. Profilometry of screen printed Vor-ink™ (3 mm hinge width). The hinge size varies from 50 to 100 μm for most peaks in the sample with the maximum being over 130 μm.

Sample heating

The temperature scale on the right is common to both plots.

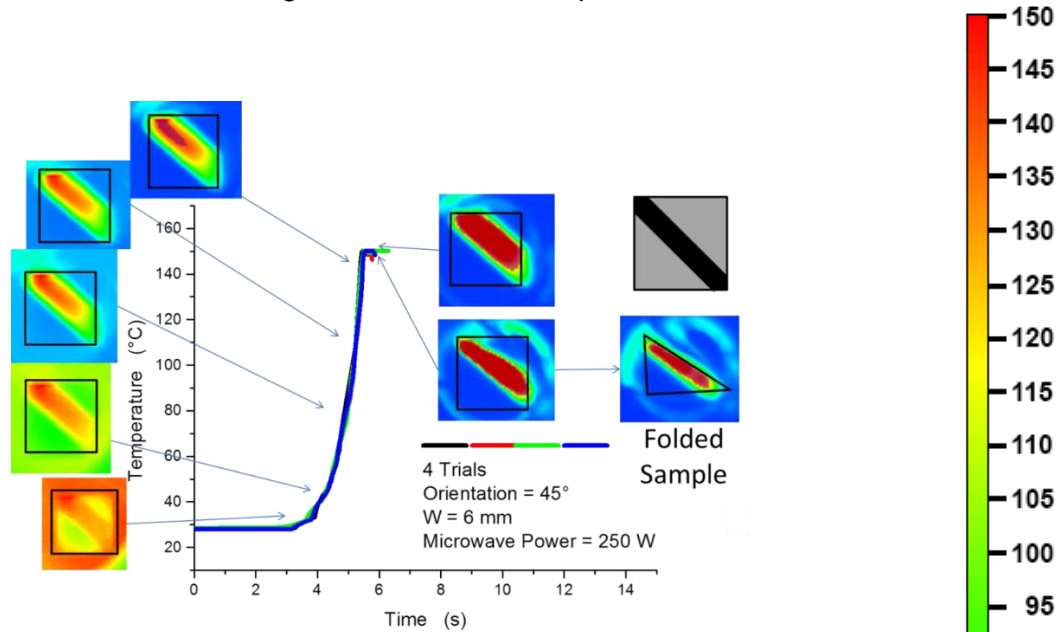


Figure S2.3. Heating profile for a 'rectangular hinge' (6 mm, 250 W, 45° orientation). The pictures are taken with an IR camera and show how the hinge heated non-uniformly. This lack of uniformity in the profile leads to imperfect folding. The camera view is flipped, so the directional heating is left to right instead of right to left. This sample folds in ~6 second. The microwave is then turned off. (Note that the first 2 images do not use the same temperature scale in order to increase visibility of the sample and hinge). The temperature range (in °C) is show in the legend on the right.

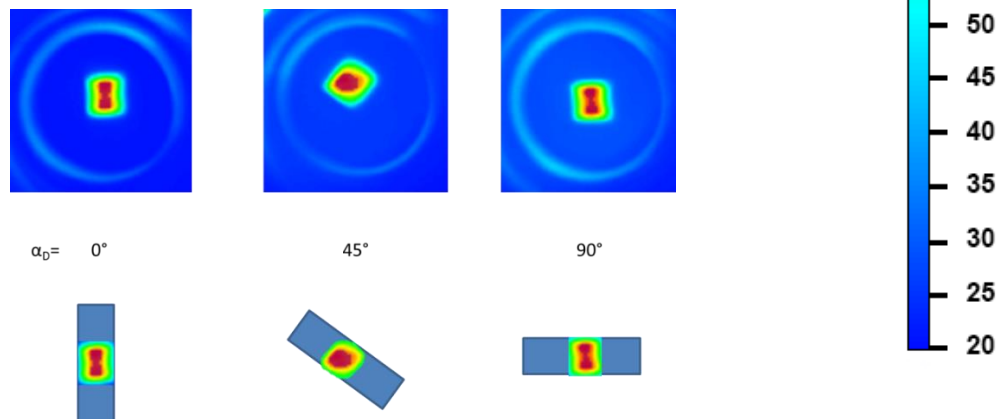


Figure S2.4. Thermal Images of square hinge samples. Even though the heating rate is similar, the orientation controls whether the sample craters or folds. This is likely because the hot region spans the width of the hinge in the 90° sample (without bound) but is bound by stiff polymer in the 0° case. The temperature range (in °C) is show in the legend on the right.

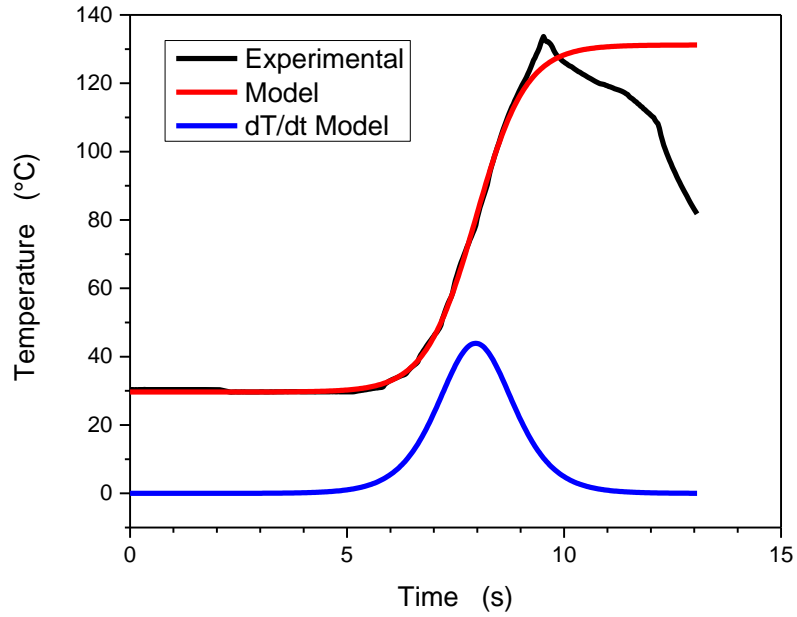


Figure S2.5. Heating profile of a 3 mm 250 W sample (experimental) and the *tanh* fit. Using this fit we found the maximum heating rate via the inflection point of the derivative.

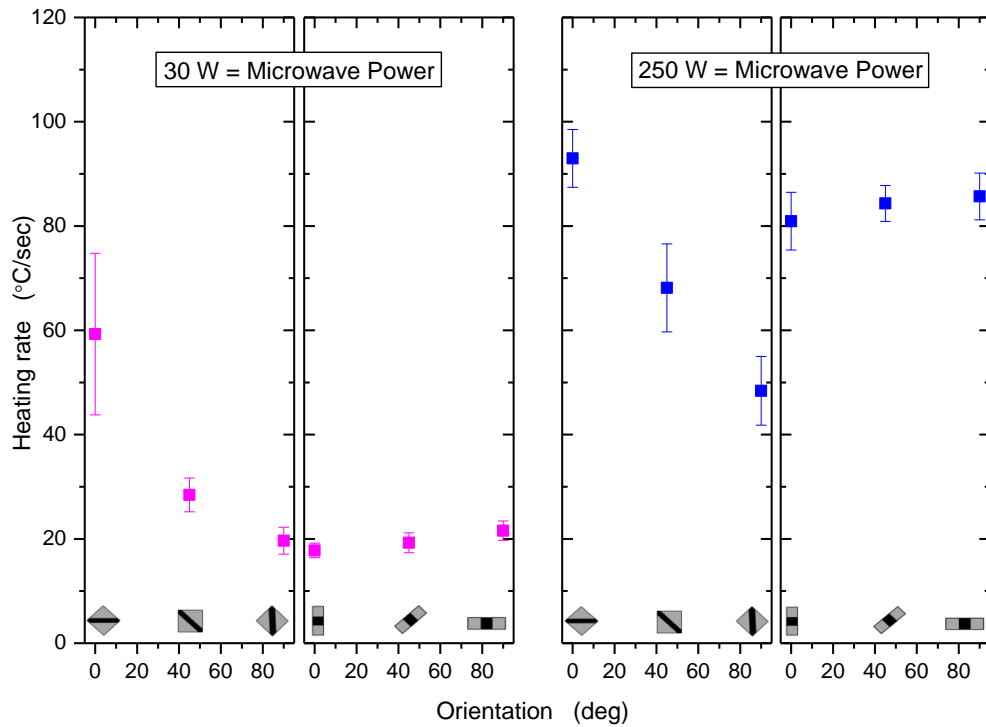


Figure S2.6. Heating rate of the samples ($W = 6$ mm) at different microwave powers and orientation relative to the direction of the microwave radiation (azimuthal angle).

References

1. Taylor, D., Dyer, D., Lew, V. & Khine, M. Shrink film patterning by craft cutter: complete plastic chips with high resolution/high-aspect ratio channel. *Lab. Chip* **10**, 2472–2475 (2010).
2. Lin, S., Lee, E. K., Nguyen, N. & Khine, M. Thermally-induced miniaturization for micro- and nanofabrication: progress and updates. *Lab. Chip* **14**, 3475–3488 (2014).
3. Grimes, A. *et al.* Shrinky-Dink microfluidics: rapid generation of deep and rounded patterns. *Lab. Chip* **8**, 170–172 (2008).
4. Hayes, G. J., Liu, Y., Genzer, J., Lazzi, G. & Dickey, M. D. Self-Folding Origami Microstrip Antennas. *IEEE Trans. Antennas Propag.* **62**, 5416–5419 (2014).
5. Fernandes, R. & Gracias, D. H. Self-folding polymeric containers for encapsulation and delivery of drugs. *Adv. Drug Deliv. Rev.* **64**, 1579–1589 (2012).
6. Felton, S., Tolley, M., Demaine, E., Rus, D. & Wood, R. A method for building self-folding machines. *Science* **345**, 644–646 (2014).
7. Wood, R. J., Avadhanula, S., Sahai, R., Steltz, E. & Fearing, R. S. Microrobot Design Using Fiber Reinforced Composites. *J. Mech. Des.* **130**, 052304–052304 (2008).
8. Silverberg, J. L. *et al.* Using origami design principles to fold reprogrammable mechanical metamaterials. *Science* **345**, 647–650 (2014).
9. Bothe, M. & Pretsch, T. Bidirectional actuation of a thermoplastic polyurethane elastomer. *J. Mater. Chem. A* **1**, 14491–14497 (2013).
10. Ikeda, T., Nakano, M., Yu, Y., Tsutsumi, O. & Kanazawa, A. Anisotropic Bending and Unbending Behavior of Azobenzene Liquid-Crystalline Gels by Light Exposure. *Adv. Mater.* **15**, 201–205 (2003).
11. Leng, J., Wu, X. & Liu, Y. Infrared light-active shape memory polymer filled with nanocarbon particles. *J. Appl. Polym. Sci.* **114**, 2455–2460 (2009).
12. Lee, K. M., Koerner, H., Vaia, R. A., Bunning, T. J. & White, T. J. Light-activated shape memory of glassy, azobenzene liquid crystalline polymer networks. *Soft Matter* **7**, 4318–4324 (2011).
13. Beblo, R. V. & Weiland, L. M. Light Activated Shape Memory Polymer Characterization. *J. Appl. Mech.-Trans. Asme* **76**, 011008/1-8 (2009).

14. Zhang, H., Xia, H. & Zhao, Y. Light-Controlled Complex Deformation and Motion of Shape-Memory Polymers Using a Temperature Gradient. *ACS Macro Lett.* 940–943 (2014).
15. Wang, E., Desai, M. S. & Lee, S.-W. Light-Controlled Graphene-Elastin Composite Hydrogel Actuators. *Nano Lett.* **13**, 2826–2830 (2013).
16. Li, M.-H., Keller, P., Li, B., Wang, X. & Brunet, M. Light-Driven Side-On Nematic Elastomer Actuators. *Adv. Mater.* **15**, 569–572 (2003).
17. Lendlein, A., Jiang, H., Juenger, O. & Langer, R. Light-induced shape-memory polymers. *Nature* **434**, 879–882 (2005).
18. Habault, D., Zhang, H. & Zhao, Y. Light-triggered self-healing and shape-memory polymers. *Chem. Soc. Rev.* **42**, 7244–7256 (2013).
19. Sodhi, J. S. & Rao, I. J. Modeling the mechanics of light activated shape memory polymers. *Int. J. Eng. Sci.* **48**, 1576–1589 (2010).
20. Ryu, J. *et al.* Photo-origami—Bending and folding polymers with light. *Appl. Phys. Lett.* **100**, 161908/1-5 (2012).
21. Jiang, W. *et al.* Photoresponsive Soft-Robotic Platform: Biomimetic Fabrication and Remote Actuation. *Adv. Funct. Mater.* 7598-7604 (2014).
22. Jiang, H. Y., Kelch, S. & Lendlein, A. Polymers Move in Response to Light. *Adv. Mater.* **18**, 1471–1475 (2006).
23. Zhang, H. & Zhao, Y. Polymers with Dual Light-Triggered Functions of Shape Memory and Healing Using Gold Nanoparticles. *ACS Appl. Mater. Interfaces* **5**, 13069–13075 (2013).
24. Liu, Y., Boyles, J. K., Genzer, J. & Dickey, M. D. Self-folding of polymer sheets using local light absorption. *Soft Matter* **8**, 1764–1769 (2012).
25. Gracias, D. H. Stimuli responsive self-folding using thin polymer films. *Curr. Opin. Chem. Eng.* **2**, 112–119 (2013).
26. Chatani, S., Kloxin, C. J. & Bowman, C. N. The power of light in polymer science: photochemical processes to manipulate polymer formation, structure, and properties. *Polym. Chem.* **5**, 2187–2201 (2014).
27. Meng, H. *et al.* Various shape memory effects of stimuli-responsive shape memory polymers. *Smart Mater. Struct.* **22**, 093001/1-23 (2013).

28. Lucas, T. M. *et al.* Wavelength specific excitation of gold nanoparticle thin-films. *Appl. Phys. Lett.* **104**, 11909 (2014).
29. Na, J.-H. *et al.* Programming Reversibly Self-Folding Origami with Micropatterned Photo-Crosslinkable Polymer Trilayers. *Adv. Mater.* **27**, 79–85 (2015).
30. Nguyen, T. D., Jerry Qi, H., Castro, F. & Long, K. N. A thermoviscoelastic model for amorphous shape memory polymers: incorporating structural and stress relaxation. *J. Mech. Phys. Solids* **56**, 2792–2814 (2008).
31. Stroganov, V. *et al.* Biodegradable Self-Folding Polymer Films with Controlled Thermo-Triggered Folding. *Adv. Funct. Mater.* **24**, 4357–4363 (2014).
32. Qi, H. J., Nguyen, T. D., Castro, F., Yakacki, C. M. & Shandas, R. Finite deformation thermo-mechanical behavior of thermally induced shape memory polymers. *J. Mech. Phys. Solids* **56**, 1730–1751 (2008).
33. Diani, J., Liu, Y. & Gall, K. Finite strain 3D thermoviscoelastic constitutive model for shape memory polymers. *Polym. Eng. Sci.* **46**, 486–492 (2006).
34. Diani, J., Gilormini, P., Frédy, C. & Rousseau, I. Predicting thermal shape memory of crosslinked polymer networks from linear viscoelasticity. *Int. J. Solids Struct.* **49**, 793–799 (2012).
35. Xu, B. *et al.* Thermo-mechanical properties of polystyrene-based shape memory nanocomposites. *J. Mater. Chem.* **20**, 3442 (2010).
36. Tamagawa, H. Thermo-responsive two-way shape changeable polymeric laminate. *Mater. Lett.* **64**, 749–751 (2010).
37. Hawkes, E. *et al.* Programmable matter by folding. *Proc. Natl. Acad. Sci.* 12441-12445 (2010).
38. White, T. J. *et al.* A high frequency photodriven polymer oscillator. *Soft Matter* **4**, 1796–1798 (2008).
39. Liu, Y., Miskiewicz, M., Escuti, M. J., Genzer, J. & Dickey, M. D. Three-dimensional folding of pre-strained polymer sheets via absorption of laser light. *J. Appl. Phys.* **115**, (2014).
40. Small, W., Wilson, T. S., Bennett, W. J., Loge, J. M. & Maitland, D. J. Laser-activated shape memory polymer intravascular thrombectomy device. *Opt Express* **13**, 8204–8213 (2005).
41. Piqué, A., Mathews, S. A., Charipar, N. A. & Birnbaum, A. J. Laser origami: a new technique for assembling 3D microstructures. in (eds. Bachmann, F. G. *et al.*) (2012).

42. Laflin, K. E., Morris, C. J., Mugeem, T. & Gracias, D. H. Laser triggered sequential folding of microstructures. *Appl. Phys. Lett.* **101**, 131901/1-4 (2012).
43. Alberto Piqué, S. A. M. Laser Origami: a New Technique for Assembling 3D Microstructures. *SPIE Proc. Vol 8244* (2012).
44. de Haan, L. T. *et al.* Accordion-like Actuators of Multiple 3D Patterned Liquid Crystal Polymer Films. *Adv. Funct. Mater.* **24**, 1251–1258 (2014).
45. Kim, J., Hanna, J. A., Byun, M., Santangelo, C. D. & Hayward, R. C. Designing Responsive Buckled Surfaces by Halftone Gel Lithography. *Science* **335**, 1201–1205 (2012).
46. Guan, J. J., He, H. Y., Hansford, D. J. & Lee, L. J. Self-folding of three-dimensional hydrogel microstructures. *J Phys Chem B* **109**, 23134–23137 (2005).
47. Stoychev, G., Zakharchenko, S., Turcaud, S., Dunlop, J. W. C. & Ionov, L. Shape-Programmed Folding of Stimuli-Responsive Polymer Bilayers. *ACS Nano* **6**, 3925–3934 (2012).
48. Chen, D., Yoon, J., Chandra, D., Crosby, A. J. & Hayward, R. C. Stimuli-responsive buckling mechanics of polymer films. *J. Polym. Sci. Part B Polym. Phys.* **52**, 1441–1461 (2014).
49. Velankar, S. S., Lai, V. & Vaia, R. A. Swelling-Induced Delamination Causes Folding of Surface-Tethered Polymer Gels. *ACS Appl. Mater. Interfaces* **4**, 24–29 (2012).
50. Kim, J., Hanna, J. A., Hayward, R. C. & Santangelo, C. D. Thermally responsive rolling of thin gel strips with discrete variations in swelling. *Soft Matter* **8**, 2375–2381 (2012).
51. Hsu, Y.-J., Jia, Z. & Kymissis, I. A Locally Amplified Strain Sensor Based on a Piezoelectric Polymer and Organic Field-Effect Transistors. *IEEE Trans. Electron Devices* **58**, 910–917 (2011).
52. Tanaka, T., Nishio, I., Sun, S.-T. & Ueno-Nishio, S. Collapse of Gels in an Electric Field. *Science* **218**, 467–469 (1982).
53. Stellman, P., Buchner, T., Arora, W. J. & Barbastathis, G. Dynamics of nanostructured Origami. *J. Microelectromechanical Syst.* **16**, 932–949 (2007).
54. Biggs, J. *et al.* Electroactive Polymers: Developments of and Perspectives for Dielectric Elastomers. *Angew. Chem. Int. Ed.* **52**, 9409–9421 (2013).

55. van den Ende, D., Kamminga, J.-D., Boersma, A., Andritsch, T. & Steeneken, P. G. Voltage-Controlled Surface Wrinkling of Elastomeric Coatings. *Adv. Mater.* **25**, 3438–3442 (2013).
56. McGough, K., Ahmed, S., Frecker, M. & Ounaies, Z. Finite element analysis and validation of dielectric elastomer actuators used for active origami - Abstract - Smart Materials and Structures - IOPscience. (2014).
57. Felton, S. M. *et al.* Self-folding with shape memory composites. *Soft Matter* **9**, 7688–7694 (2013).
58. In, H. J., Lee, H., Nichol, A. J., Kim, S. G. & Barbastathis, G. Carbon nanotube-based magnetic actuation of origami membranes. *J. Vac. Sci. Technol. B* **26**, 2509–2512 (2008).
59. Yi, Y. W. & Liu, C. Magnetic actuation of hinged microstructures. *J. Microelectromechanical Syst.* **8**, 10–17 (1999).
60. Judy, J. W. & Muller, R. S. Magnetically actuated, addressable microstructures. *J. Microelectromechanical Syst.* **6**, 249–256 (1997).
61. Nguyen, V. Q., Ahmed, A. S. & Ramanujan, R. V. Morphing Soft Magnetic Composites. *Adv. Mater.* **24**, 4041–4054 (2012).
62. Martinez, R. V., Fish, C. R., Chen, X. & Whitesides, G. M. Elastomeric Origami: Programmable Paper-Elastomer Composites as Pneumatic Actuators. *Adv. Funct. Mater.* 1376-1384 (2012).
63. Kwok, S. W. *et al.* Magnetic Assembly of Soft Robots with Hard Components. *Adv. Funct. Mater.* 2180-2187 (2013).
64. Zheng, L., Yoshida, S., Morimoto, Y., Onoe, H. & Takeuchi, S. Pneumatic balloon actuator with tunable bending points. in *2015 28th IEEE International Conference on Micro Electro Mechanical Systems (MEMS)* (2015).
65. Liu, Y., Genzer, J. & Dickey, M. D. 2D or not 2D: Shape Programming of Polymer Sheets. *Prog. Polym. Sci.* (2015). doi:10.1016/j.progpolymsci.2015.09.001
66. Krishna, K. V. G. A method of determining the dipole moment and relaxation time from microwave measurements. *Trans. Faraday Soc.* **53**, 767–770 (1957).
67. Gabriel, C. *et al.* Dielectric parameters relevant to microwave dielectric heating. *Chem. Soc. Rev.* **27**, 213–224 (1998).

68. Das, C. K., Bhattacharya, P. & Kalra, S. S. Graphene and MWCNT: Potential Candidate for Microwave Absorbing Materials. *J. Mater. Sci. Res.* **1**, (2012).
69. Nüchter, M., Ondruschka, B., Bonrath, W. & Gum, A. Microwave assisted synthesis – a critical technology overview. *Green Chem.* **6**, 128–141 (2004).
70. Dakin, T. W. & Works, C. N. Microwave Dielectric Measurements. *J. Appl. Phys.* **18**, 789–796 (1947).
71. Hu, H., Zhao, Z., Zhou, Q., Gogotsi, Y. & Qiu, J. The role of microwave absorption on formation of graphene from graphite oxide. *Carbon* **50**, 3267–3273 (2012).
72. Gokirmak, A., Wu, D.-H., Bridgewater, J. S. A. & Anlage, S. M. A Scanned Perturbation Technique For Imaging Electromagnetic Standing Wave Patterns of Microwave Cavities. *Rev. Sci. Instrum.* **69**, 3410 (1998).
73. Mailen, R. W., Liu, Y., Dickey, M. D., Zikry, M. & Genzer, J. Modelling of shape memory polymer sheets that self-fold in response to localized heating. *Soft Matter* (2015). doi:10.1039/C5SM01681A

CHAPTER 3

Self-folding of Thick Polymer Sheets Using Gradients of Heat*

*This chapter is based on Davis, D., Chen, B., Dickey, M. D. & Genzer, J. Self-folding of Thick Polymer Sheets Using Gradients of Heat. *J. Mech. Robot.* **8**(3), 031014 (2015).

Overview

Self-folding converts two-dimensional (2D) sheets into three-dimensional (3D) objects in a hands-free manner. This chapter demonstrates a simple approach to self-fold commercially available, millimeter-thick thermoplastic polymer sheets. The process begins by first stretching poly(methyl methacrylate) (PMMA), polystyrene (PS), or polycarbonate (PC) sheets using an extensometer at elevated temperatures close to the glass transition temperature (T_g) of each sheet. Localizing the strain to a small strip creates a “hinge,” which folds in response to asymmetric heating of the sheet. Although there are a number of ways to supply heat, here a heat gun delivers heat to one side of the hinge to create the necessary temperature gradient through the polymer sheet. When the local temperature exceeds the T_g of the polymer, the strain in the hinged region relaxes. Because strain relaxation occurs gradually across the sheet thickness, the polymer sheet folds in the direction towards the heating source. A simple geometric model predicts the dihedral angle of the sheet based on the thickness of the sheet and width of the hinge. This chapter reports an approach to folding that works for a variety of thermoplastics using sheets that are significantly thicker (~10 times) than those reported previously.

3.1 Introduction

Self-folding strategies convert 2D sheets into 3D objects in a hands-free manner. Self-folding is attractive for a number of applications, including remote deployment of compact structures¹⁻⁴, assembly⁵, packaging^{6,7}, robotics⁸, mechanical metamaterials⁹, and mechanical actuation¹⁰. While there are many strategies for programming materials to fold in response to a stimulus (e.g., heat, pH, light)¹¹⁻⁴⁵, this chapter focuses on polymeric materials that self-fold in response to external heat.

Recently, our group demonstrated a simple approach to self-folding that uses localized heating of prestrained polystyrene sheets to induce folding^{12,46}. Heating these “shrink films” uniformly (*e.g.*, in an oven) above the glass transition temperature (T_g) of the polymer causes them to contract in-plane uniformly. In contrast, delivering the heat from one side of the sheet generates a temperature gradient through the thickness of the sheet. This asymmetric heating causes the surface of the polymer sheet to heat faster than the bottom of the sheet and therefore shrink faster, forcing the sheet to curl toward the heat source. It is possible to harness this principle for self-folding by localizing the heat to a thin strip on the surface of the shrink film and thereby localize the shrinkage to achieve a “hinging” response. The heat may be delivered locally using, for example, ink that selectively absorbs light¹², microwaves⁴⁶, patterned lasers⁴⁷, or Joule heating⁴⁸.

This localized heating method works well with commercially available shrink films (*e.g.*, Shrinky Dinks). While these materials are convenient, they are manufactured in a limited range of thicknesses ($\sim 300\ \mu\text{m}$), compositions (*e.g.*, polystyrene, polyethylene, polyesters), and strains ($\sim 55\%$ Swainger strain in our previous work)^{12,47,49}. Previously, we developed a simple geometric model to predict the folding angle as a function of prestrain, sample thickness, and hinge width (the region of the sheet designed to shrink)⁴⁹. While the model predicts accurately the folding angle of the sheet (*i.e.*, the angle between two adjacent faces, α_F), we could only vary the hinge width to verify the validity of the model since the commercial manufacturing process employed produces polymer sheets with constant thickness, chemical composition, and degree of prestrain.

Here, we seek to vary the thickness, chemical composition, and amount of prestrain of polymer sheets to explore if the geometric model accurately predicts α_F across the entire parameter space defined within the model. The experiments have the added benefit of folding thicker plastics (1-3 mm thick), which are significantly stiffer than previously studied thin films.

These thicker polymer sheets enable a wide range of applications for folding due to their strength and robustness.

Performing these experiments motivated a new approach to induce self-folding. Rather than prestraining the entire film – as done commercially – we prestrained only the hinged region. Since the prestrain programming confines the shrinkage to only the hinged region, stray heat delivered outside the hinged regions does not cause notable curling or shrinkage. Thus, this method enables global heating instead of local heating. In this work, we use a heat gun (similar to a hair dryer) to heat the surface of the sheet; but in principle, any heating source that is capable of delivering sufficient heat to the sheet (increasing the temperature of the sheet above the T_g) would work.

Prestrained polymers that shrink to a pre-defined shape above the T_g belong to the category of shape memory polymers (SMPs). The polymer sheets here are effectively SMPs that shrink in-plane if heated uniformly but fold if heated non-uniformly. Thus, the method here provides a means of converting in-plane strain into out of plane folding using a simple stimulus (a heat gun in this example). We explore this process systematically for folding sheets of PMMA, PS, and PC at the same thickness (2 mm) and PMMA at three different thicknesses (1.5, 2, and 3 mm). We also characterize the thermal behavior during heating and folding and verify that with some minor modifications the simple geometric model introduced earlier predicts the behavior over the entire parameter space.

We developed a method that involves a cycle of prestraining of polymer sheets, self-folding via selective heating, and unfolding via uniform heating, as shown in **Figure 3.1a**. **Figure 3.1b** illustrates how an extensometer applies localized strain to the sheet at elevated temperatures (close to but below T_g). After prestraining the samples, we grip one end of the sample and orient the sample horizontally in free space at room temperature. A heat gun, positioned at 11.4 cm from the upper surface of the sheet, delivers hot air ($T \sim 150^\circ\text{C}$) toward the polymer sheet surface until the sample stops folding or reaches 90° . During the folding

process, an IR camera and a video camera record the temperature of the surface of the polymer and the folding angle of the polymer, respectively. As demonstrated by temperature profiles plotted in **Figure S3.2** in the SI, the temperature on the surface of the sheet is approximately the same for all samples during heating. As will be demonstrated later in the chapter, the polymer sheet starts to fold as soon as the surface temperature of the sheet reaches $\sim T_g$ (**Figure 3.1c**). It is possible to heat the samples in an oven above T_g to return the sample back to its original shape.

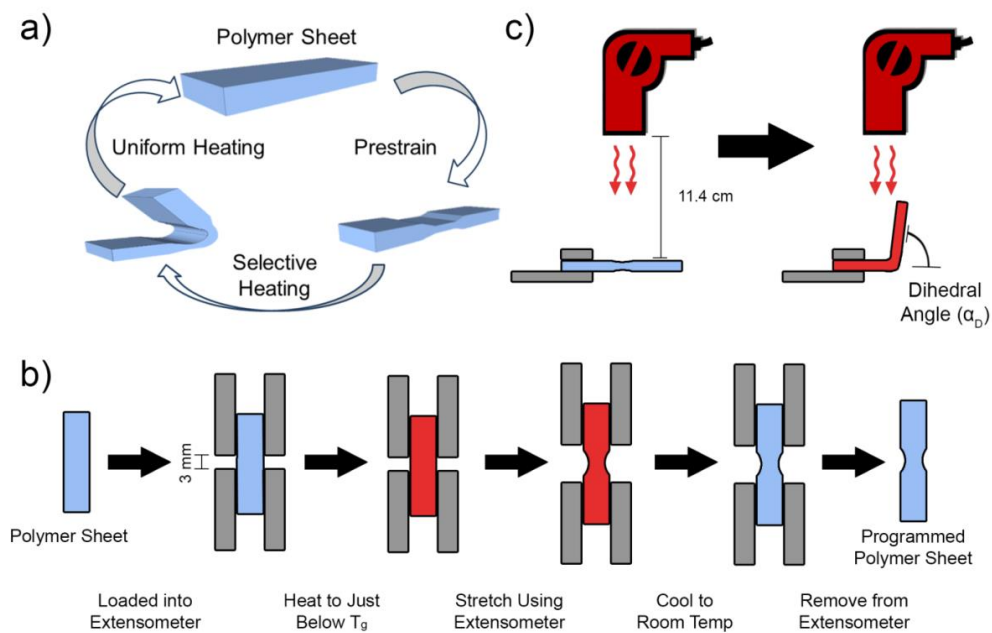


Figure 3.1. Process for self-folding. a) Locally prestraining a polymer sheet creates a hinge. Selective heating of one side of the ‘hinge’ causes asymmetric strain relaxation that induces folding. When applied uniformly, heat causes unfolding and the sample reverts to the original shape. The full cycle causes some permanent deformation, but the focus here is on the folding step. b) Schematic of the preparation steps using an extensometer. A picture of the setup is in **Figure S3.1** the SI. c) A heat gun asymmetrically heats one side of the prestrained polymer sheet to induce self-folding.

3.2 Geometric Model

Previously, we used geometric principles to derive Equation 3.1^{18,49}, which predicts accurately the dihedral angle (α_D , defined as $\alpha_D = 180^\circ - \alpha_F$) of self-folding prestrained polymer sheets using the hinge width (W), the film thickness (H), and the shrinkage (S , equivalent to the Swainger strain, defined in the SI) of the sheet:

$$\alpha_D = 180^\circ - 2 \cdot \tan^{-1} \left(\frac{2H}{W \cdot S} \right) \quad (3.1)$$

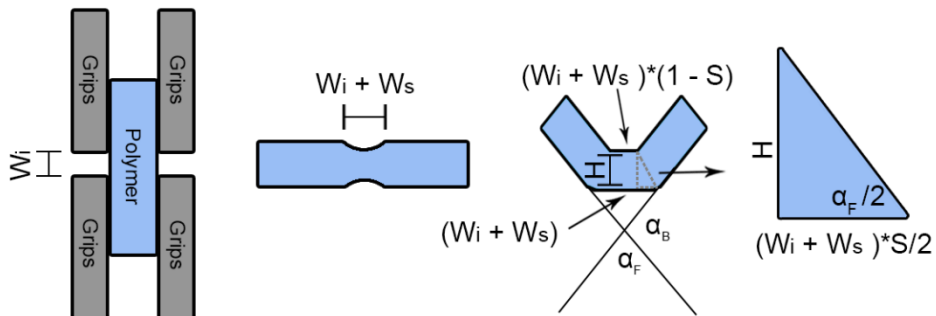


Figure 3.2. A geometric model predicts the folding angle α_F of commercial prestrained sheets⁴⁹. Grips from an extensometer start at a distance W_i apart and strain the sample a distance W_s . The straining causes the sample to shrink in the hinged region. Heat delivered to the top of the sample causes the top of the sample to shrink and therefore the sample folds. In our system, $W = (W_i + W_s)$.

This model assumes that: 1) The polymer directly underneath the hinge shrinks; 2) The bottom of the polymer sheet does not shrink considerably; 3) The strain relaxes linearly across the polymer sheet thickness (H); and 4) The thickness of the film does not increase considerably with shrinkage (although this assumption is not correct, the model still performs

adequately). When using this model with commercially available prestrained polystyrene sheets, the value for H is ~300 μm and S is ~55%, so that W is the only variable^{18,49}.

We found that the experimental data at larger strains can be modeled more accurately by employing the Almansi strain instead of the Swainger strain (used as S in the definition of Equation 3.1). In the SI, we provide the description of various strain models, including Swainger, Almansi, as well as Cauchy and Green⁵⁰. We also offer more details about why we chose the Almansi strain to model the data (*cf.* **Figure S3.3** in the SI). Although the Almansi strain employed in conjunction with Equation 1 fits the experimental data well, it does not describe the strain recovery in our samples. For example, samples extended from 3 mm (W_i) to 8 mm (W_i+W_s) and exposed to uniform heat recovered back to ~3 mm (~100% recovery).

As shown in **Figure 3.2**, the grips of the extensometer extend only the middle of the sample. Because of this localization, the rest of the material does not change its shape when heated. The extension ratio (λ), defined as the ratio of the final extended length (W_s+W_i) to the initial length (W_i), relates to the strain in the sample (S). The Almansi strain is related to S by the expression given in Equation 3.2:

$$S = \frac{1}{2} \left(\frac{(W_s + W_i)^2 - (W_i)^2}{(W_s + W_i)^2} \right) = \frac{1}{2} (1 - \lambda^{-2}) \quad (3.2)$$

Substituting this expression into Equation 3.1 results in Equation 3.3:

$$\alpha_D = 180^\circ - 2 \cdot \tan^{-1} \left(\frac{4H(W_s + W_i)}{(W_s + W_i)^2 - (W_i)^2} \right) = 180^\circ - 2 \cdot \tan^{-1} \left(\frac{4H}{(W_s + W_i)(1 - \lambda^{-2})} \right) \quad (3.3)$$

3.3 Self-Folding in Asymmetric Heat

In our experiments, we varied the sheet thickness, shrinkage, and material type and compared the experimental α_D to that predicted by the geometric model (Equation 3.3). Because the geometric model contains no material-specific parameters, we studied thermoplastic sheets

made of PMMA, PS, and PC (purchased from McMaster Carr, Elmhurst, IL) to test the validity of the geometric model. Specifically, we studied PMMA sheets of various thicknesses (1.5, 2.0, 3.0, 6.0, and 12.0 mm) and PS and PC sheets that were 2 mm thick. We verified the thickness of each sheet with a caliper. We cut the sheets with a laser cutter into rectangles (25 mm by 75 mm), placed it into an extensometer (Instron) with the distance between the grips of 3 mm (W_i) and extended by a distance W_s (cf. **Figure 3.1b**). We then use a heat gun to fold the sheets, as described earlier. Only results from samples whose thickness is ≤ 3.0 mm are reported here. We do not show the results of folding polymer sheets thicker than 3 mm due to large scatter in the data (likely due to a combination of temperature profile and variation of strain in the sample).

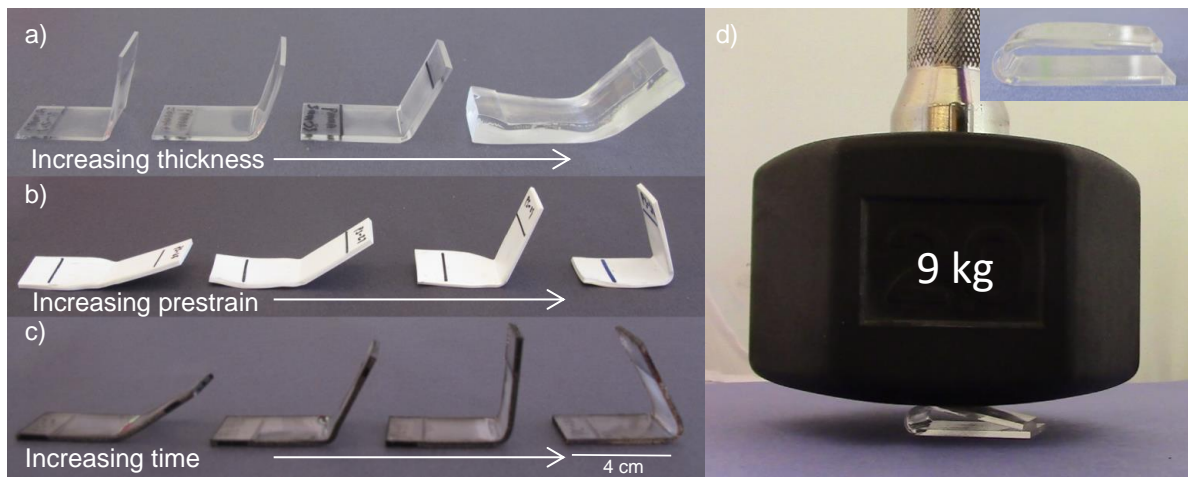


Figure 3.3. Photographs of self-folding samples. a) PMMA samples with thickness ranging from 1.5 to 12 mm. b) PS samples with λ from 1.33 to 2.67. c) PC samples exposed to the heat gun for 30 to 45 s. d) A PMMA sample folded to $\alpha_D \sim 180^\circ$ that is supporting a 9 kg weight demonstrates the strength of the folded samples.

Figure 3.3 shows folded samples of PMMA (**Figure 3.3a**), PS (**Figure 3.3b**), and PC (**Figure 3.3c**). **Figure 3.3** also highlights the effect of thickness (**Figure 3.3a**), strain (**Figure 3.3b**), and folding time (**Figure 3.3c**). In **Figures 3.3a** and **3.3b**, we heated the samples until they either stopped folding or reached 90° to avoid heating the backside of the sample. It is, however, possible to fold the sheets up to $\alpha_D \sim 180^\circ$ by moving the heat gun during folding, as shown in **Figure 3.3d**. These materials are stiff; **Figure 3.3d** shows a sample bearing a 9 kg weight.

We explored the relationship between extension ratio (λ) and dihedral angle (α_D) found in Equation 3.3 by systematically varying the prestrain, material type, and in the case of PMMA, the thickness. **Figure 3.4a** reports the data for PMMA as a function of λ and sheet thickness. From this data, it is clear that samples with larger λ bend to larger α_D . Likewise, thinner samples bend to larger α_D than thicker samples for otherwise identical conditions. A similar relationship between λ and α_D exists for all polymeric materials studied, as shown in **Figure 3.4b**.

Figures 3.4a and **3.4b** represent a range of variables, which can be collapsed onto a master plot, when properly normalized as shown in **Figure 3.4c**, which plots the arctan component of Equation 3.3 versus α_D . The line on the plot labeled 'model prediction' shows the theoretical prediction from Equation 3.3. The model captures the trends well across a range of prestrains, thicknesses, and materials. The biggest departures from the model occur at $\alpha_D < 20^\circ$ presumably because the Almansi strain is designed to predict the strain primarily in samples with high λ . For $\alpha_D > 90^\circ$, the samples block the heating source and thus inhibit proper heating of the upper hinged region of the sheet. This prevents us from exploring samples that fold past $\alpha_D = 90^\circ$ with our current setup.

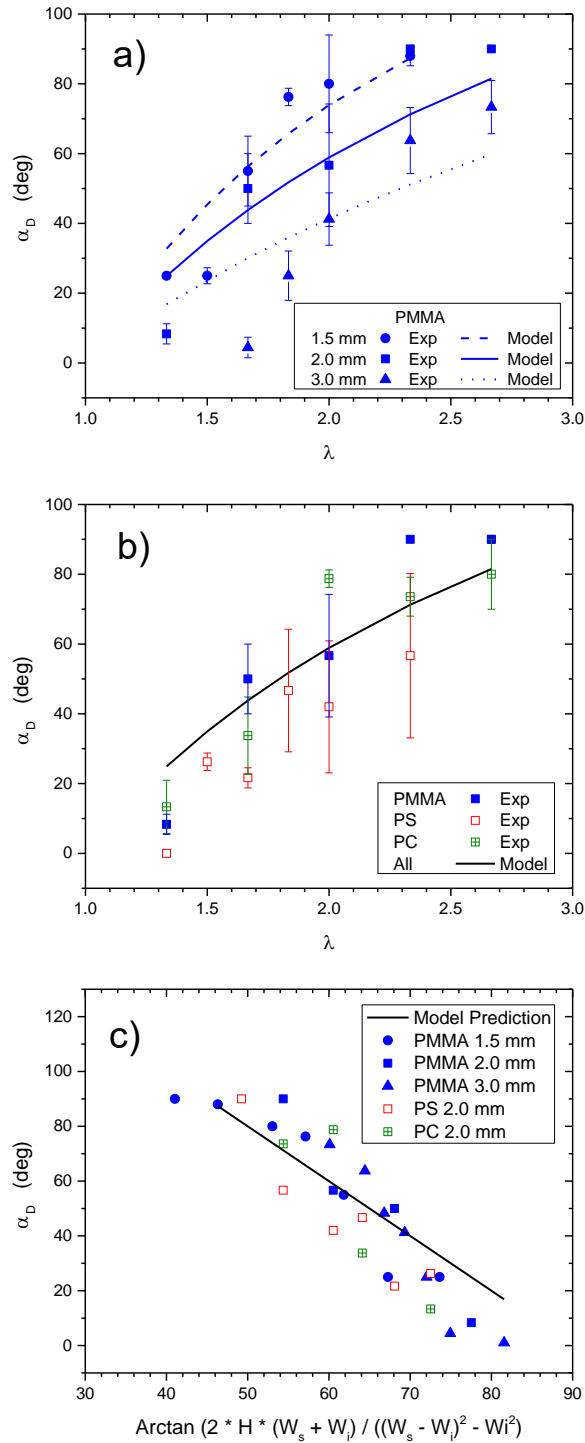


Figure 3.4. a) Experimental data (symbols) and geometric model predictions (lines) of α_D vs λ for varying thicknesses of PMMA. b) Experimental data (symbols) and geometric model predictions (line) of α_D vs λ for 2.0 mm thick PMMA, PS, and PC. c) Data from **Figures 3.4a** and **3.4b** plotted as a function of the arctan function from the geometric model. The black line denotes prediction from Equation 3.3.

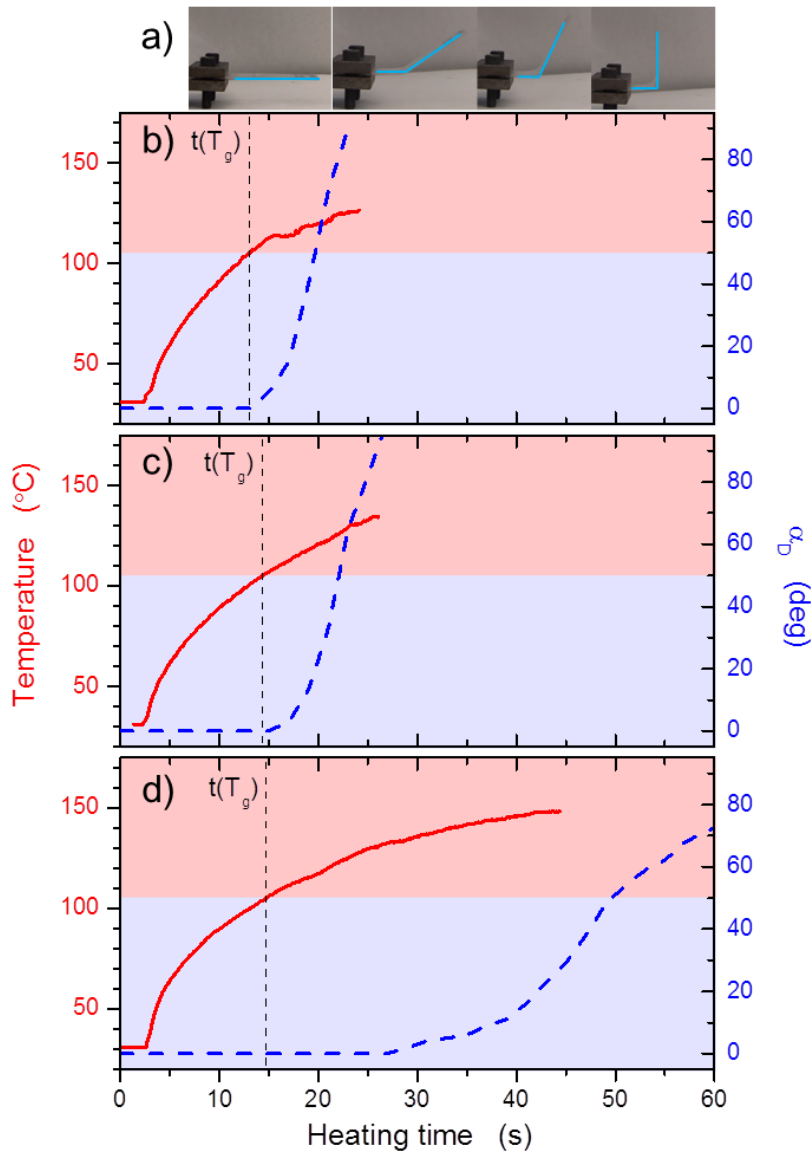


Figure 3.5. Temperature (red-solid line, left ordinate) and dihedral angle (blue-dashed line, right ordinate) as a function of heating time overlaid with the surface temperature profile of the same sample. The PMMA starts folding after the surface exceeds T_g (~ 105 °C) for 1.5 mm (b), 2.0 mm (c) and 3.0 mm (d) thick samples. Samples of PMMA that are 3.0 mm thick start folding after the surface reaches T_g .

Figure 3.5a shows a sequence of images from a self-folding experiment. The same figure also plots the temperature profiles of the hinged region (left ordinate) and α_D (right ordinate) as a function of heating time for PMMA sheets ranging from 1.5 to 3 mm in thickness.

From this overlay, it appears that the onset of folding occurs after the surface of the sheet exceeds T_g for PMMA. At the onset of folding, T_g is slightly higher for thinner materials and much higher for thicker materials. The same data for the PS and PC sheets are provided in **Figure S3.4** in the SI.

3.4 Thermal Model

In our previous work we established that in some systems, the sample folds as soon as the temperature on the back side of the sheet reaches T_g ^{47,49,51}, but for other systems, the sample folds before the back side reaches T_g ⁴⁶. The onset folding time is defined as the instant when $\alpha_D > 0$. From the data in **Figure 3.5b** and **3.5c**, it appears that folding occurs after the surface of the upper face of the sheet (*i.e.*, the one facing the heat gun) reaches T_g of PMMA. We observed the similar behavior for PS and PC sheets with thicknesses of 2 mm (*cf.* **Figure S3.4** in the SI). The onset time for PMMA sheets whose thickness is 3 mm occurs longer after the surface reaches T_g than the other sheets tested. To comprehend this behavior we constructed a simple heat transport model to provide insight about temperature distribution inside the sheet as a function of heating time.

The model (see SI for more details) assumes that the temperature on the surface of the sheet facing the heat gun corresponds to the temperature measured by the IR camera. The backside of the sheet (*i.e.*, away from the heat gun) is modeled as adiabatic; *i.e.*, we assume no heat loss from this side of the sample to the surrounding.

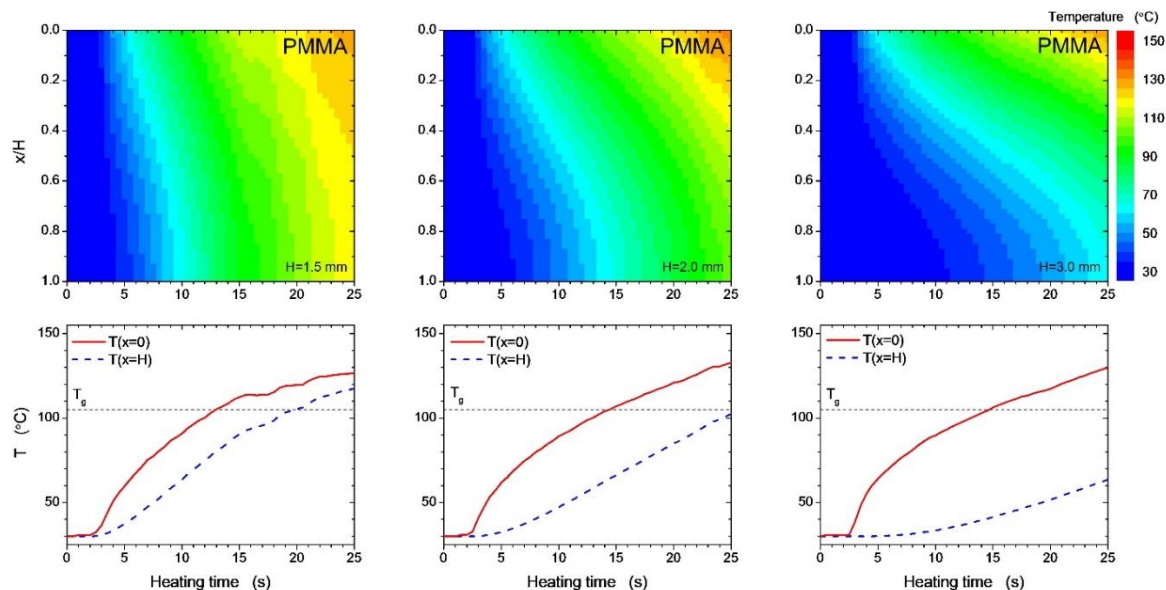


Figure 3.6. The top of each pair show the model's prediction of temperature profiles inside the sheets: PMMA 1.5 mm (left), PMMA 2.0 mm (middle), and PMMA 3.0 mm (right). The bottom of each pair denotes the temporal evolution of the temperature on the front side (red line) and the backside (blue line) of the sample.

The resulting temperature profiles calculated from the model for PMMA are plotted in **Figure 3.6**. The temperature profiles for PS and PC are plotted in **Figure S3.5** in the SI. From the data in **Figure 3.6**, the temperature on the backside of the sheet reaches the corresponding T_g at longer times than the temperature on the front face of the polymer sheet, as expected. The difference in time is relatively small for 1.5 mm thick PMMA (~8 s) and increases when the thickness of the sheet increases. For instance, for 2 mm thick sheets the delay times are ~11 and 10 s for PMMA and PS (*cf.* **Figure S3.5** in the SI), respectively. For the remaining thicker sheets, the time difference between the front and backside of the sheet reaching the T_g is even larger. We acknowledge that this model may not correctly capture of the experimental situation due to the following three reasons. 1) The model ignores possible heating of the backside of the samples through heat that is emitted by the heat gun. 2) The model assumes a constant thickness of the sheet, taken as the sheet nominal value, H . 3)

The backside of the sheet may not have to reach T_g for folding to begin. Nevertheless, the trends in temperature profiles offered by the model provide consistent, albeit qualitative, information about the temperature distribution inside the sheet during the heating process.

Table 3.1. Folding attributes of tested materials

Sample	Onset folding time (s)	Temperature at onset of folding (°C)	T_g (°C)
PMMA 1.5 mm	10	106	105 (ref ⁵²)
PMMA 2.0 mm	12	107	105 (ref ⁵²)
PMMA 3.0 mm	24	127	105 (ref ⁵²)
PS 2.0 mm	10	105	103 (ref ¹²)
PC 2.0 mm	24	150 ⁺	147 (ref ⁵²)

⁺We cannot measure past 150 °C with the IR camera; the temperature for PC might be higher

The data in **Table 3.1** compare the onset time of folding (*i.e.*, the time at which the polymer sheet starts to fold), the surface temperature at the onset of folding, and the T_g of the materials. As thickness and T_g increase, the surface temperature at the onset of folding and onset folding time also increase.

We were also able to fold polyethylene terephthalate (PET), polylactic acid (PLA), and poly(p-phenylene oxide) (PPO) but not with the same consistency as PMMA, PS, and PC sheets. We hypothesize that PET and PLA might fold using a heating method other than the heat gun. The velocity of the air leaving the heat gun generates enough force to prevent PLA and PET from folding. PPO is difficult to process using the extensometer. PPO also has a high T_g (~215°C) and the heat gun does not generate enough heat to cause consistent folding.

3.5 Conclusion

We successfully programmed and folded three different thermoplastic sheets (PMMA, PS, and PC all 2 mm thick) as well as PMMA sheets with a range of thicknesses (ranging from 1.5 to 12 mm). The sheet folding occurs by prestraining local regions of the polymer sheets and then heating them asymmetrically by applying heat from a heat gun to one side of the sheet. The dihedral angle of the sheet heated with a heat gun can be described by a simple geometrical model for a range of thicknesses, extension ratios, and degree of prestrain all for polymeric materials studied. We used the Almansi strain rather than the Swainger strain to match the experimental data to the geometric model. We characterized the folding behavior in terms of the thickness, strain, material type, folding speed, and temperature behavior of the hinge. We also provided a simple model of the heat flow through the thickness of the sheet.

Although this work uses a heat gun to fold the polymer sheets, other heating methods should also work as long as they deliver heat asymmetrically to the surface of the hinge. Future work could switch to a more direct heating method to eliminate the limitations of using a heat gun (the air pushes the sample down and the position of the gun limits the maximum dihedral angle). While the work here verifies the geometrical model for folds up to 90°, it would be interesting to verify whether the samples can be folded consistently to larger dihedral angles. Future work could examine programming bi-axial strain or creating samples with multiple hinged regions. This work provides a step towards enabling the self-folding of thick thermoplastic polymer sheets.

3.6 Acknowledgements

We thank the National Science Foundation for supporting this work under the NSF EFRI program (Grant No. 1240438).

Supporting Information

Heating chamber in extensometer

Figure S3.1 displays the custom-built heating chamber attached to the extensometer. The sample is held between two vertical grips (the initial distance between the two grips, W_i , is 3 mm). After increasing the temperature inside the chamber close to the T_g , the sample is stretched uniaxially (vertical direction in our set up) by a distance W_s .



Figure S3.1. Experimental setup for programming strain in polymer sheets in an extensometer. There are two metal grips in the center of the oven that pull the sample vertically while the four infrared lamps control the temperature with an error of $\pm 1^\circ\text{C}$. The metal grips each have two screws that secure the sample.

Measuring the temperature on the surface of the sheet

Figure S3.2 plots typical temperature profiles of the surface of the polymer sheet during the heating process, as measured by an infrared (IR) camera. As evident from the data, the increase in the surface temperature of the sheet with increasing time is approximately the same for all materials and all sheet thicknesses.

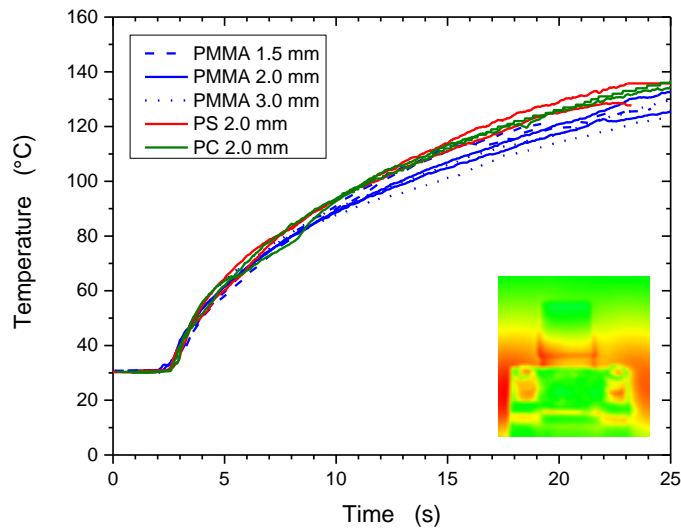


Figure S3.2. Temperature profiles of the hinge region of PS, PC, and PMMA (all thicknesses) as a function of time. We use an infrared camera to measure the temperature of the hinge while the material folds. The heat gun starts heating the sample at time = ~2 seconds.

Finite strain modelling

To understand the relationship between the various strains, we first introduce the extension ratio (λ), as the proportion of the length of the strained region (L) to its original length (L_0) as shown in Equation S3.1:

$$\lambda = \frac{L}{L_0} \tag{S3.1}$$

We consider four different definitions of strain, including, the Cauchy (Equation S3.2), Swainger (Equation S3.3), Green (Equation S3.4), and Almansi strain models (Equation S3.5). These strains can be broken up into two pairs. The Cauchy and the Swainger strains are linear models that work best for small strains, little deformation, and no rigid body rotation⁵⁰. The Cauchy and the Swainger strains are designed for elongation and shrinkage respectively. In our prior work, the geometric model used the Swainger strain as the shrinkage term (S).

The Green and the Almansi strains are quadric strains that describe elongation and shrinkage, respectively. This means that both the Green and the Cauchy strains are used for elongation and both the Swainger and the Almansi strains are used in shrinkage (*i.e.*, the Swainger and Almansi strains utilize the elongated length, L, in the denominator). In both the Green and the Almansi strains, the quadratic term corrects for larger sample deformations and rigid body rotations⁵⁰.

$$\varepsilon_C = \frac{L - L_0}{L_0} = \lambda - 1 \quad (S3.2)$$

$$\varepsilon_S = \frac{L - L_0}{L} = 1 - \lambda^{-1} \quad (S3.3)$$

$$\varepsilon_G = \frac{L^2 - (L_0)^2}{2(L_0)^2} = \frac{\lambda^2 - 1}{2} \quad (S3.4)$$

$$\varepsilon_A = \frac{(L_0)^2 - L^2}{2L^2} = \frac{1 - \lambda^2}{2} \quad (S3.5)$$

In Equations S3.2 – S3.5, ε_C is the Cauchy strain, ε_S is the Swainger strain, ε_G is the Green strain, and ε_A is the Almansi strain. Since the Almansi and Swainger strains describe shrinkage, they can be substituted into Equation 3.1 as the shrinkage (S) term directly and change which type of materials the model accurately describes. The Swainger strain is less accurate in our situation because our samples are more extended than the samples utilized

in our prior work^{49,53}. **Figure S3.3** shows the experimental dihedral angles (α_D) measured in PMMA sheets plotted against the geometric model from Equation 3.1. In these plots, the geometric model uses the Swainger and Almansi strains as the shrinkage term S (*cf.* Equation 3.1).

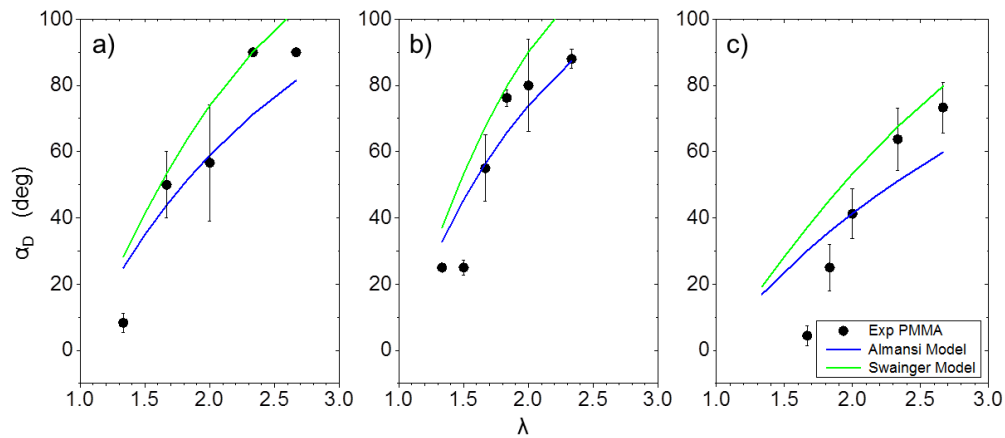


Figure S3.3. Dihedral angles calculated using the Almansi (blue lines) and Swainger (green lines) strains as a function of extension ratio (λ) using the model given by Equation 3.1 in the main text. The symbols represent the experimental data collected from PMMA sheets with thicknesses 1.5 mm (a), 2.0 mm (b) and 3.0 mm (c).

Figure S3.4 displays surface temperature (red-solid line, left ordinate) and dihedral angle (blue-dashed line, right ordinate) for PS (top) and PC (bottom) sheets as a function of heating time. Corresponding data for PMMA sheets of three different sheet thicknesses are plotted in **Figure 3.5** in the main text.

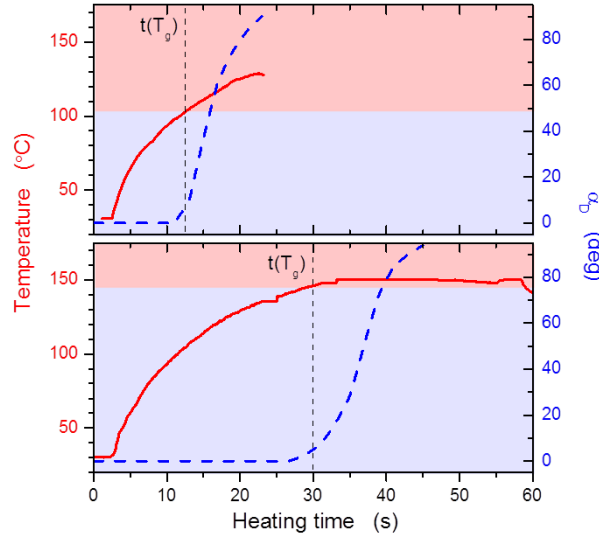


Figure S3.4. Temperature (red-solid line, left ordinate) and the dihedral angle (blue-dashed line, right ordinate) as a function of time of PS (upper - thickness 2.0 mm) and PC (bottom - thickness 2.0 mm). The material starts folding at around the time the surface of the sheet reaches T_g (~ 103 °C for PS and ~ 147 °C for PC).

Modeling temperature distribution inside the polymer sheet

We consider a polymer sheet of thickness H that is initially held at a temperature T_0 (experimentally, T_0 is equal to the ambient temperature, which we assume to be 30°C) At time $t=0$ one face of the sheet is exposed suddenly to a constant temperature ($T_1 > T_0$) while the other face is kept adiabatic (*i.e.*, there is no heat loss from the face into the surrounding). In our calculations, we take T_1 as a function of time obtained from the IR camera of the heated surface of the sheet.

The position-dependent temperature inside the sheet can be described as:

$$T(x, t) = T(x, \infty) + \sum_{n=0}^{\infty} c_n \sin(k_n x) \exp(-l_n t) \quad , \quad (\text{S3.6})$$

with boundary conditions given by:

$$\sin(k_n x) \Big|_{x=0} = 0 \quad , \quad (\text{S3.7})$$

$$\left. \frac{d}{dx} \sin(k_n x) \right|_{x=H} = k_n \cos(k_n x) \Big|_{x=H} = 0 \quad , \quad (\text{S3.8})$$

Note that x ranges from 0 (heated surface) to H (adiabatic surface).

From Equation S3.8, one obtains the following condition:

$$k_n H = \frac{\pi}{2} + n\pi \quad , \quad (\text{S3.9})$$

Moreover from the Fourier's law it follows that:

$$I_n = \left(n + \frac{1}{2} \right)^2 \left(\frac{\pi}{H} \right)^2 \alpha \cdot t \quad , \quad (\text{S3.10})$$

In Equation (A10), the thermal diffusivity, α , is given by:

$$\alpha = \frac{k}{\rho \cdot c_p} \quad , \quad (\text{S3.11})$$

where k is the thermal conductivity, ρ is the density and c_p is the specific heat.

Realizing that

$$\sum_{n=0}^{\infty} c_n \sin\left(\left(n + \frac{1}{2} \right) \frac{\pi}{H} x \right) = T_0 - T_1 \quad , \quad (\text{S3.12})$$

yields:

$$c_n = 2 \frac{T_0 - T_1}{\left(n + \frac{1}{2} \right) \pi} \quad , \quad (\text{S3.13})$$

Combining expressions given by Equation S3.6-Equation S3.13 together leads to:

$$T(x, t) = T_1 + \sum_{n=0}^{\infty} c_n \sin\left(\left(n + \frac{1}{2} \right) \frac{\pi}{H} x \right) \exp\left(- \left(n + \frac{1}{2} \right)^2 \frac{\pi^2 \alpha}{H^2} t \right) \quad (\text{S3.14})$$

with c_n given by Equation S3.13.

Equation S3.14 is solved using experimental values of k , ρ , and c_P (that give collectively the thermal diffusivity, α). The values of k , ρ , and c_P are given in Table S3.1.

Figure S3.5 shows the predictions of the temperature profile in the PS and PC samples in the hinged region of the samples.

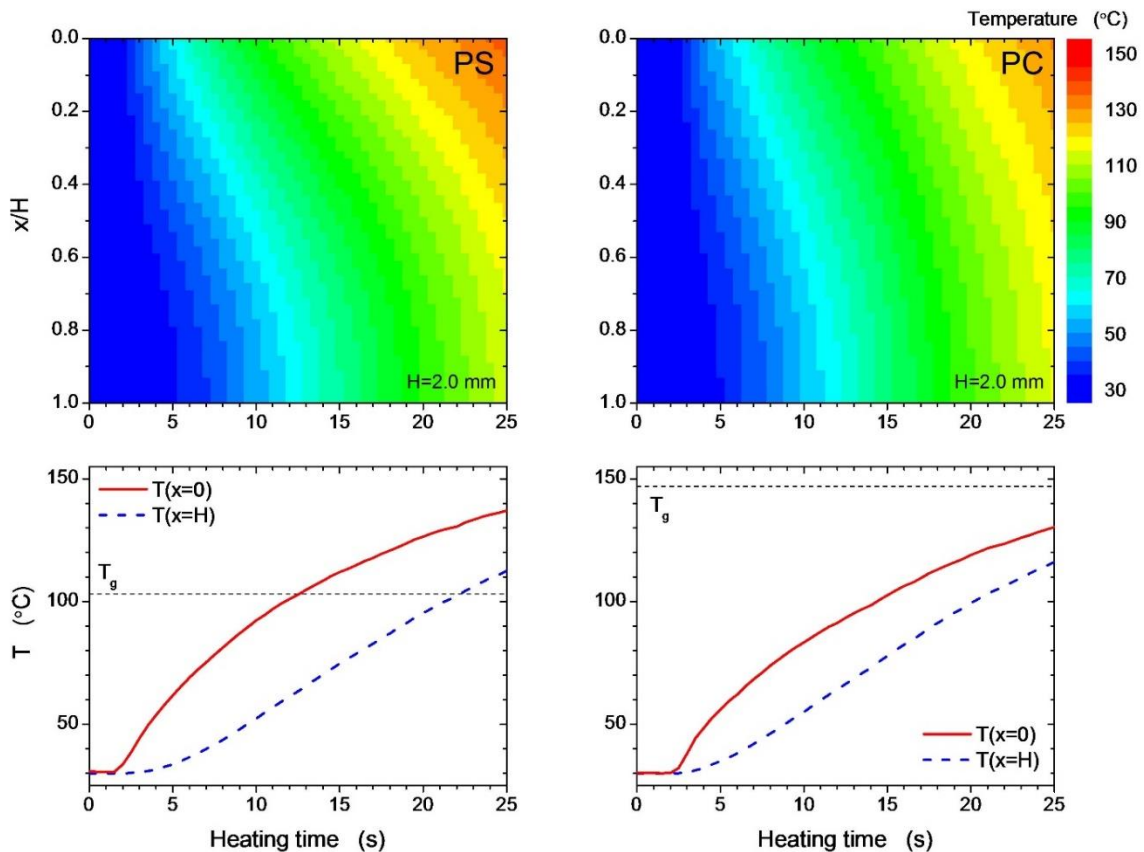


Figure S3.5. The top of each pair show the model's prediction of temperature profiles inside the sheets: PS 2.0 mm (left), and PC 2.0 mm (right). The bottom of each pair denotes the temporal evolution of the temperature on the front side (solid red line) and the backside (dashed blue line) of the sample.

Table S3.1. Physical characteristics of polymers

	K (W/m/K)	ρ (kg/m ³)	C _P (J/kg/K)	α (m ² /s)
PMMA	0.193	1195	1420	1.137 x 10 ⁻⁷
PS	0.116	1065	1185	9.192 x 10 ⁻⁸
PC	0.200	1220	1200	1.366 x 10 ⁻⁷

Note: All material properties are taken from references⁵² and⁵⁴.

References

1. Taylor, D., Dyer, D., Lew, V. & Khine, M. Shrink film patterning by craft cutter: complete plastic chips with high resolution/high-aspect ratio channel. *Lab. Chip* **10**, 2472–2475 (2010).
2. Chen, C.-S. *et al.* Shrinky-Dink microfluidics: 3D polystyrene chips. *Lab. Chip* **8**, 622–624 (2008).
3. Lin, S., Lee, E. K., Nguyen, N. & Khine, M. Thermally-induced miniaturization for micro- and nanofabrication: progress and updates. *Lab. Chip* **14**, 3475–3488 (2014).
4. Grimes, A. *et al.* Shrinky-Dink microfluidics: rapid generation of deep and rounded patterns. *Lab. Chip* **8**, 170–172 (2008).
5. Hayes, G. J., Liu, Y., Genzer, J., Lazzi, G. & Dickey, M. D. Self-Folding Origami Microstrip Antennas. *IEEE Trans. Antennas Propag.* **62**, 5416–5419 (2014).
6. Fernandes, R. & Gracias, D. H. Self-folding polymeric containers for encapsulation and delivery of drugs. *Adv. Drug Deliv. Rev.* **64**, 1579–1589 (2012).
7. Azam, A., Laflin, K. E., Jamal, M., Fernandes, R. & Gracias, D. H. Self-folding micropatterned polymeric containers. *Biomed. Microdevices* **13**, 51–58 (2011).
8. Felton, S., Tolley, M., Demaine, E., Rus, D. & Wood, R. A method for building self-folding machines. *Science* **345**, 644–646 (2014).
9. Silverberg, J. L. *et al.* Using origami design principles to fold reprogrammable mechanical metamaterials. *Science* **345**, 647–650 (2014).
10. Bothe, M. & Pretsch, T. Bidirectional actuation of a thermoplastic polyurethane elastomer. *J. Mater. Chem. A* **1**, 14491–14497 (2013).
11. An, B. *et al.* An end-to-end approach to making self-folded 3D surface shapes by uniform heating. in 1466–1473 (IEEE Conf. Robotics & Automation, 2014).
12. Liu, Y., Boyles, J. K., Genzer, J. & Dickey, M. D. Self-folding of polymer sheets using local light absorption. *Soft Matter* **8**, 1764–1769 (2012).
13. Beblo, R. V. & Weiland, L. M. Light Activated Shape Memory Polymer Characterization. *J. Appl. Mech.-Trans. Asme* **76**, 011008/1-8 (2009).
14. Habault, D., Zhang, H. & Zhao, Y. Light-triggered self-healing and shape-memory polymers. *Chem. Soc. Rev.* **42**, 7244–7256 (2013).
15. Lendlein, A., Jiang, H., Juenger, O. & Langer, R. Light-induced shape-memory polymers. *Nature* **434**, 879–882 (2005).
16. Ryu, J. *et al.* Photo-origami—Bending and folding polymers with light. *Appl. Phys. Lett.* **100**, 161908/1-5 (2012).

17. Agrawal, A., Yun, T., Pesek, S. L., Chapman, W. G. & Verduzco, R. Shape-responsive liquid crystal elastomer bilayers. *Soft Matter* **10**, 1411–1415 (2014).
18. Allensworth, J. R., Liu, Y., Braun, H., Genzer, J. & Dickey, M. D. In-plane deformation of shape memory polymer sheets programmed using only scissors. *Polymer* **55**, (2014).
19. Andres, C. M., Zhu, J., Shyu, T., Flynn, C. & Kotov, N. A. Shape-Morphing Nanocomposite Origami. *Langmuir* **30**, 5378–5385 (2014).
20. Behl, M., Zotzmann, J. & Lendlein, A. in *Shape-Memory Polymers* (ed. Lendlein, A.) 1–40 (Springer Berlin Heidelberg, 2010).
21. Chung, T., Romo-Uribe, A. & Mather, P. T. Two-Way Reversible Shape Memory in a Semicrystalline Network. *Macromolecules* **41**, 184–192 (2008).
22. Ge, Q., Dunn, C. K., Qi, H. J. & Dunn, M. L. Active origami by 4D printing. *Smart Mater. Struct.* **23**, 094007/1-15 (2014).
23. Nguyen, T. D., Jerry Qi, H., Castro, F. & Long, K. N. A thermoviscoelastic model for amorphous shape memory polymers: incorporating structural and stress relaxation. *J. Mech. Phys. Solids* **56**, 2792–2814 (2008).
24. Harris, R. D. *et al.* Chemical and Electrochemical Manipulation of Mechanical Properties in Stimuli-Responsive Copper-Cross-Linked Hydrogels. *ACS Macro Lett.* **2**, 1095–1099 (2013).
25. Ahmad, M., Luo, J. & MirafTAB, M. Feasibility study of polyurethane shape-memory polymer actuators for pressure bandage application. *Sci. Technol. Adv. Mater.* **13**, 15006 (2012).
26. Qi, H. J., Nguyen, T. D., Castro, F., Yakacki, C. M. & Shandas, R. Finite deformation thermo-mechanical behavior of thermally induced shape memory polymers. *J. Mech. Phys. Solids* **56**, 1730–1751 (2008).
27. Diani, J., Liu, Y. & Gall, K. Finite strain 3D thermoviscoelastic constitutive model for shape memory polymers. *Polym. Eng. Sci.* **46**, 486–492 (2006).
28. Leng, J., Wu, X. & Liu, Y. Infrared light-active shape memory polymer filled with nanocarbon particles. *J. Appl. Polym. Sci.* **114**, 2455–2460 (2009).
29. Lee, K. M., Koerner, H., Vaia, R. A., Bunning, T. J. & White, T. J. Light-activated shape memory of glassy, azobenzene liquid crystalline polymer networks. *Soft Matter* **7**, 4318–4324 (2011).
30. Behl, M., Razzaq, M. Y. & Lendlein, A. Multifunctional Shape-Memory Polymers. *Adv. Mater.* **22**, 3388–3410 (2010).
31. Berg, G. J., McBride, M. K., Wang, C. & Bowman, C. N. New directions in the chemistry of shape memory polymers. *Polymer* **55**, 5849–5872 (2014).

32. Jiang, H. Y., Kelch, S. & Lendlein, A. Polymers Move in Response to Light. *Adv. Mater.* **18**, 1471–1475 (2006).
33. Zhang, H. & Zhao, Y. Polymers with Dual Light-Triggered Functions of Shape Memory and Healing Using Gold Nanoparticles. *ACS Appl. Mater. Interfaces* **5**, 13069–13075 (2013).
34. Zeng, C., Seino, H., Ren, J. & Yoshie, N. Polymers with Multishape Memory Controlled by Local Glass Transition Temperature. *ACS Appl. Mater. Interfaces* **6**, 2753–2758 (2014).
35. Behl, M., Kratz, K., Zotzmann, J., Nöchel, U. & Lendlein, A. Reversible Bidirectional Shape-Memory Polymers. *Adv. Mater.* **25**, 4466–4469 (2013).
36. Higgins, M. J., Grosse, W., Wagner, K., Molino, P. J. & Wallace, G. G. Reversible Shape Memory of Nanoscale Deformations in Inherently Conducting Polymers without Reprogramming. *J. Phys. Chem. B* **115**, 3371–3378 (2010).
37. Liu, C., Qin, H. & Mather, P. T. Review of progress in shape-memory polymers. *J. Mater. Chem.* **17**, 1543–1558 (2007).
38. Lendlein, A. & Sauter, T. Shape-Memory Effect in Polymers. *Macromol. Chem. Phys.* **214**, 1175–1177 (2013).
39. Mather, P. T., Luo, X. F. & Rousseau, I. A. Shape Memory Polymer Research. *Annu. Rev. Mater. Res.* **39**, 445–471 (2009).
40. Leng, J., Lan, X., Liu, Y. & Du, S. Shape-memory polymers and their composites: Stimulus methods and applications. *Prog. Mater. Sci.* **56**, 1077–1135 (2011).
41. Kunzleman, J., Chung, T., Mather, P. T. & Weder, C. Shape memory polymers with built-in threshold temperature sensors. *J. Mater. Chem.* **18**, 1082–1086 (2008).
42. Behl, M., Kratz, K., Noechel, U., Sauter, T. & Lendlein, A. Temperature-memory polymer actuators. *Proc. Natl. Acad. Sci.* **110**, 12555–12559 (2013).
43. Westbrook, K. K. *et al.* Two-way reversible shape memory effects in a free-standing polymer composite. *Smart Mater. Struct.* **20**, 065010/1-9 (2011).
44. Pandini, S. *et al.* Two-way reversible shape memory behaviour of crosslinked poly(ϵ -caprolactone). *Polymer* **53**, 1915–1924 (2012).
45. Meng, H. *et al.* Various shape memory effects of stimuli-responsive shape memory polymers. *Smart Mater. Struct.* **22**, 093001/1-23 (2013).
46. Davis, D., Mailen, R., Dickey, M. & Genzer, J. Self-folding of polymer sheets using microwaves and graphene ink. *RSC Adv* 89254–89261 (2015).
47. Liu, Y., Miskiewicz, M., Escuti, M. J., Genzer, J. & Dickey, M. D. Three-dimensional folding of pre-strained polymer sheets via absorption of laser light. *J. Appl. Phys.* **115**, (2014).

48. Felton, S. M., Tolley, M. T., Onal, C. D., Rus, D. & Wood, R. J. Robot self-assembly by folding: A printed inchworm robot. in 277–282 (IEEE International Conference on Robotics and Automation, 2013).
49. Liu, Y., Mailen, R., Zhu, Y., Dickey, M. D. & Genzer, J. Simple geometric model to describe self-folding of polymer sheets. *Phys. Rev. E* **89**, 42601 (2014).
50. Starkova, O. & Aniskevich, A. N. Poisson's ratio and the incompressibility relation for various strain measures with the example of a silica-filled SBR rubber in uniaxial tension tests. *Polym. Test.* **29**, 310–318 (2010).
51. Mailen, R., Liu, Y., Dickey, M. D., Zikry, M. & Genzer, J. Modeling of shape memory polymer sheets that self-fold in response to localized heating. *Soft Matter* **11**, 7827–7834 (2015).
52. Brandrup, J., Immergut, E. H. & Grulke, E. A. *Polymer Handbook*. (2003).
53. Mailen, R. W., Liu, Y., Dickey, M. D., Zikry, M. & Genzer, J. Modelling of shape memory polymer sheets that self-fold in response to localized heating. *Soft Matter* **11**, 7827–7834 (2015).
54. Wypych, G. *Handbook of Polymers*. (ChemTec Publishing, 2012).

CHAPTER 4

Repeatable Reversible 2D to 3D Bilayer Shape Programming*

*In collaboration with Elton Luong, Russell Mailen, and Alan Russell

Overview

Folding is an attractive way to create 3D objects from 2D sheets. Materials that can change shape have potential applications in packaging^{1,2}, space exploration³, energy harvesting⁴⁻⁶, and toys. We sought to achieve folding by mimicking joints in the human body, which use tensile stress from filaments (i.e., muscle fibers) to actuate two rigid bodies (i.e., bones surrounded by tissue) connected by a hinge (i.e., joint). Here, stress from strained elastic filaments triggers self-folding of plastic sheets in uniform heat. After removing the elastic filaments, the folded objects revert to 2D sheets at elevated temperatures. These sheets fold reliably, reversibly, and repeatedly to create final shapes dictated by the placement of the tensile elements. A model based on the law of cosines predicts the dihedral angle as a function of the strain in the elastic filament. A thermo-mechanical model predicts the dihedral angle as a function of the elongation in the strained tensile elements. It is possible to reprogram the materials to unfold into a different shape when reheated by adding an extra heating step to the process. This system precisely controls converting 2D sheets to 3D objects using only commercially available polymer sheets, elastics, and heat.

4.1 Introduction

This chapter introduces a bilayer system that induces self-folding to convert two-dimensional (2D) sheets into three-dimensional (3D) objects in a hands-free manner. Bilayer systems are typically composed of two layers adhered together to create a laminate with both tunable mechanical properties and a shape that changes in response to an external stimulus. Many bilayer or composite polymer systems studied use hydrogels as one of the layers because they undergo reversible high volume expansion and contraction as well as increasing the biocompatibility of the laminate⁷⁻⁹. There are many bilayer systems that bend in response to a stimulus (e.g., heat, swelling, light)⁸⁻³³. Here, the bilayer system combines elastic filaments

with a thermoplastic polymer to enable self-folding behavior without permanently adhering the layers together.

We created a bilayer sheet composed of vulcanized polyisoprene (rubber bands) adhered to the surface of a poly(methyl methacrylate) (PMMA) sheet with metal binder clips. The PMMA is ablated with a VLS 3.5 laser writer to create thinner areas that define the 'hinges' where the sheet will fold. The rubber bands are cut into strips of various lengths and strained across the hinge as shown in **Figure 4.1**. We heat the bilayer (PMMA and rubber bands) in an oven at 130 °C, which is above the glass transition (T_g) of PMMA (105 °C)³⁴. As the sheet exceeds T_g , the hinge softens which allows the rubber bands to contract and fold PMMA as shown in **Figure 4.1A**. The strain in the rubber band controls the dihedral angle (α_D) of the folded PMMA sheet. The maximum α_D reached by this system is 180°. Controlling the hinge thickness (t_h) allows the hinge to vary between a sharp fold isolated to the hinge or a curve that occupies the entire region under the rubber band. Once folded, the sample can unfold by removing the rubber bands and re-heating the PMMA above its T_g .

This system can also be used to fold sequentially. First, a 3D object is folded using the technique described above and cooled without removing the rubber bands. After cooling, additional rubber bands can be added to the 3D objects to program new folds. When the sample is re-heated, the new rubber bands will induce self-folding and a second set of folds will occur. Many additional folds may be induced using this sequential folding technique.

In addition to designing the new folding system, we created two models: 1) a model that relates the strain in the rubber band to the dihedral angle based on law of cosines and 2) a model that balances the contraction force in the rubber band to the bending stiffness of the PMMA sheet in the hinge region. The force balance model predicts the temperature at the onset of folding. Both models predict the experimental results within expected error.

Finally, we developed a method to alter how 3D objects unfold when they are heated above T_g without rubber bands attached. **Figure 4.1B-C** shows the process with and without an additional heating step and how the heating step effects the unfolding process. If the material heats up slightly above the ‘terminal flow temperature’ (160 °C) while in a new shape, the material loses some entanglements and relaxes in the new shape. The ‘terminal flow temperature’ is a temperature above T_g where the polymer behaviors more like a viscous fluid and polymer chains can become less entangled. When unfolding, the sample returns to the new shape. Adding the extra heating step changes the shape the sample will return to when heated without rubber bands.

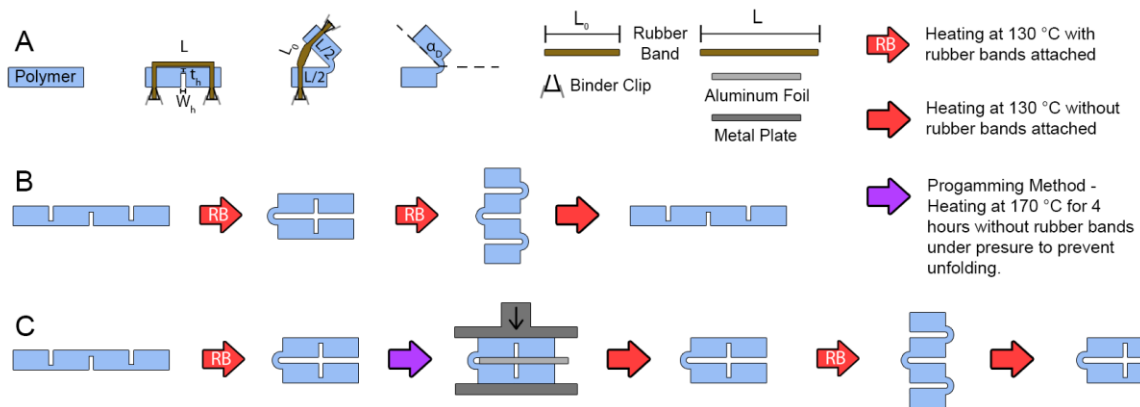


Figure 4.1. Schematic of the self-folding method using rubber bands. (A) A rubber band of initial length L_0 is stretched across the hinge region to length L , extended through the PMMA sheet, and secured with metal clips. The sample is placed in an oven at 130 °C until the increased temperature makes the thermoplastic hinge soft enough to allow the rubber band to relax back to L_0 , folding the sample to a dihedral angle (α_D). If the rubber bands are removed and the sample is reheated at 130 °C, the sample unfolds back to its original shape, or ‘base shape,’ regardless of which new shape it occupies. (B) Starting with a flat shape with multiple hinges, the sample sequentially folds into two different shapes. When the rubber bands are removed and the sample is heated again, it will unfold into the original shape. (C) The sample can be strained and heated to 170 °C to change which shape it will return to when it is unfolded. With the additional heating step, the sample behaves the same as the sample in B except it unfolds to the intermediate shape instead of the original flat sheet. Compare the last to steps of (B) and (C) for a side by side comparison.

4.2 Experimental Results – One Hinge Samples

We started with the simplest possible shape: a one hinge sample. We adhered rubber bands with different strains to measure its effect on dihedral angle. We use extension ratios when measuring strain to avoid confusing between different types of strain. Extension ratio (λ) is the ratio between the length strained sample (L) and the original length (L_0) as shown in Equation 4.1.

$$\lambda = \frac{L}{L_0} \quad (4.1)$$

The dihedral angle correlates directly to the extension ratio in the rubber band. **Figure 4.2A** shows a series of one hinge samples that were each folded using this technique to control the angle. We tested thicker sheets up to 6 mm thick and found that if the thickness of the hinge is less than 50% of the original sheet thickness, the sample will fold using the technique (i.e. a 6 mm sheet needs a hinge of 3 mm or less to self-fold). If the hinge is too thick, the force in the rubber band (~5-10 N) will be too weak to induce self-folding and the sample will not fold. If the hinge is too thin (<0.4 mm thick) the hinge will break from the strain in the rubber band.

The folding angle (α_F) is the angle between the two faces of the sample and the dihedral angle (α_D) is its supplement. Using the law of cosines, we developed a model (derived in the Model Derivation section in the SI) that predicts the dihedral angle based on the extension ratio as shown in Equation 4.2.

$$\alpha_D = 180^\circ - \arccos(1 - 2\lambda^{-2}) \quad (4.2)$$

This model makes a triangle using the strained rubber band as two sides of a triangle and the unstrained length as the third side as shown in **Figure 4.1A**. If three sides of a triangle are known, then the law of cosines can predict any angles within that triangle. **Figure 4.2B** shows how well the model predicts the experimental folding results for the samples with one hinge. As the extension ratio increases, the sheet starts to curl in the area immediately adjacent to

the hinge, causing a slight deviation from the model. As long as the samples do not bend outside of the ablated region, the model accurately predicts the relationship between strain in the rubber band and the dihedral angle achieved from self-folding.

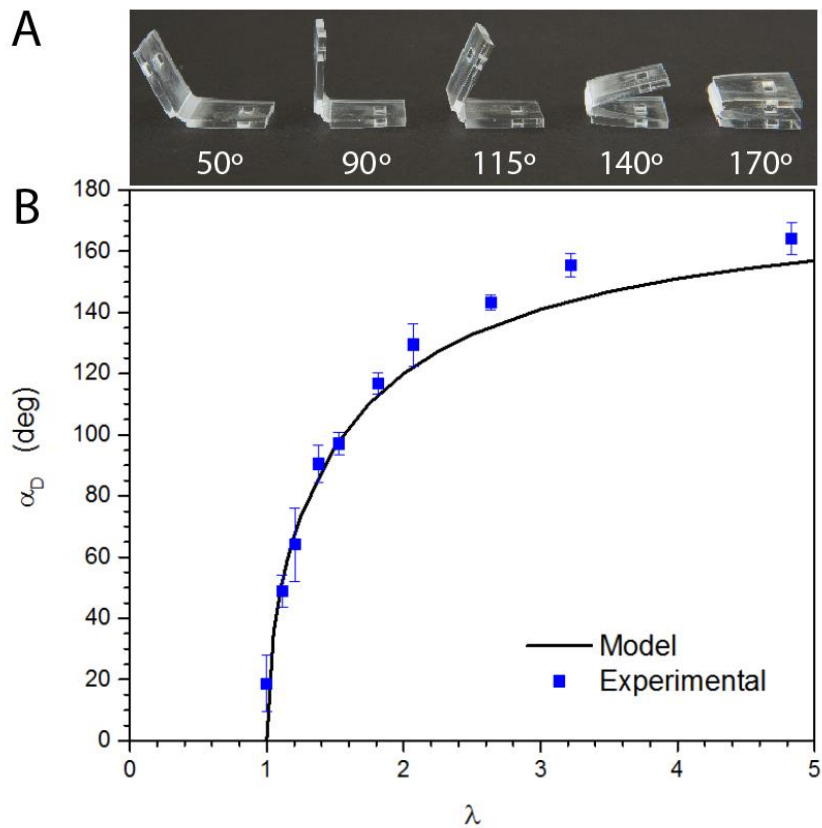


Figure 4.2. (A) Folded 2 mm thick PMMA sheets showing the effect of strain on dihedral angle. (B) This plot uses the extension ratio of the rubber band to accurately predict the dependence of dihedral angle based on Equation 4.2.

The kinetics can be controlled using multiple rubber bands. We tested samples using one or two rubber bands strained to an extension ratio of 3. Both samples had a hinge thickness of ~ 0.9 mm thick, a hinge width of 2 mm, and were placed in an oven at 130 °C. From the onset of fold until the sample stopped moving, the sample with 1 rubber band took ~ 30 seconds and the sample with 2 rubber bands took ~ 16 seconds to reach the same

dihedral angle. In the future, a more systematic study that various extension ratio, hinge width, hinge thickness, and number of rubber bands would be required to get statistically significant results.

4.3 Experimental Results – Complex Samples

The ability to precisely control the dihedral angle enables the generation of complex shapes. **Figure 4.3** shows a series of shapes formed by controlling the geometry of the PMMA sheet (defined by a laser writer), placement of the rubber bands, and extension ratios.

Although **Figure 4.3** shows a wide variety of shapes, it is not exhaustive. This system is easily adapted to many different shapes, size scales, and geometries. Origami shows us a vast variety of different objects paper can make. We hope to emulate origami to fabricate many of the same objects using this technique.

In **Figure 4.3A**, the crane pattern at the bottom of the figure that can generate both a sitting crane and a standing crane using the same pattern by changing the extension ratio in rubber band that folds the ‘wings’ of the crane. Using this idea, we created a set of structures that can modularly change their final design based solely on the placement and extension ratio of the rubber bands. We call this ‘modular origami.’

4.4 Experimental and Results – Modular Origami

We created patterns with multiple places to connect the rubber bands. Depending on where the rubber band is adhered, the sheet will fold into one of a variety of different shapes. **Figure 4.3B** shows three possible final structures from each of two different modular designs – the hex pattern and the cross patterned box. The asymmetry in the hex pattern allows the same folding connection to behave differently if rotated 90°.

Since the folding is fully reversible, the modular patterns can be unfolded and refolded into different shapes. Folding and unfolding the same shape more than five times tends to break the sample at the hinge, but more cycles are possible depending on the complexity of the pattern.

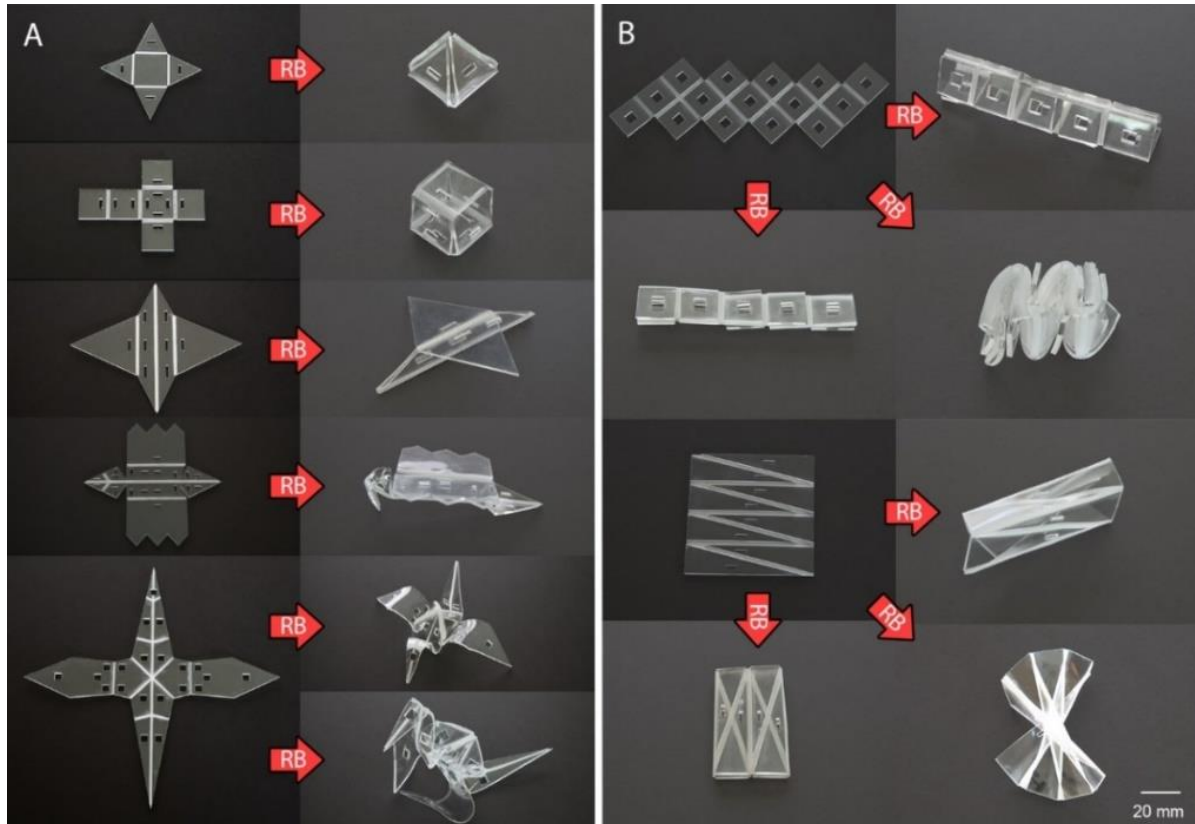


Figure 4.3. Complex shapes (A) and a series of modular shapes (B). The pyramids, cubes, planes, birds, and cranes were folded by designing a series of flat samples with hinges across the regions that need to fold. The modular patterns contained two different base shapes, a hex pattern and a cross patterned box which each fold into a variety of different shapes shown below the base images. The hex pattern can fold into a cylinder, a flat line, and a fully collapsed cell. The cross patterned box can fold into an offset cylinder, a flat square, and a fan. By connecting the rubber bands to different areas, even more shapes can be discovered from the same base patterns. Both sets of shapes were cut and ablated with a laser writer and folded in an oven at 130 °C.

4.5 Modeling Results – Balancing Forces

We created a model that balances the forces in the system to predict the temperature at the onset of folding. The model compares the elastic force of the rubber band and the bending stiffness of the polymer sheet. The onset of folding occurs when the force generated by the elongated rubber band (F_R) exceeds the stiffness of the polymer sheet (F_S), $F_S < F_R$, and the temperature is near T_g . If the temperature of the sample is too low, the hinge will break when the force in the rubber band exceeds the stiffness of the polymer sheet.

The resistance of the polymer sheet to movement can be described using the constitutive equation of beam bending, shown in Equation 4.3, which relates the elastic modulus (E), the moment of inertia (I) and the second derivative of displacement with respect to distance ($\frac{d^2v}{dx^2}$) to the bending moment (M):

$$EI \frac{d^2v}{dx^2} = M \quad (4.3)$$

Following the derivation shown in the SI, the constitutive model relates the force required to bend the sheet (F_S) to the elastic modulus (E), sheet width (W), hinge thickness (t_h), dihedral angle (α_D), and hinge width (W_h) as shown in Equation 4.4:

$$F_S = \frac{EWt_h^2\alpha_D}{3W_h} \quad (4.4)$$

The rubber band generates the force necessary to overcome F_S . Equation 4.5 derives from thermodynamic first principles, as shown in the SI³⁵. This equation relates the constriction force (F_R) to the density (ρ), gas constant (R), temperature (T), initial cross sectional area of the rubber band (A_i), molecular weight between crosslinks (M_c), and extension ratio (λ).

$$F_R = \frac{\rho RTA_i}{M_c} \left(\lambda - \frac{1}{\lambda^2} \right) \quad (4.5)$$

$$\alpha_D = \frac{3W_h\rho RTA_i}{EWt_h^2M_c} \left(\lambda - \frac{1}{\lambda^2} \right) \quad (4.6)$$

At the onset of folding, F_R and F_S are approximately equal, therefore, this system of equations reduces to Equation 4.6 and predicts α_D as a function of T , geometry, material properties, and λ . In **Figure 4.4A**, we plot α_D as a function of T and t_h . We hold W_h , ρ , R , A_i , W , λ , and M_c all constant. E is a function of T so it is evaluated at each temperature and not held constant. For each t_h , there is a T where α_D rapidly increases. This T is the temperature when the onset of folding occurs. To show this effect more clearly, a plot $\frac{d\alpha_D}{dT}$ as a function of T shows where the most rapid change in α_D takes place, as plotted in **Figure 4.4B**. From these graphs, the onset of folding occurs between 102 °C and 110 °C. Compared to our experimental data in **Figure 4.4C**, the model predicts the experimental temperature at the onset of folding. The model fails to predict the temperature at the onset of folding correctly around 0.8 mm thick hinges. Above a hinge thickness of 0.8 mm, the area around the hinge bends as the hinge folds. If the bending occurs in both the hinge region and the sheet, the model cannot predict the folding behavior accurately.

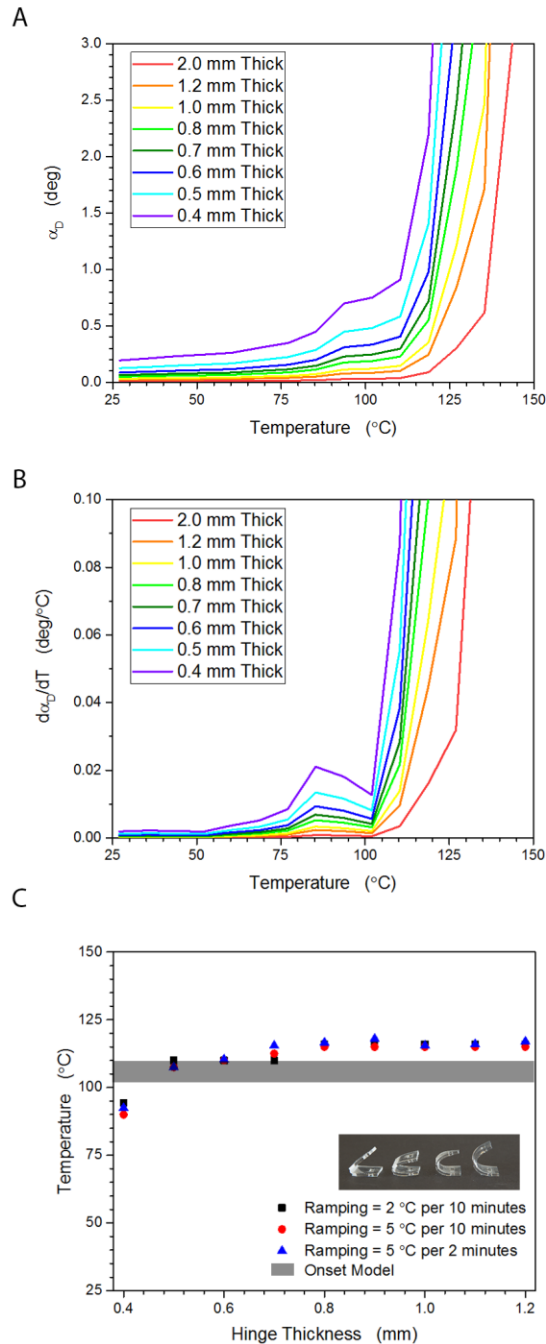


Figure 4.4. (A) The model predicts the α_D at the point when $F_S=F_R$ as a function of t_h (solid, rainbow) and T . Above a critical onset temperature, the sheet will fold. (B) $\frac{d\alpha_D}{dT}$ plotted as a function of temperature. This figure shows the T when α_D drastically increases. There is a major and minor relaxation in the sheet. The major relaxation predicts the onset folding. (C) Using this model, we predict the temperature at the onset of folding and compare the model to experimental data. The experimental data was taken by heating a sample to a temperature, holding it at that temperature for a given duration and then slowly ramping the temperature up until the samples folded. In these experiments, we noticed that once a sample folded a certain amount, it would continue folding to the maximum angle predicted in **Figure 4.2**.

4.6 Method to Reprogram Unfolding

The folding is fully reversible; the sample unfolds back into the original flat shape when heated in the absence of the rubber bands. We altered the unfolding process to create two identical folded structures that unfold into different shape when heated without rubber bands. The reprogramming method uses principles from shape memory polymers. We folded our modular hex pattern into its flat configuration (**Figure 4.5**) and annealed the sample while it was confined at 170 °C for 4 hours. This is above the glass transition temperature (105 °C) and above 'terminal flow temperature' (160 °C). We speculate that at this temperature, the sample relieves its internal stress while maintaining its strain. Now, the sample will unfold into the shape held during the extra heating step as shown in **Figure 4.5B**. The sample is confined to prevent unfolding. Aluminum foil prevents adjacent polymer layers from interpenetrating during the annealing step as shown in **Figure 4.1C**.

In **Figure 4.5C**, we show a series of photographs of the unfolding process. The sample created with the standard folding method unfolds into the original shape (the hex pattern) and the sample created with the reprogramming method unfolds into the secondary shape.

The reprogramming method works, but it is tricky to balance the relaxation of the polymer. If the sample does not relax enough, it will not be reprogrammed. If the sample relaxes too much, the hinges will flow and break apart. If the technique is perfected, it could be used to create objects that look the same but behave differently under heat. Objects that look identical but change into different shapes when heated have been studied previously using shrink films that were uniaxially strained in one direction but cut at different angles relative to the prestrain direction³⁶.

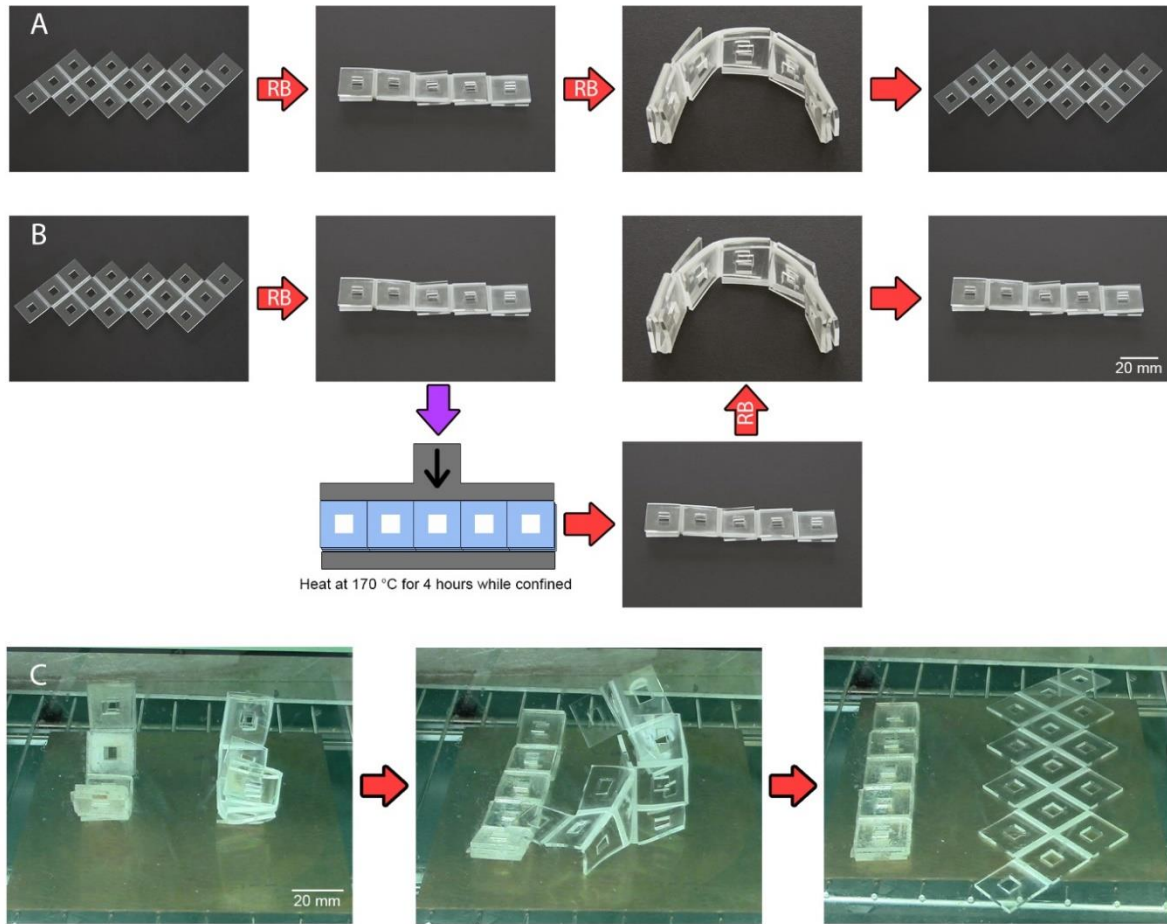


Figure 4.5. Using the programming methods shows in **Figure 4.1**, here are the experimental results for the folding method (A), the reprogramming method (B), and the side by side comparison in the oven (C). The reprogramming method contains an extra heating step that anneals PMMA in a high heat while preventing the shape from changing with a metal weight. This extra step allows the sample to relax and resets the base shape. Instead of reforming the initial shape (hex pattern) upon additional heating without rubber bands, it relaxes back to the intermediate shape (flat pattern).

4.7 Conclusion

We demonstrated a method to create complex origami folds using only rubber bands, binder clips, ablated sheets of PMMA, and an oven. The sheets can be folded reliably, reversibly, and repeatedly. The rubber band programs the dihedral angle as predicted by the law of cosines model. A force balance model predicts the onset of folding in samples with hinges between 0.4 - 0.8 mm thick. Finally, we created a reprogramming method that changes

the base structure that our samples unfold into when the rubber bands have been removed and heat is applied.

4.8 Acknowledgements

We thank the National Science Foundation for supporting this work under the NSF EFRI program (Grant No. 1240438).

Supporting Information

Experimental Setup

We take a flat, 2 mm thick sheet of PMMA from McMasterCarr and use a VLS 3.5 laser in raster mode to ablate the sheet making hinges that are 2 mm wide and 0.8 mm thick. Then, we use the laser in vector mode to cut the desired pattern out of the sheet. These patterns include holes 3.5 cm from the nearest hinge to allow the insertion of rubber bands through the sheet. The shapes used are derived from origami folding patterns.

Advantage® rubber bands are cut into strips. The rubber bands are strained across the hinge and inserted through the holes in the sheet. Then, we used a 32 mm binder clips to adhere the rubber band to the sheet and prevent the strained rubber band from relaxing. For complex shapes, this process is repeated for each hinge in the sheet. Once all the rubber bands are adhered to the sheet, we place the sheet into the oven at 130 °C. After 2-5 minutes, the sample will fold.

To convert a 3D object to a 2D sheet, remove the rubber bands adhered to the sample, put the object back into the oven at 130 °C and wait 10 minutes. The sample will unfold and regenerate the original flat sheet (or the secondary structure if the reprogramming method is used). In some cases, additional heating is required to return to a completely flat shape.

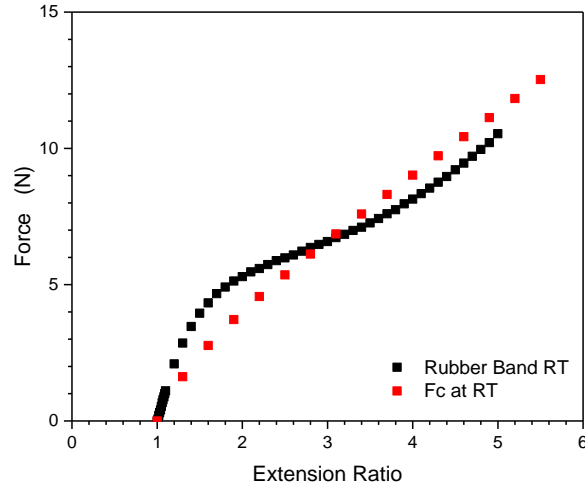


Figure S4.1. The contraction force in the rubber band calculated with an extensometer co-plotted with F_c from the balance of forces model. F_c does not predict the rubber band behavior perfectly, so it will cause some errors in ability of the model to predict the temperature at the onset of folding. The force balance model was calculated with an extension ratio of 3 to minimize these errors.

Law of Cosines Model

$$c^2 = a^2 + b^2 - 2ab\cos(C) \quad (S4.1)$$

Where 'a', 'b', and 'c' are sides of the triangle and C is the angle opposite side 'c'.

$$C = \alpha_F, \quad a = \frac{L}{2}, \quad b = \frac{L}{2}, \quad c = L_0, \quad \lambda^{-2} = \frac{L_0^2}{L^2} \quad (S4.2)$$

Where α_F is the angle between two facing sides of the polymer sheet, L is the length of the rubber band when extended, L_0 is the original length of the rubber band, and λ is the extension ratio. When these substitutions are made, Equation S4.1 becomes Equation S4.3.

$$L_0^2 = \left(\frac{L}{2}\right)^2 + \left(\frac{L}{2}\right)^2 - 2\left(\frac{L}{2}\right)^2 \cos(\alpha_F) \quad (S4.3)$$

$$L_0^2 - \frac{L^2}{2} = -2\left(\frac{L}{2}\right)^2 \cos(\alpha_F) \quad (S4.4)$$

$$1 - 2 \frac{L_0^2}{L^2} = \cos(\alpha_F) = 1 - 2\lambda^{-2} \quad (\text{S4.5})$$

We are interested in dihedral angle (α_D) which is the supplementary angle to α_F in order to use the beam bending model.

$$\alpha_D = 180^\circ - \arccos(1 - 2\lambda^{-2}) \quad (\text{S4.6})$$

Equation S4.6 is the model used to predict dihedral angles as a function of extension ratio as shown in **Figure 4.3**.

Onset Time Model - F_s Derivation

Beam bending is a setup where a sheet is attached to a wall on one side and lifted straight up on the other. It allows us to quantify how material parameter affect how material bend. For our system, our pulling force is parallel instead of perpendicular. We start with the general constitutive model that relates the elastic modulus (E), the moment of inertia (I) and the second derivative of displacement with respect to distance ($\frac{d^2v}{dx^2}$) to the bending moment (M). In this case distance is along the length of the sheet and displacement is normal to the sheet.

$$EI \frac{d^2v}{dx^2} = M \quad (\text{S4.7})$$

From Equation S4.7, we know that the slope of deflection curve is the first derivative of displacement and only displacement changes with respect to distance. The boundary conditions are shown in Equation S4.8 and Equation S4.10 are used to derivate Equation S4.9 and Equation S4.11 respectively.

$$EI \frac{dv}{dx} = Mx + C_1 \quad \text{BC 1) } \frac{dv}{dx} = 0 \quad @ \quad x = 0 \quad \text{so } C_1 = 0 \quad (\text{S4.8})$$

$$EI \frac{dv}{dx} = Mx \quad (\text{S4.9})$$

We integrate again and apply the second boundary condition.

$$EIv = \frac{Mx^2}{2} + C_2 \quad \text{BC 2) } v = 0 \text{ @ } x = 0 \quad \text{so } C_2 = 0 \quad (\text{S4.10})$$

$$EIv = \frac{Mx^2}{2} \quad (\text{S4.11})$$

Here, we substitute the relationships shown in Equation S4.12 that we know from the geometry of our system and the small angle approximation (onset of folding is measured when the angle reaches 1°). In these equations, include the elastic modulus (E), hinge thickness (t_h), sheet width (W), dihedral angle (α_D), hinge width (W_h), and force required to bend the sheet (F_s). Finally, we reach our model after substituting into Equation S4.13 and rearranging to get Equation S4.14.

$$I = \frac{Wt_h^3}{12} \frac{v}{W_h} = \tan(\alpha_D) \sim \alpha_D \quad M = \frac{F_s t_h}{2} \quad x = W_h \quad (\text{S4.12})$$

$$\frac{EWt_h^3 \alpha_D W_h}{12} = \frac{F_s t_h W_h^2}{4} \quad (\text{S4.13})$$

$$F_s = \frac{EWt_h^2 \alpha_D}{3W_h} \quad (\text{S4.14})$$

The elasticity modulus is from the literature³⁷ and is based on a strain rate of 10^{-4} s^{-1} as a function of temperature.

Onset Time Model – F_R Derivation

This derivation is based on a similar derivation from Principles of Polymer Engineering³⁵. For ideal rubber, we can define the force holding the rubber together relative to the entropy in the system using Equation S4.15. This equation comes from the general equation of state for rubber when the entropic forces dominate the equation.

$$F_R = -T \left(\frac{\delta S}{\delta L} \right)_{T,V} \quad (\text{S4.15})$$

If we assume:

- No volume change occurs upon stretching, then $\lambda_x \lambda_y \lambda_z = 1$ where λ_x , λ_y and λ_z are extension ratios along the x, y and z axes, respectively.
- For uniaxial extension along the z-axis ($\lambda_z = \lambda$).
- Deformation is affine.
- $P(r)$ = probability that the end-to-end distance of a randomly coiled network chain is r and that $P(r)$ is given by the Gaussian distribution.
- We can use the Boltzmann equation to get the entropy as shown in Equation S4.16. The Boltzmann equation relates entropy (S), to the Boltzmann's constant (k) and probability of achieving a given state ($P(r)$).

$$S = k \ln(P(r)) \quad (S4.16)$$

From these assumptions, we can generate Equation S4.17.

$$\Delta S = \frac{-\rho R V}{2M_c} (\lambda_x^2 + \lambda_y^2 + \lambda_z^2 - 3) \quad (S4.17)$$

For uniaxial extension in the z-axis, $\lambda_z = \lambda$ and $\lambda_x = \lambda_y = \lambda^{-1/2}$ and get Equation S4.18.

$$\Delta S = \frac{-\rho R V}{2M_c} (\lambda^2 + \frac{2}{\lambda} - 3) \quad (S4.18)$$

We then took Equation S4.18 and substituted it into Equation S4.15 (after changing variables from L to λ and ended with Equation S4.19, which relates the constriction force (F_c) to the density (ρ), gas constant (R), temperature (T), initial cross sectional area of the rubber band (A_i), molecular weight between crosslinks (M_c), and extension ratio (λ).

$$F_c = \frac{\rho R T A_i}{M_c} \left(\lambda - \frac{1}{\lambda^2} \right) \quad (S4.19)$$

References

1. Lee, N. & Pellegrino, S. Packaging and deployment strategies for synthetic aperture radar membrane antenna arrays. in 1–4 (IEEE, 2014).
2. Kimionis, J. & Tentzeris, M. Origami antennas and packaging using 3D printing technologies. *SPIE Newsroom* (2015).
3. Zirbel, S. A. *et al.* HanaFlex: a large solar array for space applications. in (eds. George, T., Dutta, A. K. & Islam, M. S.) 94671C/1-9 (Proc. SPIE, 2015).
4. Invernizzi, F., Dulio, S., Patrini, M., Guizzetti, G. & Mustarelli, P. Energy harvesting from human motion: materials and techniques. *Chem. Soc. Rev.* **45**, 5455-5473 (2016).
5. Kornbluh, R. D. *et al.* Dielectric elastomers: Stretching the capabilities of energy harvesting. *Mrs Bull.* **37**, 246–253 (2012).
6. Zi, Y. *et al.* Harvesting Low-Frequency (<5 Hz) Irregular Mechanical Energy: A Possible Killer Application of Triboelectric Nanogenerator. *ACS Nano* **10**(4), 4797–4805 (2016).
7. Bassik, N., Abebe, B. T., Laffin, K. E. & Gracias, D. H. Photolithographically patterned smart hydrogel based bilayer actuators. *Polymer* **51**, 6093–6098 (2010).
8. Shim, T. S., Kim, S., Heo, C., Jeon, H. C. & Yang, S. Controlled Origami Folding of Hydrogel Bilayers with Sustained Reversibility for Robust Microcarriers. *Angew. Chem. Int. Ed.* **51**, 1420–1423 (2012).
9. Jamal, M. *et al.* Bio-Origami Hydrogel Scaffolds Composed of Photocrosslinked PEG Bilayers. *Adv. Healthc. Mater.* **2**, 1142–1150 (2013).
10. Wong, W. S. Y. *et al.* Mimosa Origami: A nanostructure-enabled directional self-organization regime of materials. *Sci. Adv.* **2**, (2016).
11. Jiang, W. *et al.* Photoresponsive Soft-Robotic Platform: Biomimetic Fabrication and Remote Actuation. *Adv. Funct. Mater.* **24**, 7598–7604 (2014).
12. Deng, T. *et al.* Self-folding graphene-polymer bilayers. *Appl. Phys. Lett.* **106**, 203108/1-4 (2015).
13. Stoychev, G., Zakharchenko, S., Turcaud, S., Dunlop, J. W. C. & Ionov, L. Shape-Programmed Folding of Stimuli-Responsive Polymer Bilayers. *ACS Nano* **6**, 3925–3934 (2012).

14. Agrawal, A., Yun, T., Pesek, S. L., Chapman, W. G. & Verduzco, R. Shape-responsive liquid crystal elastomer bilayers. *Soft Matter* **10**, 1411–1415 (2014).
15. Ge, Q., Dunn, C. K., Qi, H. J. & Dunn, M. L. Active origami by 4D printing. *Smart Mater. Struct.* **23**, 094007/1-15 (2014).
16. Felton, S., Tolley, M., Demaine, E., Rus, D. & Wood, R. A method for building self-folding machines. *Science* **345**, 644–646 (2014).
17. Martinez, R. V., Fish, C. R., Chen, X. & Whitesides, G. M. Elastomeric Origami: Programmable Paper-Elastomer Composites as Pneumatic Actuators. *Adv. Funct. Mater.* **22**, 1376–1384 (2012).
18. Mu, X. *et al.* Photo-induced bending in a light-activated polymer laminated composite. *Soft Matter* **11**, 2673–2682 (2015).
19. Wang, C. *et al.* Printed Carbon Nanotubes on Polymer Films for Active Origami. *Mater. Res. Lett.* **1**, 13–18 (2013).
20. Tolley, M. T. *et al.* Self-folding origami: shape memory composites activated by uniform heating. *Smart Mater. Struct.* **23**, 094006/1-9 (2014).
21. Felton, S. M. *et al.* Self-folding with shape memory composites. *Soft Matter* **9**, 7688–7694 (2013).
22. Andres, C. M., Zhu, J., Shyu, T., Flynn, C. & Kotov, N. A. Shape-Morphing Nanocomposite Origami. *Langmuir* **30**, 5378–5385 (2014).
23. Meng, H. & Li, G. A review of stimuli-responsive shape memory polymer composites. *Polymer* **54**, 2199–2221 (2013).
24. Chen, S., Hu, J. & Zhuo, H. Properties and mechanism of two-way shape memory polyurethane composites. *Compos. Sci. Technol.* **70**, 1437–1443 (2010).
25. Ratna, D. & Karger-Kocsis, J. Recent advances in shape memory polymers and composites: a review. *J. Mater. Sci.* **43**, 254–269 (2008).
26. Hu, J., Zhu, Y., Huang, H. & Lu, J. Recent advances in shape-memory polymers: Structure, mechanism, functionality, modeling and applications. *Prog. Polym. Sci.* **37**, 1720–1763 (2012).
27. Leng, J., Lan, X., Liu, Y. & Du, S. Shape-memory polymers and their composites: Stimulus methods and applications. *Prog. Mater. Sci.* **56**, 1077–1135 (2011).

28. Shan, W., Lu, T. & Majidi, C. Soft-matter composites with electrically tunable elastic rigidity. *Smart Mater. Struct.* **22**, 085005 (2013).
29. Xu, B. *et al.* Thermo-mechanical properties of polystyrene-based shape memory nanocomposites. *J. Mater. Chem.* **20**, 3442 (2010).
30. Tobushi, H., Hayashi, S., Sugimoto, Y. & Date, K. Two-Way Bending Properties of Shape Memory Composite with SMA and SMP. *Materials* **2**, 1180–1192 (2009).
31. Westbrook, K. K. *et al.* Two-way reversible shape memory effects in a free-standing polymer composite. *Smart Mater. Struct.* **20**, 065010/1-9 (2011).
32. Smela, E. Microfabrication of PPy microactuators and other conjugated polymer devices. *J. Micromechanics Microengineering* **9**, 1 (1999).
33. Hawkes, E. *et al.* Programmable matter by folding. *Proc. Natl. Acad. Sci.* **107**, 12441–12445 (2010).
34. Brandrup, J., Immergut, E. H. & Grulke, E. A. *Polymer Handbook*. (2003).
35. Allensworth, J. R., Liu, Y., Braun, H., Genzer, J. & Dickey, M. D. In-plane deformation of shape memory polymer sheets programmed using only scissors. *Polymer* **55**, 5948–5952 (2014),
36. Mulliken, A. D. & Boyce, M. C. Mechanics of the rate-dependent elastic–plastic deformation of glassy polymers from low to high strain rates. *Int. J. Solids Struct.* **43**, 1331–1356 (2006).
37. McCrum, N. G., Buckley, C. P. & Bucknall, C. B. Principles of polymer engineering. *Oxf. Univ. Press N. Y.* (1988).

CHAPTER 5

Compressed Thermoplastic Polymers for Fabricating Tunable Self-Folding Devices

*In collaboration with Amber Hubbard

Overview:

Prestrained thermoplastic polymers shrink when heated above their glass transition temperature (T_g). This property is useful for self-actuating devices including sheets that self-fold by localizing heat to precise regions on the sheet. Polymers are attractive materials for self-folding based on their commercial availability, ease of handling, and low cost. However, there are only a few commercial prestrained polymer sheets; examples include: Shrinky Dinks[®], Eastman's Embrace[™], and polyurethane shrink film. The process to fabricate these films requires expensive equipment to simultaneously heat and strain the sheets. Due to the limited number of commercially available shrink films and processing conditions (i.e., strains, moduli, or thicknesses), we created a new fabrication system using heated compression of polymer sheets to manufacture strained polymers from planar, unstrained thermoplastic sheets. After straining, these materials can self-fold into complex geometries when exposed to external stimuli and can fully recover their initial geometry when heated uniformly. Digital Image Correlation (DIC) is used to measure the strain profile within the strained samples while a Mooney-Rivlin model and geometric model predict the average strain and folding response of our samples, respectively. The model predictions agree with experimental results. Complex geometries are obtained experimentally with both thick (~12 mm) and thin (~1 mm) strained polymers. The techniques presented here should work with many thermoplastic, thus increasing the available pool of polymers for self-actuating devices made from commercially available thermoplastics.

5.1 Introduction:

Prestrained thermoplastic sheets are a class of shape memory polymers used in many applications, including self-actuated devices¹⁻¹¹, microfluidics¹²⁻¹⁴, and manufacturing¹⁴⁻¹⁶. To create a pre-strained thermoplastic sheet, the original polymer is heated above its T_g ,

stretched either biaxially or uniaxially, and cooled below the T_g to prevent the sheet from relaxing. Industrially, prestrained polymer sheets are made through numerous methods including blown film extrusion, roll-to-roll processing, or film casting. These processes stretch the sheet biaxially and change the shape of the sheet to match the intended application. Unfortunately, the tools to apply prestrain are typically expensive and large. Therefore, they are not common in academic research laboratories. Access to pre-strained polymer sheets is limited to commercial sheets, which restricts the diversity of polymers, thicknesses, and strains that are accessible. Here, we present a laboratory scale method to generate strained thermoplastic sheets to produce self-actuated devices.

Our method induces relatively uniform radial strain throughout planar polymer sheets via compression using a melt press. First, we acquired unstrained thermoplastic sheets of various thicknesses and compositions. We tested polystyrene (PS) from 1 to 6 mm in thickness and poly(methyl methacrylate) (PMMA) from 1 to 12 mm in thickness. Secondly, we used a melt press to compress the material at a temperature slightly below the T_g of the polymer sheet. Finally, we removed the strained sheet from the melt press and rapidly cooled the sheet to preserve the imposed strain. These strained polymer samples can then be used to produce self-actuating devices. In terms of applications, this work is divided into two regimes: thin sheets (~ 1 mm) and thick sheets (~ 6 – 12 mm).

Previously, our group explored using localized heating to induce self-folding in thin prestrained PS sheets, commercially known as Shrinky-Dinks®. Researchers developed techniques to actuate folding using a myriad of external stimuli including light^{2,5,8}, lasers⁷, and microwaves¹⁰. These systems use asymmetric heating to shrink the surface of the polymer sheet faster than the bottom of the sheet, thus forcing the sheet to fold toward the heating source. Inspired by methods developed earlier, we initiated a self-folding response using the thin, strained samples created from melt pressing.

Previously, localized stretching was used to create unidirectional strain within thick polymer sheets, allowing them to fold upon asymmetric heating¹¹. However, this work failed to create complex geometries because we could only strain uniaxially. In contrast, the samples formed here by the melt press have radially symmetric strain which enables the creation of complex origami shapes from a homogenous polymer sheet. Portions of the polymer sheets were ablated away using a Universal[®] Laser System VLS 3.5 laser cutter to create “hinges” composed of thinner regions on the sample. By asymmetrically heating the sample the strain is released locally resulting in self-folding of a thick sheet. A schematic depicting both the thick and thin folding processes are shown in **Figure 5.1**.

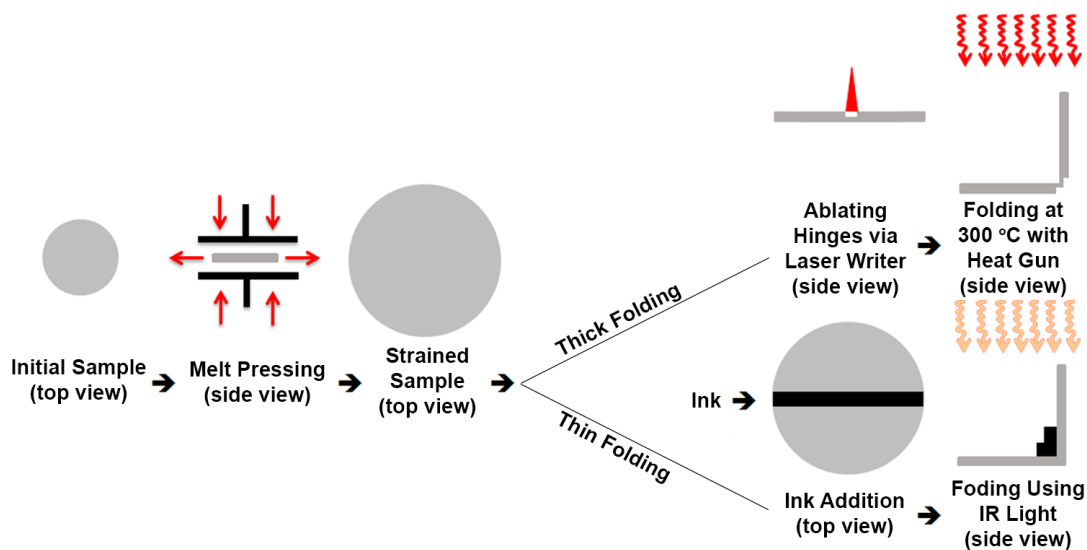


Figure 5.1. Schematic to produce strained sheets compressed with a melt press. If these sheets are put under a heat gun (red) or an IR light (orange), they will self-fold. All samples of varying thicknesses and polymer compositions were initially cut into a 75 mm diameter disk using a laser cutter and compressed in a melt press at an elevated temperature (below the T_g of each sheet). The strained samples then were either modified using hinge ablation (via laser cutting for sample thicknesses 6-12 mm) or ink addition (via China Marker for sample thickness ≤ 1 mm). An asymmetric temperature profile induces self-folding in the thick and thin samples via a heat gun or local light absorption, respectively.

5.2 Digital Image Correlation – Strain Quantification

Digital image correlation (DIC) is a photography-based strain mapping technique used to calculate and pictorially represent the strain profile within a sample. By placing a pattern of random dots (here, using a black marker) on samples before straining, the DIC software maps the strain within the entire sample by calculating how each dot has shifted due to in-plane deformation of the sheet. The samples are imaged before and after melt pressing and these images serve as an input for the DIC software (Ncorr, an open source plugin for MATLAB available at: <http://www.ncorr.com/>) for image analysis. **Figure 5.2** shows strain profiles in the X and Y directions (E_{xx} and E_{yy} , respectively) as a function of the force applied in the melt press during straining. Some samples exhibit non-uniform distribution of strain after melt pressing due to experimental factors such as misalignment of the heating platens, nonuniform heating, slippage of the sheet within the melt press, and thickness variation in the polymer sheets.

We use Ncorr to perform the DIC analysis. To operate, Ncorr requires 2 photos, a pre- and post-compression image of the sample. Before quantitative analysis begins, we align these images using Photoshop. Both images must be perfectly aligned and be within the same focal plane to produce accurate strain mapping results. After adjusting both images, they are uploaded into Ncorr. The software begins strain mapping by finding a “seed” spot, an identical spot located on both the initial and final images of the sample. Ncorr checks with the user to verify the seed spot locations on both photos and after approving the seed, Ncorr maps the profile by calculating the distance from the seed to the neighboring dots in both images. By determining the difference in distances between the same dot in the unstrained and strained images, Ncorr calculates the strain in the region between the dots. By repeating this process for each set of dots throughout the sample, Ncorr generates a strain profile and indicates the strain uniformity of the sample as shown in **Figure 5.2**.

To map the strain field correctly within our samples, we use a unique dot profile. When the dots are arranged with equal spacing between the dots, Ncorr is unable to accurately tabulate the strain within the sample. The software tries to indicate the “seed” spot on the pre- and post-strained images and the spots do not match (i.e., if the seed is set to the center in the “before” image, the software might create a match with the edge of the sample in the “after” image). Thus, we used a semi-randomized sequence of dots with two distinct features to orient the images as shown in **Figure 5.2A**. In the center of the sample, there is an asymmetric 3-dot pattern that allows us to create a consistent “seed” spot when Ncorr starts mapping the strain. The 3-dot pattern is different from the rest of the sample to avoid false positives. Directly above the 3-dot pattern is a 5-dot pattern used to align the pre- and post-strained images radially. These two unique features increase the accuracy of the DIC measurement.

Most DIC derived strain profiles for samples strained in the melt pressed appear relatively uniform. However, there are many experimental factors leading to non-uniformities in strain. In **Figure 5.2B**, polystyrene (PS) compressed at 4 metric tons provides one example of strain non-uniformity. This particular sample was compressed more in the Y direction than in the X direction, resulting in an ellipsoid shape. DIC analysis can quantify the non-uniform strain in these types of samples.

We employed the Mooney-Rivlin model to correlate strain profiles in the sheet gathered from DIC to the force applied by the melt press, which will be discussed below. The experimental data points in the Mooney-Rivlin model were the median strains from the DIC plots (converted into λ_R). The error bars are the standard deviation of these medians.

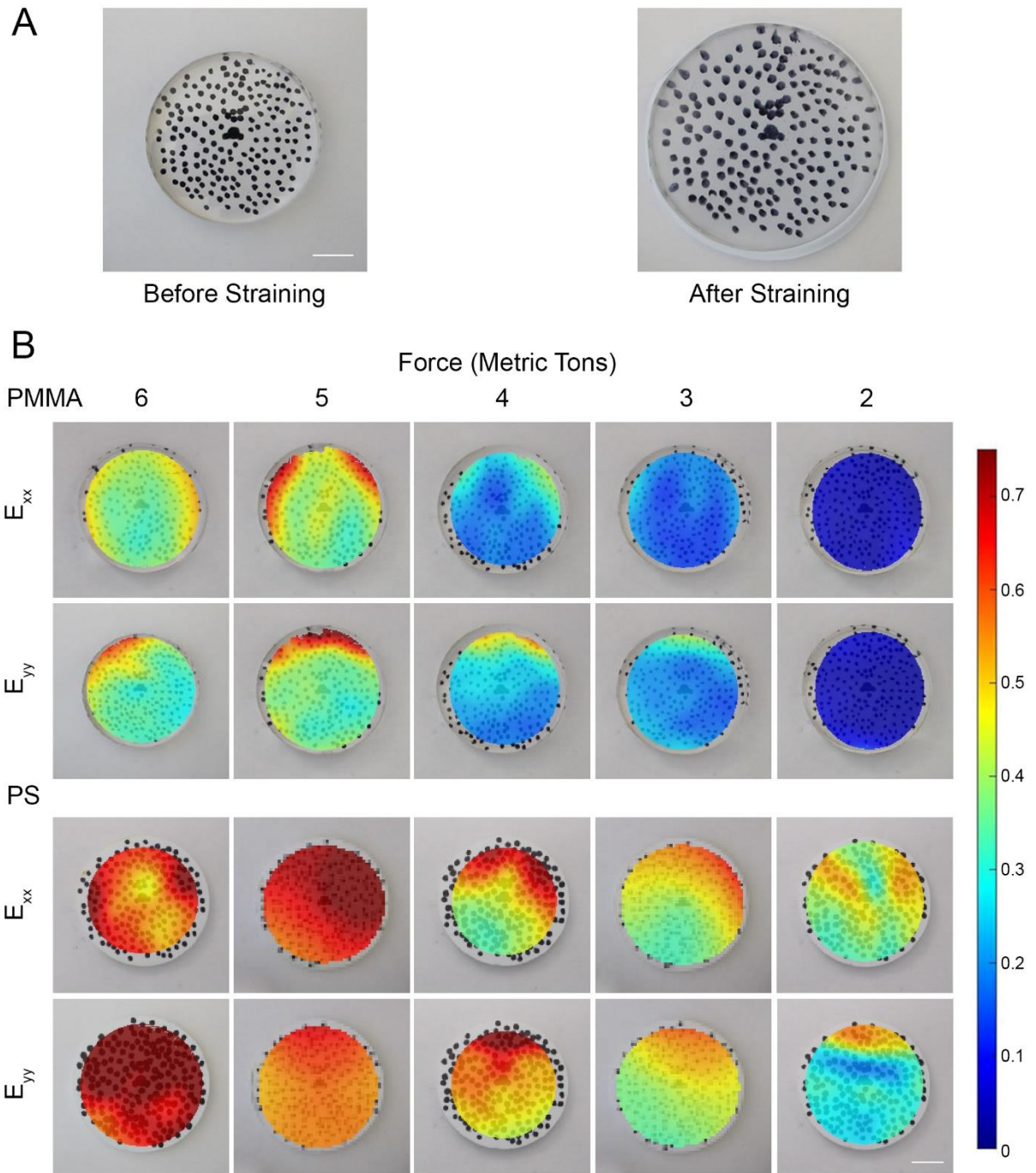


Figure 5.2. Example images depicting pre- and post-strained PMMA sheets (A). DIC derived strain profiles of PMMA and PS samples in the X and Y directions (E_{xx} and E_{yy} , respectively) as a function of applied force in the melt press (B). The colored scale bar represents a breadth of strain (mm/mm) imparted to the sample. The scale bars are 20 mm.

5.3 Experimental Conditions

All starting materials were purchased commercially from McMaster-Carr as planar, unaltered polymer sheets in a range of thicknesses. Polystyrene (PS) sheets were purchased as a range from 1 to 6 mm in thickness while poly(methyl methacrylate) (PMMA) sheets were purchased as a range from 1 to 12 mm in thickness. Note that PS sheets are not available commercially beyond thicknesses of 6 mm. These sheets were then cut into 75 mm diameter disks using a VLS 3.5 laser cutter. This uniform size was used for all samples based on optimization of the polymer stretching and the geometry was chosen to minimize the occurrence of edge effects.

All samples were compressed with a Carver[®] hydraulic melt press. PS and PMMA samples were compressed at temperatures of ~ 90 °C and ~100 °C, respectively. These temperatures are slightly below the T_g range of PMMA (105 °C¹⁷) and PS (103 °C⁵) which allows the polymers to soften and elongate when compressed. The melt press applied forces between 2 – 6 metric tons for 15 – 30 minutes until they stopped stretching. The metal press was maintained at a constant force by controlling the pressure of the hydraulic fluid. Thick samples would stop stretching at ~ 15 minutes while thin samples would take ~ 30 minutes. Upon removal from the melt press, samples were immediately placed between two metal slabs maintained at room temperature that acted as a heat sink and induced rapid cooling. When samples were heated well above their T_g and removed from the melt press, the sheets would recover strain erratically, creating random buckling in the surface of the polymer. Thus, the temperatures of melt pressing were chosen to minimize warping and unwanted sample strain recovery.

DIC image analysis was performed on samples to determine the strain profile of the polymer sheet. The height of all samples was also measured using a caliper for modeling purposes. Upon removal from the melt press, the samples were ready to for self-folding. Below we discuss the folding of thick (thickness >6 mm) and thin (~ 1 mm thick) sheets.

5.3.1 Thick Sheets

For thick samples (~6 – 12 mm in thickness) regardless of polymer chemical composition, asymmetric heating of a thin 'hinge' region actuates self-folding. The strained polymer samples are placed within a laser cutter where the outline of the entire shape (for example the 2D pattern for an unfolded cube) is cut out from the sample. To produce hinges within the material, ~3-4 mm thickness is ablated away from the sample as shown in **Figure 5.1**. This final structure is placed upside down under the heat gun. The heat gun blasts 300°C air at the sample to create a temperature gradient through the sheet thickness (in principle, any source of heat could be used if it can heat the top of the sheet without heating the bottom). When the top of the sheet is heated faster than the bottom and will shrink when it is sufficiently hot. Because the top shrinks faster than the bottom, sheet to bends. The hinge region is thinner than the rest of the sheet, so it folds first. The shapes created with this technique are shown in **Figure 5.3**. It should be noted that the hinge thickness, hinge width, strain within the sample, and uniformity of the applied heat gun will all impact the final folding response. For example, thinner hinge thicknesses result in faster onset times for folding but weaken the structure mechanically. The impact of these experimental factors on self-folding of thick prestrained thermoplastic sheets was discussed in Chapter 3 of this PhD dissertation. For strained, thick samples we typically used a hinge that is 2 mm wide and 2-3 mm thick.

Previously, our group has investigated and reported on the ability to produce curvature within thermoplastic self-folding sheets¹⁸. Many complex and functional self-actuated polymeric systems require both folds and curves within a single structure. By controlling the thicknesses and widths of the hinges, we can produce any combination of folds and curves required to make a complex shape. We speculate that complex shapes such as those reported previously could be generated by taking advantage of this differentiation between bending and folding.

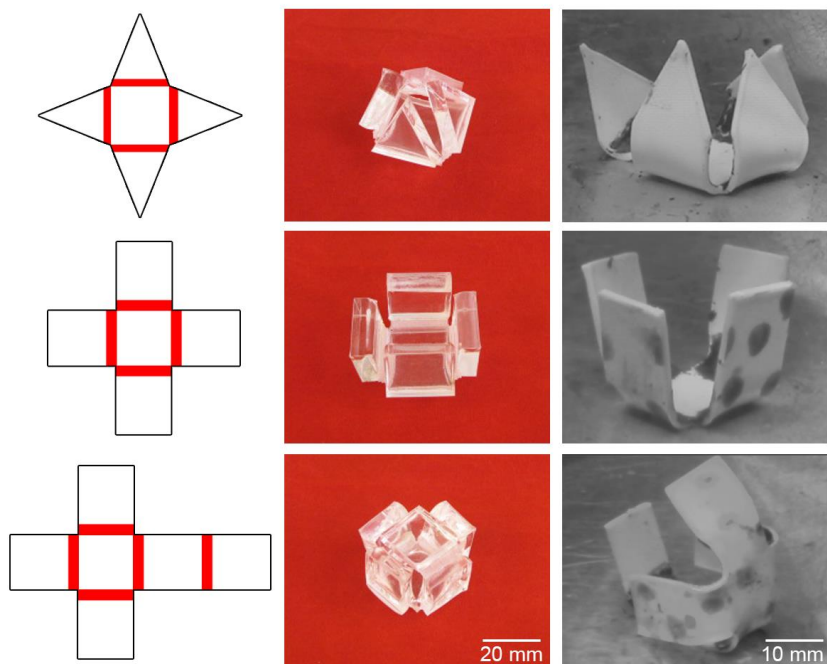


Figure 5.3. Images on the left show the 2D patterns that self-fold into the 3D structures created from thick PMMA (~12 mm, middle) and thin PS (~1 mm, right) sheets. We created a range of complex geometries including pyramids (top), open boxes (middle), and closed boxes (bottom) using both thick and thin self-folding. Note that both the thick and thin folding can be produced with a polymeric material other than the ones demonstrated here (i.e., the thick and thin folding materials can be reversed).

5.3.2 Thin Sheets

For thin samples (~ 1 mm in thickness) self-folding is induced by placing an IR absorbing material on the surface of the sample and exposing it to 250 Watt IR light. Previously, our group has demonstrated the ability to do this by placing black ink from an inkjet printer upon the surface of Shrinky-Dinks® and exposing the sample to IR light^{5,9,18–20}. The 2D sheets are placed on a hot plate at 90 °C and allowed to equilibrate. An IR light is then placed ~ 5 cm from the surface of the sample and turned on. The elevated temperature of the hot plate is used to decrease the temperature differential between the sample and activation temperature

(T_a) of the material (~ 103 °C), which makes folding occur quicker in response to light. T_a is the temperature when folding begins. The Shrinky-Dinks® material is relatively transparent to the IR light, while the black ink is not. The black inked regions absorb IR light, producing a temperature gradient and therefore a strain gradient through the thickness of the sheet. This strain gradient through the materials results in a self-folding motion. Previous work has demonstrated the ability to produce geometrically folded structures, controllable curvature, and the reproducibility of this system has been verified via predictive modeling^{5,9,18–20}.

While the previously developed system is beneficial, the experimental criteria do not fit perfectly with the strained samples produced via melt pressing. Shrinky-Dinks® used in previous research are ~ 0.3 mm thick while our thin, strained samples reach ~ 0.5 mm in thickness. Due to equipment limitations, the samples are too thick to deposit ink using an inkjet printing. Since inkjet printing is not an option, we used black Dixon China Marker. To test the IR light absorption of this material, we performed UV-Visible Spectroscopy on our samples comparing the absorption of black ink as inkjet printed, black ink as extracted and placed on the sample with a cotton applicator, and an even coating of China Marker applied by hand. The spectrum is shown in **Figure 5.4**. Surprisingly, China Marker absorbs light more efficiently than black ink in all cases. China Marker is deposited manually and creates multiple layers on the surface of the polymer sheet. Beer's Law predicts that multilayered substrates absorb more efficiently than single layers, which could explain China Marker's higher absorption. Based on these results, we proceeded with all experimental testing using China Marker to draw hinges on the strained samples for thin sheets.

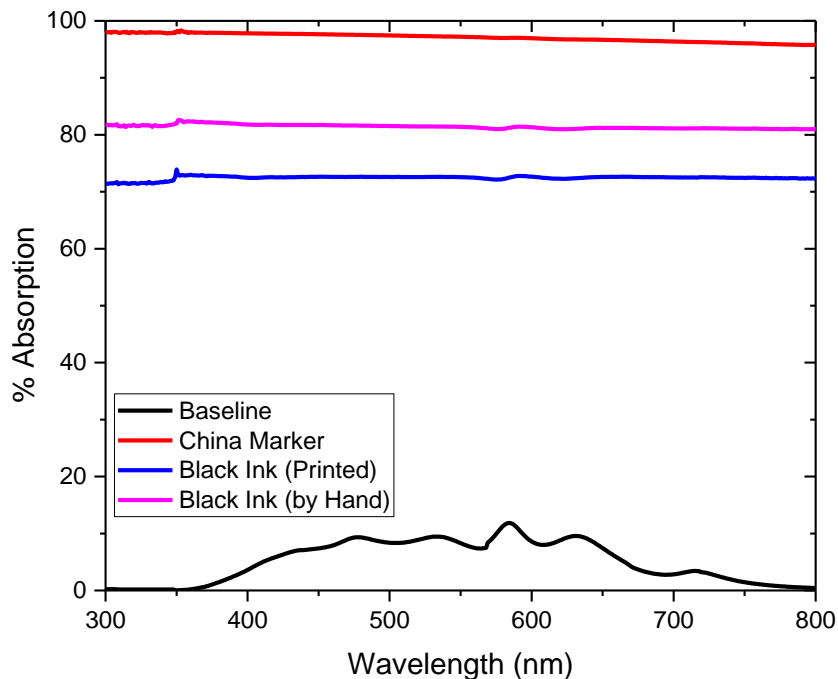


Figure 5.4. UV-Vis shows that China Marker absorbs ~98% of IR light compared with printed black ink and manually applied black ink which absorb ~73% and ~82%, respectively.

All folding structures were cut from the strained samples via laser cutting. Then, China Marker was used to draw hinges upon the surface of the material. Several experimental factors impact the self-folding response of the material including the strain within the sample, including, hinge thickness, hinge width, and uniformity of the IR source. To compare these structures with the previously reported self-folding samples we tested hinge widths of 2, 4, and 6 mm with a range of sample strains and thicknesses based on melt pressing conditions. All starting materials for the thin self-folding work were initially ~1 mm thick and the resulting dihedral angles from experimental tests will be discussed in a later section. The folding angle is the angle between 2 faces separated by a hinge. Dihedral angle is the supplementary angle to the folding angle. In addition, we created complex shapes shown in **Figure 5.3**. It should

be noted that the samples were produced using both PMMA and PS polymer sheets and that thin folding samples actuate much faster than their thick folding counterparts. Heat transfers faster through thinner sheets, so the difference in actuation speed is unsurprising. Unfortunately, this increased speed also makes complex folding difficult. When folding thin samples, sometimes one hinge will fold much faster than the other hinges and starts unfolding before the other hinges finish folding as shown in the pyramid sample in **Figure 5.3**. We speculate that curvature could be self-actuated in melt pressed samples using techniques similar to those previously published¹⁸ - placing a gradient in either the ink layer thickness or the amount of surface area ink coverage along the length of the samples. For this system, we would use China Marker instead of the ink used in the previous study.

5.4 Mooney-Rivlin Model

We drew on existing theories to create a model that predicts the stretching behavior when a sheet is compressed in the melt press. The Mooney-Rivlin model is the standard empirical model used to predict stress-strain behavior in elastomeric polymers²¹. Although more accurate when predicting elastomers, we used the Mooney-Rivlin model to predict the behavior of near T_g PS and PMMA. At these temperature, PS and PMMA behave more like rubber and deform similarly to elastomers²², which are the conventional materials used with the Mooney-Rivlin model²¹.

The Mooney-Rivlin model correlates the extension ratio in the material after melt pressing to the force applied during melt pressing. Equation 5.1 shows the relationship of the stress (σ) to the force applied (F), surface area (A), height extension ratio (λ_z) and material-dependent constants (C_1 , C_2). We fit experimental data to calibrate C_1 and C_2 , which are tabulated on **Table 5.1**. Although the specific sheets used in this study had not been characterized with the Mooney-Rivlin model, other researchers have determined the characteristic constants C_1 and C_2 in the Mooney-Rivlin model for bulk PMMA^{23,24} and PS²⁵.

Table 5.1. Constants for the Mooney-Rivlin Model.

Constants	12 mm thick PMMA (MPa)	6 mm thick PS (MPa)	1 mm thick PS (MPa)
C ₁	0.077	0.023	0.551
C ₂	0.256	0.060	0.878

Equation 5.2 defines the extension ratio of the height as a function of the sheet thickness before (Z_0) and after (Z) straining (i.e., melt pressing) of the sample. We utilize the extension ratio, defined in Eq. (5.2) to stay consistent with Chapters 3 and 4. Equation 5.3 assumes that the deformation of the sheet is affine and it defines the relationship between the extension ratios for height (λ_z) and radius (λ_R) of a disk geometry.

$$\sigma = \frac{F}{A} = 2\left(C_1 + \frac{C_2}{\lambda_z}\right)\left(\lambda_z - \frac{1}{\lambda_z^2}\right) \quad (5.1)$$

$$\lambda_z = \frac{Z}{Z_0} \quad (5.2)$$

$$\lambda_z \lambda_R^2 = 1 \quad (5.3)$$

Using Equations 5.1, 5.2, and 5.3, we modelled the system to show the radial extension ratio as a function of force applied in the melt press, which is shown in **Figure 5.5**. In the model, the force applied and the surface area determine the extension ratio, not the thickness; therefore, the thickness of the sheet should not affect the amount of strain imported to the sheet. In PMMA, the theory matches the experimental result – the thickness does not affect the strain imparted with the melt press. However, the thickness of PS appears to influence the straining imparted by the melt press as shown in **Figure 5.6**. This discrepancy requires future study to fully understand the behavior. For the current study, we fit the Mooney-Rivlin model

to 1 mm thick PS experimental as shown in **Figure 5.5**. Using this fit, we calculated Mooney-Rivlin constants for 1 mm thick PS as shown in **Table 1**. We use the Mooney-Rivlin model to calculate λ_R as a function of force using the constants for 1 mm thick PS and 12 mm thick PMMA. Using λ_R , we calculated the shrinkage (S) used in the geometric model below.

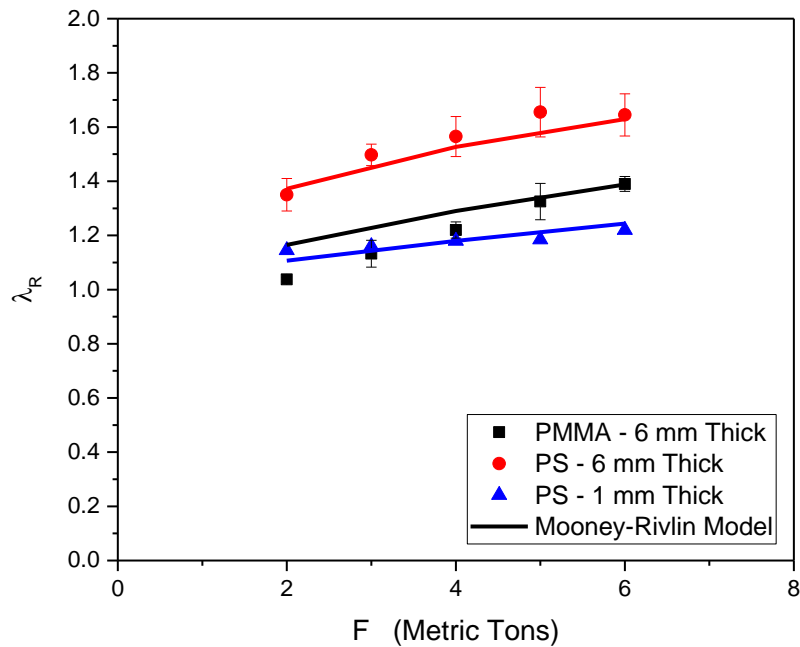


Figure 5.5. The Mooney-Rivlin model correlates the force applied in the melt press to the radial extension ratio (λ_R) post-melt pressing. Using this model, an end user can predict the strain in their sample using only the applied force and the surface area of the disk. The PMMA has a starting thickness of 12 mm. The PS was modeled at two different thicknesses: 6 mm and 1 mm. All samples have a diameter of 75 mm.

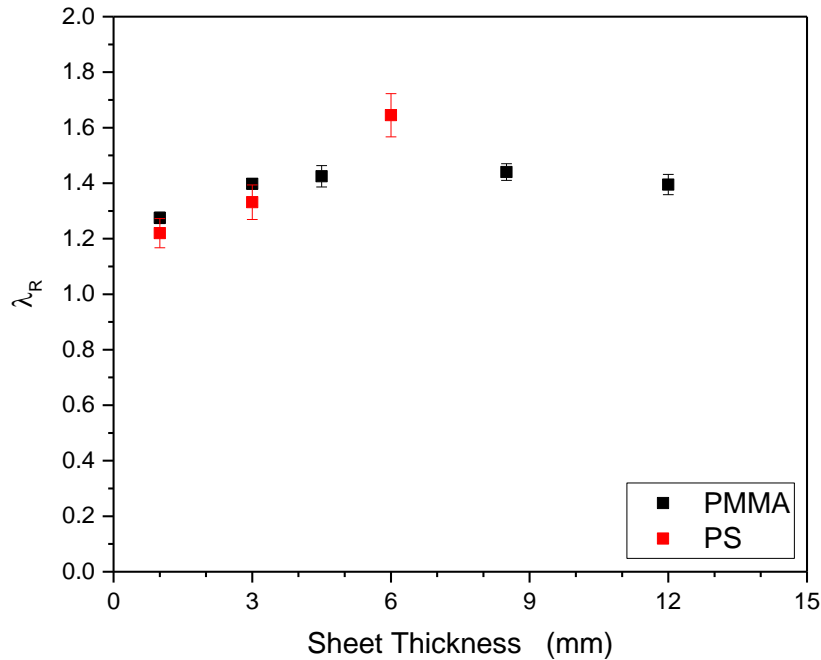


Figure 5.6. λ_R of a sheet strained in the melt press plotted as a function of starting sheet thickness for PMMA and PS. The applied force was 6 metric tons in all cases. λ_R does not depend on thickness for PMMA but does effect PS.

5.5 Geometric Model

A previously derived geometric model⁹, as shown in Equation 5.4, was also employed to predict the dihedral angle of self-folding Shrinky-Dinks®. Here, the dihedral angle (α_D) is a function of sheet thickness (Z), hinge width (W), and shrinkage (S). The shrinkage uses the Swainger strain (as defined in Chapter 3) to define how a sample will transition from a strained state to a recovered/unstrained state. Since we use radial coordinates, we define this equation in terms of the prestrained radius (R), the recovered or unstrained radius (R_0), and the radial extension ratio (λ_R) as shown in Equation 5.5.

$$\sigma_D = 180^\circ - 2 \cdot \tan^{-1}\left(\frac{2Z}{W \cdot S}\right) \quad (5.4)$$

$$S = \frac{R - R_0}{R} = 1 - \frac{1}{\lambda_R} \quad (5.5)$$

This model assumes that: 1) The polymer directly underneath the hinge shrinks; 2) The bottom of the polymer sheet does not shrink considerably; 3) The strain relaxes linearly across the polymer sheet thickness; and 4) The thickness of the film in the folding region does not increase considerably with shrinkage. We predict the dihedral angle for both PMMA and PS in **Figure 5.7** as a function of force and extension ratio. Both films had a starting thickness of ~ 1 mm, used hinges made from China Marker, and were self-folded using IR light.

In **Figure 5.7A-B**, we input a force and predict a dihedral angle using Equations 5.1 and 5.4. The results of this model are highly variable because the force applied during melt pressing does not perfectly produce a uniform strain profile, as evidenced within **Figure 5.2**. It should also be noted that the results of this plot are unique to our experimental setup. A melt press in another lab could be aligned slightly differently, heated at a different rate, have a different amount of friction between the polymer sheet and the plates, and/or apply a different amount of pressure over time which would alter the strain within the post-pressing sample. If a sample is in a low or high strain region, the dihedral angle will change too. When making complex shapes, like those shown on **Figure 5.3**, the variation in sheet strain will cause the sample to fold to different dihedral angles. **Figure 5.7A-B** shows that in general, applying large forces leads to larger dihedral angles. In **Figure 5.7C-D**, we plot the strain in the hinge of the sample and predict the dihedral angle using the geometric model, showing the well-established dependence of dihedral angle on strain^{5-11,20}. Once an end-user has determined the strain profile in their sample, this plot will allow them to predict the dihedral angle by carefully choosing a hinge width. **Figure 5.7E-F** show the predicted dihedral angle compared to the experimental angle for a given sample. If the geometric model were perfectly accurate, the data would have all fallen on a diagonal line with a slope of 1. If a linear trend

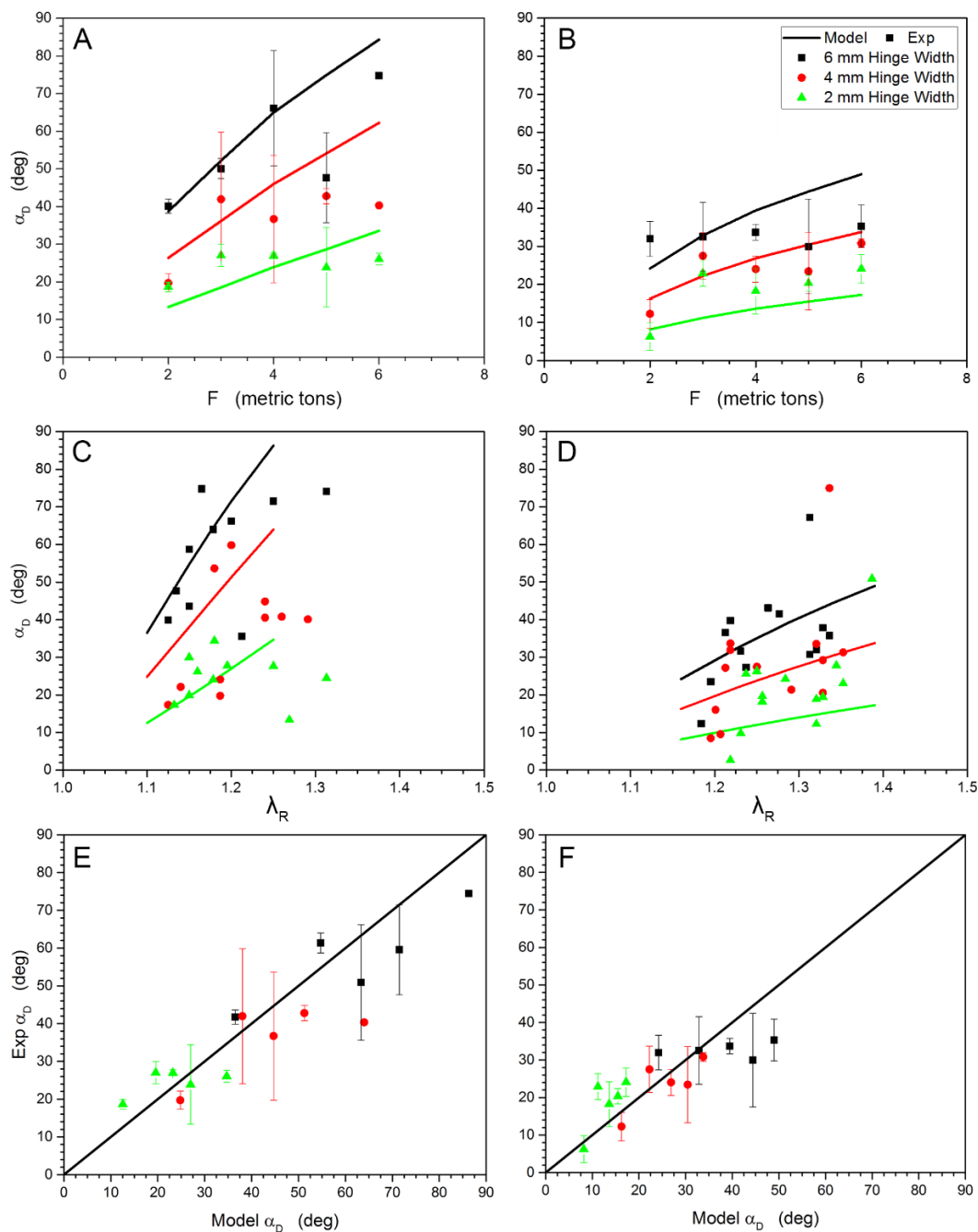


Figure 5.7. A geometric model is used to predict the folding angle as a function of hinge width for PS (left) and PMMA (right). (A-B) We use the geometric model to predict the folding angle based on the applied force in the melt press. This model only accounts for geometry, so any nonuniform strain profiles produced in the melt press will result in deviation. (C-D) Since force does not perfectly correlate to the amount of strain in a particular region of the sheet, the data from A-B is replotted as a function of strain. This plot shows that despite the high variance in the system, the geometric model predicts the dihedral angle relatively well. (E-F) The predicted dihedral angle vs. the experimentally measured dihedral angle demonstrates a reasonable fit with a near-linear trend line.

line is fit to the experimental data in **Figure 5.7E-F**, the slopes of the two linear trend lines are 0.71 (PS) and 0.53 (PMMA). Given the variability in the system, the geometric model fits well.

5.6 Conclusions

Within this work, we have shown that planar thermoplastic sheets of various thicknesses and chemical compositions can be strained by compressing them in a melt press at temperatures close to the glass transition temperature of each sheet. We used Digital Image Correlation to map the strain profile of the samples after melt pressing and to indicate areas of non-uniformity in strain. To demonstrate the applicability of this lab-scale straining technique, we produced a range of 3D complex geometries, including, pyramids, open boxes, and closed boxes by folding the pre-strained thick PMMA and thin PS sheets. These structures demonstrate that complex shapes can be made from thermoplastic sheets prestrained in a melt press, with a wide range of sheet thicknesses. Thin samples (~1 mm) self-folded into cubes and pyramids⁵ while the thick samples (~12 mm) folded into complex 3D shapes at relatively large thicknesses of PMMA for the first time. The Mooney-Rivlin and the geometric models predict accurately the strain and dihedral angle of generated samples, respectively. This system can produce self-folding devices of various complex shapes using both thick and thin sheets. We speculate that this process is also amenable to the production of curvature across the entire sheet instead of localized folding. The ability to tailor a specific application based on the polymer composition, polymer thickness, hinge width, and activation mechanism (including temperature constraints) may provide industrial applications. By harnessing true tunability of lab-scale self-folding polymeric materials that has been previously been unattainable, devices such as grippers, encapsulating boxes, sensors, and actuators are all potential applications with which this work could be utilized.

5.7 Acknowledgements

We thank the National Science Foundation for supporting this work under the NSF EFRI program (Grant No. 1240438). This material is also based in part upon work supported by the National Science Foundation Graduate Research Fellowship under Grant No. DGE-1252376.

References

1. Hayes, G. J., Liu, Y., Genzer, J., Lazzi, G. & Dickey, M. D. Self-Folding Origami Microstrip Antennas. *IEEE Trans. Antennas Propag.* **62**, 5416–5419 (2014).
2. Mailen, R. W., Liu, Y., Dickey, M. D., Zikry, M. & Genzer, J. Modelling of shape memory polymer sheets that self-fold in response to localized heating. *Soft Matter* **11**, 7827–7834 (2015).
3. Allensworth, J. R., Liu, Y., Braun, H., Genzer, J. & Dickey, M. D. In-plane deformation of shape memory polymer sheets programmed using only scissors. *Polymer* **55**, 5948–5952 (2014).
4. Liu, Y. Shape Programming of Polymeric Materials from 2D to 3D. (North Carolina State University, 2013).
5. Liu, Y., Boyles, J. K., Genzer, J. & Dickey, M. D. Self-folding of polymer sheets using local light absorption. *Soft Matter* **8**, 1764–1769 (2012).
6. Liu, Y., Genzer, J. & Dickey, M. D. ‘2D or not 2D’: Shape-programming polymer sheets. *Prog. Polym. Sci.* **52**, 79–106 (2016).
7. Liu, Y., Miskiewicz, M., Escuti, M. J., Genzer, J. & Dickey, M. D. Three-dimensional folding of pre-strained polymer sheets via absorption of laser light. *J. Appl. Phys.* **115**, 204911 (2014).
8. Liu, Y., Shaw, B., Dickey, M. D. & Genzer, J. Sequential folding of polymer sheets. (2017).
9. Liu, Y., Mailen, R., Zhu, Y., Dickey, M. D. & Genzer, J. Simple geometric model to describe self-folding of polymer sheets. *Phys. Rev. E* **89**, 042601 (2014).
10. Davis, D., Mailen, R., Genzer, J. & Dickey, M. D. Self-folding of polymer sheets using microwaves and graphene ink. *RSC Adv.* **5**, 89254–89261 (2015).
11. Davis, D., Chen, B., Dickey, M. D. & Genzer, J. Self-folding of Thick Polymer Sheets Using Gradients of Heat. *J. Mech. Robot.* **8**(3), 031014 (2015).
12. Chen, C.-S. *et al.* Shrinky-Dink microfluidics: 3D polystyrene chips. *Lab. Chip* **8**, 622–624 (2008).
13. Grimes, A. *et al.* Shrinky-Dink microfluidics: rapid generation of deep and rounded patterns. *Lab. Chip* **8**, 170–172 (2008).

14. Taylor, D., Dyer, D., Lew, V. & Khine, M. Shrink film patterning by craft cutter: complete plastic chips with high resolution/high-aspect ratio channel. *Lab. Chip* **10**, 2472–2475 (2010).
15. Lin, S., Lee, E., Pegan, J., Sharma, H. & Khine, M. Smart (shrink manufacturing advanced research tools). in *2015 Transducers - 2015 18th International Conference on Solid-State Sensors, Actuators and Microsystems (TRANSDUCERS)* 580–583 (2015).
16. Lin, S., Lee, E. K., Nguyen, N. & Khine, M. Thermally-induced miniaturization for micro- and nanofabrication: progress and updates. *Lab. Chip* **14**, 3475–3488 (2014).
17. Brandrup, J., Immergut, E. H. & Grulke, E. A. *Polymer Handbook*. (2003).
18. Hubbard, A. M., Mailen, R., Zikry, M., Dickey, M. & Genzer, J. Controllable Curvature from Planar Polymer Sheets in Response to Light. *Soft Matter* (2017).
19. Liu, Y., Shaw, B., Dickey, M. D. & Genzer, J. Sequential self-folding of polymer sheets. *Sci. Adv.* **3**, e1602417 (2017).
20. Mailen, R., Liu, Y., Dickey, M. D., Zikry, M. & Genzer, J. Modeling of shape memory polymer sheets that self-fold in response to localized heating. *Soft Matter* **11**, 7827–7834 (2015).
21. Feng, W. W. & Hallquist, J. On Mooney-Rivlin Constants for Elastomers. in *LS-DYNA 1-10* (2012).
22. Mulliken, A. D. & Boyce, M. C. Mechanics of the rate-dependent elastic–plastic deformation of glassy polymers from low to high strain rates. *Int. J. Solids Struct.* **43**, 1331–1356 (2006).
23. Ogura, K. & Takahashi, M. Uniaxial and Biaxial Extension Behavior of a Lightly Cross-Linked PMMA Melt at Constant Strain Rates. *日本レオロジー学会誌* **31**, 79–83 (2003).
24. Ogura, K. & Takahashi, M. Uniaxial Extension Behavior of Cross-Linked Poly (methyl methacrylate)s with Various Degrees of Cross-Linking. *日本レオロジー学会誌* **31**, 85–89 (2003).
25. Oommen, B. & Van Vliet, K. J. Effects of nanoscale thickness and elastic nonlinearity on measured mechanical properties of polymeric films. *Thin Solid Films* **513**, 235–242 (2006).

CHAPTER 6

Summary and Future Outlook

6.1 Summary

This Ph.D. dissertation describes techniques to convert 2D sheets into 3D objects with a focus on thick thermoplastics, including poly(methyl methacrylate) (PMMA) and polystyrene (PS). The basic premise of this work is to release strain in localized regions of prestrained polymer sheets using heat. We examined various stimuli to deliver the heat including microwaves, infrared (IR) light, uniform heat with an oven, and asymmetric heat supplied by a heat gun. We folded both simple and complex shapes including boxes, cranes, and the Muira Ori fold.

We demonstrated the ability to self-fold pre-strained polymer films using microwaves as a heating source. A pattern of graphene ink on the surface of pre-strained polymer films absorbs the microwaves and causes the polymer to shrink directly below the hinge, which induces the polymer sheet to fold. The dihedral angle is directly proportional to the hinge width printed on the polymer sheet and it is possible to self-fold to 180° . The quality of the folding depends on the geometry and orientation of the sample due to uneven distribution of microwaves energy in the microwave reactor (commercial microwaves also have non-uniform heating). The best folding occurs when the hinge receives as uniform heating as possible across its length, which occurs at an azimuthal sample orientation of 90° within the reactor. A finite element model suggests that the absorption of microwave energy by the hinge results in a temperature difference of $\sim 40^\circ\text{C}$ from top to bottom of the polymer samples. This large temperature difference explains why the samples can fold within seconds despite starting at room temperature.

We successfully programmed and folded three different thermoplastic sheets (PMMA, PS, and PC all 2 mm thick) as well as PMMA sheets with a range of thicknesses (ranging from 1.5 to 12 mm). Previous self-folding of thermoplastics was limited to thin sheets, but thicker sheets can support more stress and are therefore form more robust 3D shapes. The sheet folding occurs by prestraining local regions of the polymer sheets and then heating them asymmetrically by applying heat from a heat gun to one side of the sheet. The dihedral angle

of the sheet heated with a heat gun can be described by a simple geometrical model for a range of thicknesses, extension ratios, and degree of prestrain all for polymeric materials studied. Using the Almansi strain rather than the Swainger strain improved the match between the experimental data and the geometric model. We characterized the folding behavior in terms of the thickness, strain, material type, folding speed, and temperature behavior of the hinge.

We also demonstrated a method to create complex origami folds using only rubber bands, binder clips, ablated sheets of PMMA, and an oven. The sheets can be folded reliably, reversibly, and repeatedly. The rubber band programs the dihedral angle as predicted by the law of cosines. A force balance model predicts the onset of folding in samples with hinges up to 0.8 mm thick. Finally, we created a new programming method that changes the base structure that our samples unfold into when the rubber bands have been removed and heat is applied. We speculate that this technique could be used to make morphing objects from the same starting sheet of material.

Finally, we have shown that planar thermoplastic sheets of various thicknesses and chemical compositions can be strained by compressing them in a melt press at temperatures close to the glass transition temperature of each sheet. We used Digital Image Correlation to map the strain profile of the samples after melt pressing and to indicate areas of non-uniformity in strain. To demonstrate the applicability of this lab-scale straining technique, we produced a range of 3D complex geometries, including, pyramids, open boxes, and closed boxes by folding the pre-strained thick PMMA and thin PS sheets. These structures demonstrate that complex shapes can be made from thermoplastic sheets prestrained in a melt press, with a wide range of sheet thicknesses. Thin samples (~1 mm) self-folded into cubes and pyramids⁵ while the thick samples (~12 mm) folded into complex 3D shapes at relatively large thicknesses of PMMA for the first time. The Mooney-Rivlin and the geometric models predict accurately the strain and dihedral angle of generated samples, respectively. This system can

produce self-folding devices of various complex shapes using both thick and thin sheets. We speculate that this process is also amenable to the production of curvature across the entire sheet instead of localized folding. The ability to tailor a specific application based on the polymer composition, polymer thickness, hinge width, and activation mechanism (including temperature constraints) may provide industrial applications. By harnessing true tunability of lab-scale self-folding polymeric materials that has been previously been unattainable, devices such as grippers, encapsulating boxes, sensors, and actuators are all potential applications with which this work could be utilized.

6.2 Future Outlook

The following highlights future areas of research and applications that are worth exploring in the future.

6.2.1 Chemical Folding

'Chemical folding' was an idea we explored that never worked as well as we hoped. The basic idea was to diffuse a plasticizer through the thickness of a sheet to create a hinge by lowering the T_g in a gradient throughout the hinge. As the concentration of the plasticizer increases, the T_g would drop below room temperature and allow the surface of the sample (where the concentration was highest) to shrink while the backside of the hinge (where the concentration was lowest) to stay extended. In principle, this method would induce self-folding in polymers without using heat. Unfortunately, either the plasticizers did not diffuse fast enough into the material to create a significant gradient in T_g or they dissolved the material completely.

We created a bilayer system composed of PS and scotch tape and submerged in styrene. The styrene penetrated the PS side but not the tape side of the bilayer. This allowed the system to fold but the styrene would dissolve the PS as soon as the sample finished

folding. Removing the bilayer from the styrene also did not work because the styrene weakened the sample and the bilayer would break when moved.

Getting this concept to function as intended requires a specific combination of plasticizer/solvent and polymer. The plasticizer/solvent would need to diffuse through the hinge quickly enough that a gradient in T_g would form but not dissolve the polymer in the process. The polymer would also need to be prestrained and be able to recover that strain in its partially solvated state. If a polymer and plasticizer/solvent system could be found, this system could lead to remote deployment applications.

6.2.2 Melt Press - Future Work

Chapter 5 discusses using a melt press to create strained PS and PMMA for self-folding applications. It would be interesting to expand the scope of this work to include polyethylene terephthalate (PET), poly lactic acid (PLA), polycarbonate (PC) and various polyesters with a T_g above room temperature. We want to show that the melt press straining method is robust and can work for many different polymers.

We also plan to collect more data on all polymers strained with the melt press to expand the predictive powers of both models discussed in Chapter 5. With a clear trend for each polymer, we could create a program online where a user could input the polymer, force, and geometry, and the program would predict the range of strains expected in the polymer sheet.

Finally, we will explore how the limitations of the equipment affect the straining process. We plan to test how the strain profile will change if we cool the sample while in the melt press, if we use a different melt press, or if we use a mold to limit the maximum extension of the polymer sheet.

6.2.3 Children's Toy / Folding Kit

While running outreach events using self-folding polymer sheets¹⁻³, we noticed the high levels of excitement and engagement from the children participating in the demonstration. We setup a hot plate and IR light setup to allow children to draw hinges on prestrained PS and watch their inventions self-fold before their eyes. At the end of the event, the parents would ask our team where they could purchase the materials to recreate the demonstration in their home. We realized that a market exists for a self-folding origami system designed for home use. Unfortunately, the system used for outreach is not safe for children due to the high temperatures involved. Luckily, the system presented in Chapter 4 is safe for home use.

In Chapter 4, we discuss a bilayer system that can fold any number of prescribed and modular shapes in uniform heat using all household safe materials. We are considering commercializing this project to create a children's toy for the market.

The toy we propose is motivated by three main drivers:

1) Creating engaging classrooms: As a visually stimulating application of science, we could market the toy to teachers to make science class rooms more exciting to young future scientists. They could engage the students in an exploration of what drivers the shape change and look at how different facts influence the final shape. Such a lesson could involve teaching children about geometry, origami, materials, plastics, energy, and shape programmable materials. Although primarily aimed at children, it also provides a visual tool for teaching principles of polymers to college students and adults.

2) Inspiring young scientists: One of the biggest drivers for commercialization are the parents met during outreach events. Kids from both primary and secondary school were very excited while making 3D shapes from 2D sheets without using their hands, and parents noticed. We want to provide the opportunity for parents to bring that excitement about science to their home.

3) Capitalizing on a demand in the market: Given the excitement we see at every outreach event, we believe there is a market for self-folding toys. We plan to make a kit that enables children to fold birds, planes, and modular shapes. If this product is successful, we could start a line of products with different themes. We are currently pitching this idea to publishers in the toy industry to find an industrial partner.

To bring this product to market, some refinement and safety testing is still needed. The shapes we put into a kit would need to avoid sharp edges and be strong enough to survive a child playing roughly. We plan to explore different color materials and add-ons like stickers to allow children to customize the toys. We also need to explore the potential safety hazards of using rubber bands in an oven. If a significant amount of material is degrading or becoming air-borne, it could contaminate food cooked using the oven. If we can overcome these safety concerns and find an industrial partner, we look forward to creating this toy.

6.2.4 Optical Applications for the Folding Driven by Elastic Filaments

When exploring the effect of hinge thickness on the folding/curving of the folded samples in the bilayer system from Chapter 4, some samples that did not behave ideally curved out-of-plane. After improving our bending technique, we could make convex lens. We could manipulate this effect to create cost-effective, low throughput PMMA lens.

We have done some preliminary work to create lens using the pyramid design (Chapter 4 **Figure 4.3**). When this structure folds, the base of the pyramid bows out and makes a convex lens. If we cut out the bowed convex base from the sheet, we can create a lens.

For this to work, one would first need to explore which parameters affect the curvature in the hinge. So far, we know that the hinge thickness and dihedral angle both affect the curvature. We would also recommend building a geometric model to predict the curvature/magnification based factors like dihedral angle, hinge geometry, and sheet

thickness. Once we can control and predict the optics, we would need to find the size, shape, and magnification to target an application. Tunable, plastic lens could open new applications for cost-effective optics.

6.3 Final Thoughts

Self-folding systems work best when applied to situations like remote deployment or on the microscopic scale, where manipulating by hand is not an option. As scientists innovate self-folding technique, we create a larger toolbox for applications and expand what technology can use self-folding components. As we look to the future, we use the tool box of techniques developed now to solve the problems of tomorrow.